AD-A266 542

BB

1

DTIC
S ELECTE D
JUL 08 1993
B

DISTRIBUTION STATEMENT A
Approved for public release;
Distribution Unlimited

DEPARTMENT OF THE AIR FORCE
AIR UNIVERSITY

AIR FORCE INSTITUTE OF TECHNOLOGY

Wright-Patterson Air Force Base, Ohio

AFIT/DS/AA/93-1

Hopf Bifurcation in Viscous, Low Speed Flows About an Airfoil with Structural Coupling

DISSERTATION

Mark John Lutton
Captain

AFIT/DS/AA/93-1

Approved for public release; distribution unlimited

93 7 07 012

93-15357

152pg

AFIT/DS/AA/93-1

HOPF BIFURCATION IN VISCOUS, LOW SPEED FLOWS ABOUT AN AIRFOIL WITH STRUCTURAL COUPLING

DISSERTATION

Presented to the Faculty of the School of Engineering
of the Air Force Institute of Technology
Air University
In Partial Fulfillment of the
Requirements for the Degree of
Doctor of Philosophy

DTIC QUALITY INSPECTED 5

Accession For
NTIS GRA&I ☑
DTIC TAB ☐
Unannounced ☐
Justification
By
Distribution/
Availability Codes
Dist | Avail and/or Special
A-1

Mark John Lutton, B.S., M.S.
Captain

March, 1993

Approved for public release; distribution unlimited

AFIT/DS/AA/93-1

HOPF BIFURCATION IN VISCOUS, LOW SPEED FLOWS ABOUT AN AIRFOIL WITH STRUCTURAL COUPLING

Mark John Lutton, B.S., M.S.

Captain

Approved:

1 Apr 93

Mark Oxley 1 Apr 93

Gerald A Hasen 1 Apr 93

Ronald L Bagley 1 APR 93

2 April 93

J S Przemieniecki 3 May 1993

J. S. Przemieniecki

Senior Dean

Acknowledgments

Many people deserve recognition for their contributions to this research effort. I would particularly like to thank my research committee chairman, Dr. Philip Beran. Without his continued guidance and advice, this effort would not have been possible. Thanks are due to the members of my research committee, Col Ronald Bagley, Lt Col Gerald Hasen, Dr. Mark Oxley, and Dr. Joseph Shang. Col Bagley provided insightful criticism and guidance. Without his inputs the research would not have assumed its present form; he suggested the application of Theodorsen's function to provide a basis of comparison for the numerical algorithms. Lt Col Hasen similarly provided insightful guidance and was always available to assist with a problem, technical or otherwise. Dr. Oxley was recruited as a committee member less than two months prior to the defense, replacing Dr. Vadim Komkov, who had retired. His willingness to accept this increased workload and his rapid orientation to the technical issues are greatly appreciated. A special measure of appreciation is due to Dr. Shang, who served in the dual capacity as sponsor of the research, and as the Dean's representative, requiring a painstaking review of the document.

Finally, I owe much more than gratitude to my wife, Venita, and five children, Lena Marie, Matthew Russell, Shawn Eric, Justin Leslie, and Chad Emerson. Venita unhesitatingly sacrificed her needs and desires so that I could accomplish this work. The children similarly were deprived of certain recreations due to my activities. In addition, my family provided me with motivation and a constant source of inspiration. Rather than thanking them, I would prefer now to try and make it up to them over the ensuing years.

Mark John Lutton

Table of Contents

Page

Acknowledgments iii

Table of Contents iv

List of Figures vii

List of Tables xi

List of Symbols xii

Abstract xv

I. Introduction 1
  - 1.1 Overview of Part I 1
    - 1.1.1 The Influence of Turbulence 3
  - 1.2 Overview of Part II 5

II. Analysis: Part I 8
  - 2.1 Equations of Motion 8
  - 2.2 Coordinate Transformation 13
  - 2.3 Aerodynamic Coefficients 15
  - 2.4 Boundary Conditions 17
  - 2.5 Numerical Implementation 19

III. Results and Conclusions: Part I 23
  - 3.1 Grid Refinement and Sensitivity 23
  - 3.2 Variation of Natural Frequencies: Single and Dual Axes . . 25

Page
3.3 Influence of Structural Damping 31
3.4 Impact of the Structural Model on the Solution Space . . . 32
3.5 Conclusions 36

IV. Analysis: Part II 49
4.1 Turbulence Model Implementation 49
4.2 Modification of the Incompressible Code 52
4.3 The Genesis of Theodorsen's Function 56
4.4 Beam and Warming Code 63

V. Results and Conclusions: Part II 68
5.1 Overview 68
5.2 Flutter Onset: Comparison with Theory and Experiment . 69
5.3 Comparison with Inviscid Aerodynamic Transfer Function 72
5.4 Conclusions 92

VI. Summary 94

Appendix A. Code Validation 97
A.1 Integration of the Navier-Stokes Equations 97
A.2 Application of Structural Model 103

Appendix B. Comparison of Incompressible Codes 105
B.1 Validity of LU Decomposition Approach 105
B.2 Stability Analysis by Model Equation 108

Appendix C. Direct Calculation of Hopf Points 114
C.1 Hopf Bifurcation Algorithm: Fixed Airfoil 114
C.2 Hopf Bifurcation Algorithm: Moving Airfoil 117

Page

Appendix D. Computer Codes and Resources 125

D.1 Software Documentation 125

D.2 Algorithm Performance 129

Bibliography 130

Vita 134

List of Figures

Figure Page

1. Regimes of fluid flow across a circular cylinder [10] 4
2. Inertial and A-Frames 9
3. Airfoil with Linear and Torsional Springs Affixed 12
4. Flowchart Detailing Implementation of Aerodynamic and Structural Models 22
5. Grid 1 (59x25) 26
6. Grid 2 (99x40) 27
7. Variation of Strouhal no. with Domain Size 28
8. Critical Reynolds no. vs ω, $\alpha = 0.2$ rad 29
9. Critical Reynolds no. vs ω, $\alpha = 0.1$ rad 30
10. Effect of Structural Damping $Re = 450, \zeta = 0.5$; Fourier Analysis of C_l 38
11. Effect of Structural Damping $Re = 450, \zeta = 2.0$; Fourier Analysis of C_l 39
12. Effect of Structural Damping $Re = 650, \zeta = 2.0$; Fourier Analysis of C_l 40
13. Vorticity in Near Wake, Fixed Airfoil, $Re = 750$ 41
14. Vorticity in Near Wake, Moving Airfoil, $Re = 750$ 41
15. Hopf Bifurcation Structure: $\alpha = 0.2$ rad, Stable Equilibrium Path (solid line), Unstable Equilibrium Path (dashed line), Dual Axes (◇), Fixed Axes (⊙), Vertical Axis (△) 42
16. Fixed Airfoil Case, $Re = 1200$, $\alpha = 0.2$ rad: (a) C_l Phase Plot (b) Time History (c) Fourier Analysis 43
17. Vertical Axis Case, $Re = 1200$, $\alpha = 0.2$ rad; (a) C_l Phase Plot (b) Time History (c) Fourier Analysis 44
18. Fixed Airfoil Case, $Re = 1600$, $\alpha = 0.25$ rad; C_l Phase Plot Near Equilibrium 45
19. Vertical Axis Case, $Re = 1600$, $\alpha = 0.25$ rad; C_l Phase Plot Near Equilibrium 46

Figure Page

20. Dual Axes Case, *Re* = 380, $\alpha_o = 0.2$ rad; (a) C_l Phase Plot (b) Time History (c) Fourier Analysis 47

21. Dual Axes Case, *Re* = 950, $\alpha_o = 0.2$ rad; (a) C_l Phase Plot (b) Time History (c) Fourier Analysis 48

22. Regions of Application for Turbulence Model 51

23. Definition of $\bar{x}, \bar{y}$ Coordinate System 53

24. Conformal Map of Wing Profile with Circulation Element in Wake . 59

25. Real and Imaginary Components of the Theodorsen Function 62

26. Flutter Onset Velocity as a Function of ω_h/ω_α. 71

27. Comparison of Calculated (solid line) and Theoretical (long-dashed line) Lift Coefficient, Compressible Code, α (short-dashed line), Reduced Frequency $k = 0.05$; (a) $Re = 100$, (b) $Re = 1000$, (c) $Re = 1.5 \times 10^5$, (d) $Re = 3.0 \times 10^6$ 79

28. Comparison of Calculated (solid line) and Theoretical (long-dashed line) Lift Coefficient, Compressible Code, α (short-dashed line), Reduced Frequency $k = 0.2$; (a) $Re = 100$, (b) $Re = 1000$, (c) $Re = 1.5 \times 10^5$, (d) $Re = 3.0 \times 10^6$ 80

29. Comparison of Calculated (solid line) and Theoretical (long-dashed line) Lift Coefficient, Compressible Code, α (short-dashed line), Reduced Frequency $k = 1$; (a) $Re = 100$, (b) $Re = 1000$, (c) $Re = 1.5 \times 10^5$, (d) $Re = 3.0 \times 10^6$ 81

30. Comparison of Calculated (solid line) and Theoretical (long-dashed line) Lift Coefficient, Compressible Code, α (short-dashed line), Reduced Frequency $k = 2$; (a) $Re = 100$, (b) $Re = 1000$, (c) $Re = 1.5 \times 10^5$, (d) $Re = 3.0 \times 10^6$ 82

31. Comparison of Calculated (solid line) and Theoretical (long-dashed line) Lift Coefficient, Compressible Code, α (short-dashed line), Reduced Frequency $k = 4$; (a) $Re = 100$, (b) $Re = 1000$, (c) $Re = 1.5 \times 10^5$, (d) $Re = 3.0 \times 10^6$ 83

Figure Page

32. Comparison of Calculated (solid line) and Theoretical (long-dashed line) Lift Coefficient, Compressible Code, α (short-dashed line), Reduced Frequency $k = 6$; (a) $Re = 100$, (b) $Re = 1000$, (c) $Re = 1.5 \times 10^5$, (d) $Re = 3.0 \times 10^6$ 84

33. Comparison of Calculated (solid line) and Theoretical (long-dashed line) Lift Coefficient, Incompressible Code, α (short-dashed line), Reduced Frequency $k = 0.05$; (a) $Re = 100$, (b) $Re = 500$, (c) $Re = 1000$, (d) $Re = 2000$ 85

34. Comparison of Calculated (solid line) and Theoretical (long-dashed line) Lift Coefficient, Incompressible Code, α (short-dashed line), Reduced Frequency $k = 0.2$; (a) $Re = 100$, (b) $Re = 500$, (c) $Re = 1000$, (d) $Re = 2000$ 86

35. Comparison of Calculated (solid line) and Theoretical (long-dashed line) Lift Coefficient, Incompressible Code, α (short-dashed line), Reduced Frequency $k = 2$; (a) $Re = 100$, (b) $Re = 500$, (c) $Re = 1000$, (d) $Re = 2000$ 87

36. Comparison of Calculated (solid line) and Theoretical (long-dashed line) Lift Coefficient, Incompressible Code, α (short-dashed line), Reduced Frequency $k = 4$; (a) $Re = 100$, (b) $Re = 500$, (c) $Re = 1000$, (d) $Re = 2000$ 88

37. O-Grid 209x108: $k = 1$, $Re = 3 \times 10^6$, (a) Turbulence Model Off, (b) Turbulence Model On 89

38. Phase and Amplitude Errors as a Function of Reduced Frequncy: Compressible Code; Phase Error (⊙) Amplitude Error (△) 89

39. Error Norm as a Function of Reynolds Number: Incompressible Code ($k = 0.2$) 90

40. Vorticity Contours: Incompresible Code, Grid 2, $Re = 500$, $k = 2$, $\tau = 1.0$ 90

41. Vorticity Contours: Incompressible Code, Grid 2, $Re = 500$, $k = 2$, $\tau = 2.0$ 91

42. Vorticity Contours: Incompressible Code, Grid 2, $Re = 500$, $k = 2$, $\tau = 3.0$ 91

Figure Page

43. Vorticity Contours: Compressible Code, O-grid 120x50, $Re = 500$, $k = 2$, $\tau = 3.0$ 92

44. O-grid Structure: (a) Node Distribution; (b) Schematic of Boundaries 98

45. Strouhal Number as a Function of Reynolds no. Experimental: Roshko [28], Tritton [29] and Berger [30]; Computational: Sa and Chang [51], and Present (Grids O2 and O3). 100

46. Drag Coefficient as a Function of Reynolds Number. Experimental: Tritton [29]; Computational: Sa and Chang [51], Borthwick [52], and Present (Grids O1, O2 and O3). 102

47. Comparison of Exact (solid line) and Runge-Kutta (⊙) Solutions: Vertical Axis 103

48. Modulus of Amplification Factor in Complex Plane, (a) Case 1 (A_1), (b) Case 2 (A_2) 113

List of Tables

Table Page

1. Grid Characteristics 23
2. Strouhal no. at $Re = 1200$ and Hopf points, $\alpha = 0.2$ rad 24
3. Tabulated Parametric Results; Reduced Frequency, $k = 1$ 78
4. Characterstics of Grids O1, O2 and O3 99
5. Comparison of Computer Code Performance 129

List of Symbols

Symbol

a - Distance from midchord to axis of rotation (positive right)

b - Airfoil half-chord

C_c - Airfoil section chordwise force coefficient

C_d - Airfoil section drag coefficient

C_k - Airfoil section lift coefficient (theoretical)

$C(k)$ - Theodorsen function

C_l - Airfoil section lift coefficient

C_m - Airfoil section pitching moment coefficient

C_n - Airfoil section normal force coefficient

c - Airfoil chord

D_α - Structural dissipation (damping) term (pitch axis)

D_h - Structural dissipation (damping) term (vertical axis)

$\hat{e}_1$ - Unit vector in noninertial frame (a-frame)

$\hat{e}_2$ - Unit vector in noninertial frame (a-frame)

$\vec{f}$ - Apparent body forces applied in noninertial system

f_e - Explicit fourth-order numerical damping term

f_i - Implicit fourth-order numerical damping term

f_s - Vortex shedding frequency (cycles per aerodynamic time unit)

$\hat{G}$ - Functional form of discretized equations

I_α - Moment of inertia (pitch axis)

$\hat{i}$ - Unit vector in inertial reference frame

$\tilde{J}$ - Transformation Jacobian

$\hat{j}$ - Unit vector in inertial reference frame

K_α - Torsional spring coefficient (pitch axis)

K_h - Linear spring coefficient (vertical axis)

k - Reduced frequency ($\Omega c/2U$)

L_1 - Discrete form of Laplacian operator (interior nodes)

L_2 - Discrete form of Laplacian operator (surface nodes)

L_3 - Discrete operator (vorticity condition)

m_o - Airfoil mass per unit span

p - Pressure

Q_α - Applied aerodynamic moment (pitch axis)

Q_h - Applied aerodynamic force (vertical axis)

Re - Reynolds number $= Uc/\nu$

Re_{crit} - Reynolds number at which flow becomes unsteady

S_t - Strouhal number $= fc/U = f_s$

S_α - Mass static moment

U - Freestream velocity

U_{crit} - Freestream velocity at which flow becomes unsteady

u - Velocity component in noninertial system

v - Velocity component in noninertial system

$\hat{u}$ - Convective velocity (vorticity-transport equation)

$\hat{v}$ - Convective velocity (vorticity-transport equation)

x - Coordinate in noninertial system

y - Coordinate in noninertial system

$\bar{x}$ - Coordinate referenced to axis of rotation

$\bar{y}$ - Coordinate referenced to axis of rotation

α - Geometric angle of attack

α_o - Angle of attack (structural equilibrium)

Δ - Difference operator

ζ - Structural damping factor

ν - Kinematic viscosity

ξ - Transformed coordinate (tangent to airfoil surface)

η - Transformed coordinate (normal to airfoil surface)

θ - Pitch angle (positive counter-clockwise)

τ - Time in aerodynamic units (scaled time)

ϕ_i - Viscous coefficients for Laplacian

φ - Perturbation velocity potential

Γ - Circulation

Ψ - Streamfunction

ψ - Disturbance streamfunction

Ω - Angular velocity of noninertial frame

ω - Vorticity

ω_α - Natural frequency (pitch axis)

ω_h - Natural frequency (vertical axis)

AFIT/DS/AA/93-1

Abstract

The locations of Hopf bifurcation points associated with the viscous, incompressible flow about a NACA 0012 airfoil with structural coupling are computed for very low Reynolds numbers (< 2000). A semi-implicit, first-order-accurate time-integration algorithm is employed to solve the streamfunction-vorticity form of the Navier-Stokes equations. The formulation models the inclusion of simple structural elements affixed to the airfoil and captures the resulting airfoil motion. The equations describing the airfoil motion are integrated in time using a fourth-order Runge-Kutta algorithm.

The dissertation is divided into two parts. In Part I, numerical experiments are performed in the laminar regime to determine if the structural model of the airfoil has an effect upon the location of the Hopf bifurcation point when compared with the fixed airfoil. Results are reported for a variety of structural characteristics, including variation of torsional and linear spring constants, inertial properties, structural coupling, and structural damping. The structure of the solution space is explored by means of phase plots.

In Part II, the Baldwin-Lomax turbulence model is implemented to model turbulent flow. A numerical effort is made to predict the onset of unsteady flow and the results are compared to theory and experiment. A comparison is undertaken with the compressible and incompressible form of the Navier-Stokes equations to assess the correspondence of the unsteady lift evolved by pitching the airfoil at a prescribed frequency and amplitude. Comparisons are made with the lift predicted by the potential flow method of Theodorsen.

HOPF BIFURCATION IN VISCOUS, LOW SPEED FLOWS ABOUT AN AIRFOIL WITH STRUCTURAL COUPLING

I. Introduction

1.1 Overview of Part I

In the past few years, interest in low Reynolds number, time-periodic flows has been increasing. Pulliam [1, 2] has performed numerical studies detailing such flows, demonstrating such phenomena as period-doubling bifurcations and chaotic attractors. Pulliam investigated periodic flows using time integration of the Navier-Stokes equations, and found a sequence of period-doubling bifurcations leading to chaos. Jackson [3] has investigated the onset of vortex shedding corresponding to time-periodic body forces for a variety of body shapes. Strganac and Mook [4] have numerically investigated subsonic flutter for a finite wing using a potential flow model, demonstrating the existence of a "flutter boundary," above which limit-cycle oscillations persist. A substantial portion of Part I was reported earlier [5] as part of an ongoing research effort.

The development of a time-periodic flow, emanating from an equilibrium flow, is an example of Hopf bifurcation [6, 7]. Physically, Hopf bifurcation represents an exchange of stability manifested, in the fluid dynamics context, as the formation of a time-periodic vortex street. The physically relevant processes occuring are the convection and dissipation of vorticity. If the dissipative mechanism dominates, vorticity will be dissipated before a wake instability can be excited, and thus a steady flow results. Conversely, if the convective forces dominate, unsteady vortex shedding ensues. The Reynolds number, representing the ratio of convective to dissipative forces, is therefore physically relevant and serves as the bifurcation parameter. The properties of the solution space, as the bifurcation parameter changes, serve to classify the bifurcation. In this study, a *subcritical* bifurcation is demonstrated numerically. A subcritical bifurcation occurs when, across a given range of the bifurcation parameter, three solution branches to the equation set coexist: a stable equilibrium branch, a stable limit-cycle branch, and an unstable limit-cycle branch connecting the stable branches [6]. This region is referred to in the literature as *bistable*. Physically, a system exhibiting a subcritical bifurcation will be susceptible to perturbations. Seydel [6] offers a more complete description of this type of bifurcation.

Beran [8] has employed time integration as a means of determining and verifying the location of Hopf points for a fixed airfoil in a two-dimensional parametric space defined by Reynolds number and angle of attack. This was accomplished in conjunction with a direct method for computing the Hopf point [3, 9]. The current effort represents a modification to the time-integration algorithm of Beran to allow the numerical prediction of the Hopf bifurcation point for an airfoil with a linear and torsional spring affixed. This represents a simple structural model and thus suggests a means to examine "low Reynolds number" flutter. The central question to be investigated is the coupling effect between the developing aerodynamic flowfield and the structural model of the airfoil, which is now free to vibrate or oscillate in response to the aerodynamic forces. The basic assumptions associated with the fluid are those of an incompressible, viscous, two-dimensional flow. The fluid equations are presented in streamfunction-vorticity form.

The structural model of the airfoil allows motion with two degrees of freedom: pitch and vertical displacement. The equations of motion for the airfoil incorporate linear and torsional spring constants, structural damping in both axes, and structural coupling effects. Numerical experiments are undertaken to determine the effect on the critical Reynolds number, Re_{crit}, when the inertial and structural properties of the airfoil are varied. A limited grid refinement study is undertaken to evaluate the accuracy of the computed Strouhal number and Re_{crit}. The variation of Strouhal number with the computational domain size is also explored. In addition, the structure of the Hopf bifurcation is investigated, with emphasis on the impact of the airfoil structural model. These investigations are undertaken in the laminar flow regime in order to explore the solution structure in the absence of turbulence and unnecessary amounts of artificial dissipation. Low-speed flutter and the associated solution structure in the laminar regime have not been investigated for viscous flows.

1.1.1 ***The Influence of Turbulence*** The transition from laminar to turbulent flow has a fundamental and significant effect upon the onset of unsteady motion in a fluid. The physical progression of this transition is shown in Figure 1 for the case of a circular cylinder [10]. At very low Reynolds numbers ($Re < 5$), the flow is steady and no vortices are present. As the Reynolds number increases, the flow remains steady, but a pair of standing vortices appear in the near wake. A further increase in Reynolds number induces unsteady laminar flow, manifested by asymmetric vortex shedding. It was this laminar regime that was explored for the moving airfoil in Part I to assess the impact of structural model on the flow structure.

The transition to turbulence at larger Reynolds numbers is the hallmark of the next regime. As the Reynolds number increases to approximately 3×10^5, the increased dissipation provided by turbulence disrupts the unsteady vortex street and a quasi-steady flow ensues. As the Reynolds number increases beyond 3.5×10^6, the flow again becomes unsteady with the reestablishment of the vortex street. The transition to turbulent flow represents a natural demarcation between Parts I and II of this work as applied to the prediction of flutter onset. The numerical investigations in Part I are applied in the flow regimes indicated by the first three entries in Figure 1. The numerical investigation of flutter onset in Part II incorporates a turbulence model, and is applied in the flow regimes indicated by the final two entries in Figure 1.

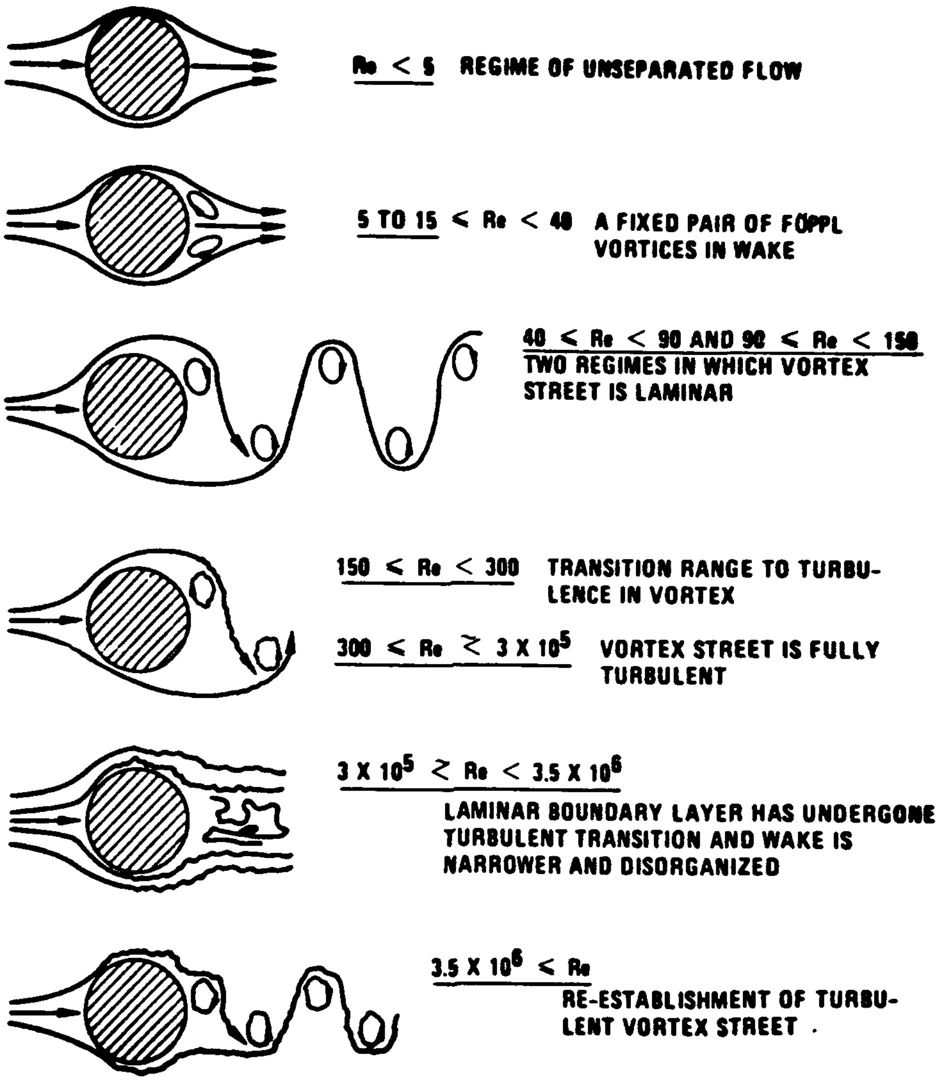
Re < 5 REGIME OF UNSEPARATED FLOW
5 TO 15 ≤ Re < 40 A FIXED PAIR OF FÖPPL VORTICES IN WAKE
40 ≤ Re < 90 AND 90 ≤ Re < 150 TWO REGIMES IN WHICH VORTEX STREET IS LAMINAR
150 ≤ Re < 300 TRANSITION RANGE TO TURBULENCE IN VORTEX
300 ≤ Re ≲ 3 X 10^5 VORTEX STREET IS FULLY TURBULENT
3 X 10^5 ≲ Re < 3.5 X 10^6
LAMINAR BOUNDARY LAYER HAS UNDERGONE TURBULENT TRANSITION AND WAKE IS NARROWER AND DISORGANIZED
3.5 X 10^6 ≤ Re
RE-ESTABLISHMENT OF TURBULENT VORTEX STREET .

Figure 1. Regimes of fluid flow across a circular cylinder [10]

1.2 Overview of Part II

While the exploration of the solution space presented in Part I is of value from an analytic point of view, the results do not directly correspond with experiment (typically performed in the subsonic to transonic regimes [11, 12], with $Re > 5 \times 10^5$, where turbulence is a factor). The predicted onset of unsteady motion (laminar regime) occurs at a Reynolds number much lower than the experimental evidence (turbulent regime) indicates. Therefore, an attempt is made to capture experimental data by implementing a turbulence model to account for these effects at larger Reynolds numbers. The turbulence model selected for this effort is that of Baldwin and Lomax [13] as modified by Knight and Visbal [14]. A brief discussion of the implementation of the turbulence model and its applicability to the present calculations is provided in Chapter 4. An attempt is made to capture numerically the experimental data of Yang and Zhao [11] and the theoretical and experimental results of Theodorsen [15].

A similar computational effort, on a larger scale, was accomplished by Guruswamy [16]. He employed the compressible Navier-Stokes equations with the Baldwin-Lomax turbulence model in conjunction with an aeroelastic model of a wing-body configuration and successfully simulated aeroelastic oscillations for a transonic flow regime ($M_\infty = 0.975$). Although Guruswamy achieved satisfactory results using the Baldwin-Lomax turbulence model, and demonstrated no specific shortcomings, he did question the accuracy of the turbulence model in predicting the onset of flow unsteadiness due to the quasi-steady assumptions applied in its derivation. Kousen and Bendiksen [17] and Wu et al. [18] have also applied the Navier-Stokes equations to the numerical prediction of flutter onset in the high subsonic and transonic regimes. Similar efforts applying the Euler equations have been reported by Bendiksen and Kousen [19] and Robinson et al. [20]. Strganac et al. [21] investigated the numerical simulation of subsonic flutter using a vortex-lattice method. Considerable attention has been devoted to the understanding and prediction of the onset of aerodynamic flutter [12, 15, 22, 23, 24, 25, 26]. In addition to the computational efforts cited, wind tunnel [22, 23] and flight testing [12, 24] in conjunction with theoretical analysis [15, 25] have been the usual mode of inquiry. The advantages of a computational approach include reduced cost, easier application (once a validated code is available), and an ability to explore experimental configurations or parametric studies.

The contribution attempted in Part II is twofold. Firstly, numerical evidence is presented that the bifurcation to an unsteady state is subcritical in the turbulent regime. Secondly, a basis is sought establishing the validity of the numerical prediction of flutter onset. In order to substantiate the basis for numerically predicting flutter onset, a correlation is made between the present numerical results and those predicted by the aerodynamic transfer function of Theodorsen [15]. A NACA 0012 airfoil is oscillated with a prescribed frequency and amplitude; the computed lift coefficient is compared with that predicted by Theodorsen's function. This is accomplished using a modified version of the incompressible code employed in Part I, and a Beam and Warming code authored by Visbal [27]. This is the focus of the second part of the present research effort. The results are presented in Chapter 5.

The modifications to the incompressible code are presented in Chapter 4. A time-dependent metric transformation is applied to account for the airfoil motion rather than the approach outlined in Part I. The reasons for the modifications and the resultant changes to the boundary conditions are discussed. Also provided in Chapter 4 is an outline of the development of Theodorsen's function and the of application of the Beam and Warming algorithm.

Validation of the incompressible code employed in this work is presented in Appendix A. The implementation of the integration procedure for solving the Navier-Stokes equations was validated by simulation of the flow about a fixed circular cylinder. The circular cylinder was chosen because a wide range of experimental data is available [28, 29, 30]. In contrast, there is a paucity of experimental and numerical data available for airfoils over the very low Reynolds number range considered. Therefore, comparisons with experimental and other numerical data are accomplished for the Strouhal number and drag coefficient for the case of the circular cylinder. Good agreement was achieved with the results of previous investigations.

The airfoil equations of motion are identical in form (second-order ordinary differential equations) and thus only the vertical axis was examined for validation purposes. The validation was accomplished by comparing an exact solution to the ordinary differential equation representing the vertical axis to the numerical solution when a prescribed forcing function is applied. A phase lag equal to the largest timestep used in the airfoil computations was applied between the forcing functions to examine the effect on the respective responses. The method of coupling the aerodynamics and the structural model was demonstrated to be accurate.

II. Analysis: Part I

2.1 Equations of Motion

The equations of motion and the method of solution are presented in this section. The modifications to the streamfunction-vorticity formulation of the equations are described for the case of the rotating and translating airfoil. Finally, the implementation of the numerical algorithm is discussed, including the application of the boundary conditions.

Equations are presented throughout in nondimensional form. The velocity scale is the freestream velocity, U, the length scale is the chord length, c, time is nondimensionalized by the aerodynamic scale, c/U. Force per unit mass (acceleration) is nondimensionalized by U^2/c.

In modifying the equations of motion for a two-dimensional, incompressible flow, the approach of Batchelor [31] is applied, wherein the moving frame, i.e., the frame fixed to the airfoil, hereafter referred to as the a-frame, is treated as the computational reference frame. The acceleration of the a-frame relative to a true inertial frame is rectified by inclusion of apparent body forces. These body forces (per unit mass, nondimensionalized) are then added directly to the momentum equation in vector form. The components of momentum must then be examined individually to insure they are correctly handled when transforming to the streamfunction-vorticity form of the equations. An alternate approach to modeling the moving airfoil, involving a time-dependent metric transformation, is presented in Part II.

The acceleration in the inertial system is given by Greenwood [32]:

$$\begin{aligned} \vec{a} &= \frac{d^2\vec{R}}{dt^2} + \frac{d^2\vec{r}}{dt^2} + 2\vec{\Omega} \times \frac{d\vec{r}}{dt} + \frac{d\vec{\Omega}}{dt} \times \vec{r} + \vec{\Omega} \times (\vec{\Omega} \times \vec{r}), \\ &= \frac{d^2\vec{R}}{dt^2} + \frac{D\vec{u}}{Dt} + 2\vec{\Omega} \times \vec{u} + \frac{d\vec{\Omega}}{dt} \times \vec{r} + \vec{\Omega} \times (\vec{\Omega} \times \vec{r}). \end{aligned} \qquad (1)$$

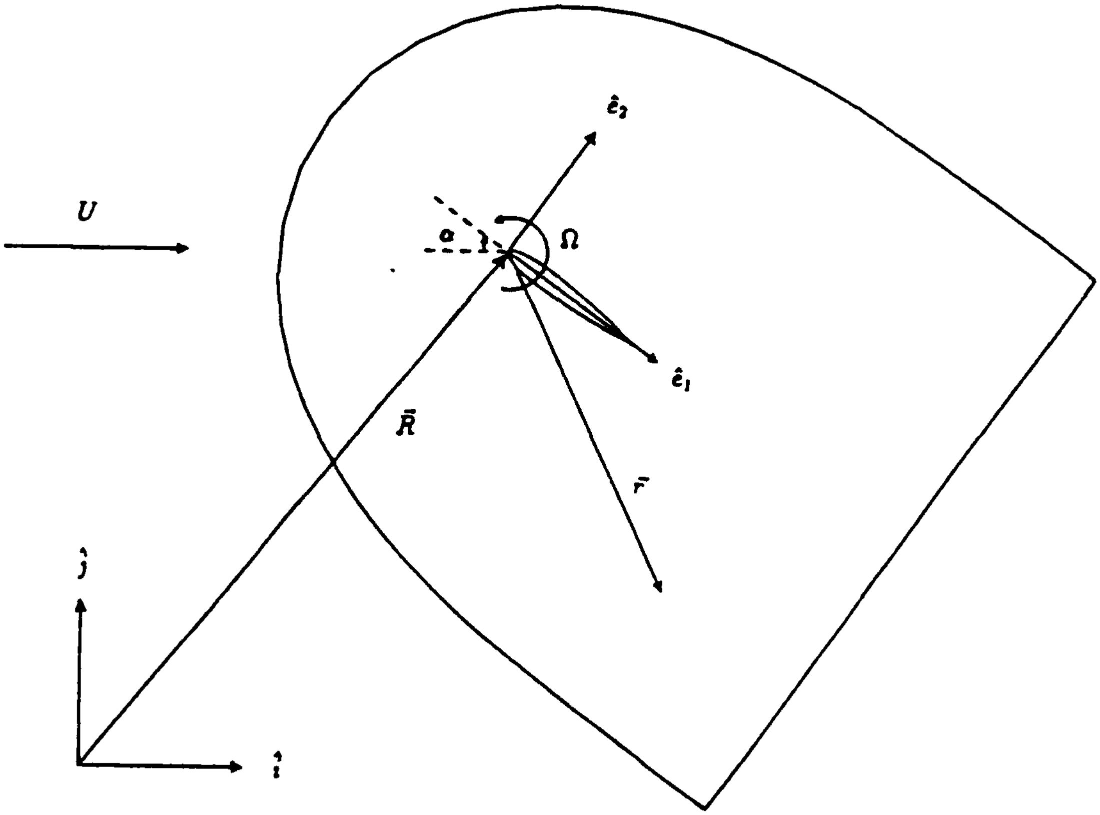
U
α
Ω
$\hat{e}_2$
$\hat{e}_1$
$\bar{R}$
$\bar{r}$
$\hat{j}$
$\hat{i}$

Figure 2. Inertial and A-Frames

where $\vec{R}(t)$ is the position vector to the origin of the a-frame, $\vec{r}$ represents the position vector of a fluid element in the a-frame, and $\vec{\Omega}(t)$ is the angular velocity of the a-frame with respect to the fixed frame (see Figure 2). Here the term $2\vec{\Omega} \times \vec{u}$ accounts for the Coriolis effect, $d\vec{\Omega}/dt \times \vec{r}$ is associated with tangential (Eulerian) acceleration, and $\vec{\Omega} \times (\vec{\Omega} \times \vec{r})$ is the centripetal acceleration, while $\vec{u} = u\hat{e}_1 + v\hat{e}_2$ represents the velocity in the a-frame. The velocity observed in the inertial system is related to this velocity by the relation [32]

$$\vec{V} = \left[\frac{d\vec{R}}{dt}\right]_a + \vec{u} + \vec{\Omega} \times \vec{r}, \tag{2}$$

or, in components referenced to the a-frame system,

$$\begin{aligned} \vec{V} &= (\dot{R}_1 + u - y\Omega)\hat{e}_1 + (\dot{R}_2 + v + x\Omega)\hat{e}_2 \\ &= \tilde{u}\hat{e}_1 + \tilde{v}\hat{e}_2. \end{aligned} \tag{3}$$

The velocity field observed in the inertial frame expressed in components referenced to that frame is given by

$$\vec{V} = (\tilde{u}\cos\alpha + \tilde{v}\sin\alpha)\hat{i} + (-\tilde{u}\sin\alpha + \tilde{v}\cos\alpha)\hat{j}, \tag{4}$$

where $\alpha = \alpha(t)$ and $\dot{\alpha} = -\Omega$.

The acceleration in the a-frame may be equated to the local force per unit mass acting on a fluid element to give the momentum equation. In terms of $\vec{u}(\vec{r}, t)$, assuming an Eulerian formulation [31],

$$\frac{D\vec{u}}{Dt} \equiv \frac{\partial \vec{u}}{\partial t} + \vec{u} \cdot \nabla \vec{u} = \frac{d^2\vec{r}}{dt^2}. \tag{5}$$

The applied forces can be separated into the pressure forces, the viscous forces, and the apparent body forces. If the body forces are denoted by $\vec{f} = f_1\hat{e}_1 + f_2\hat{e}_2$, then the components of the momentum equation [31] may be written

$$\frac{\partial u}{\partial t}+u\frac{\partial u}{\partial x}+v\frac{\partial u}{\partial y} = -\frac{\partial p}{\partial x}+\frac{1}{Re}\left(\frac{\partial^2 u}{\partial x^2}+\frac{\partial^2 u}{\partial y^2}\right)-f_1, \tag{6}$$

$$\frac{\partial v}{\partial t}+u\frac{\partial v}{\partial x}+v\frac{\partial v}{\partial y} = -\frac{\partial p}{\partial y}+\frac{1}{Re}\left(\frac{\partial^2 v}{\partial x^2}+\frac{\partial^2 v}{\partial y^2}\right)-f_2. \tag{7}$$

where $Re = Uc/\nu$. Differentiating the first expression with respect to y and the second with respect to x and subtracting eliminates the pressure term. Using the definition of vorticity, $\omega = v_x - u_y$, we have,

$$\frac{\partial \omega}{\partial t}+u\frac{\partial \omega}{\partial x}+v\frac{\partial \omega}{\partial y} = \frac{1}{Re}\left(\frac{\partial^2 \omega}{\partial x^2}+\frac{\partial^2 \omega}{\partial y^2}\right)+\frac{\partial f_1}{\partial y}-\frac{\partial f_2}{\partial x}. \tag{8}$$

This represents the modified form of the vorticity-transport equation; the definition of streamfunction and the continuity equation remain unaltered. The expressions for f_1 and f_2 are obtained by examining the component form of Eq. (1):

$$f_1 = \ddot{R}_1 - 2v\Omega - y\dot{\Omega} - x\Omega^2, \tag{9}$$

$$f_2 = \ddot{R}_2 + 2u\Omega + x\dot{\Omega} - y\Omega^2, \tag{10}$$

where $\vec{R} = R_1\hat{e}_1 + R_2\hat{e}_2$, and $\vec{r} = x\hat{e}_1 + y\hat{e}_2$.

The streamfunction, Ψ, is defined by the relations

$$\Psi_y = u = \vec{u}\cdot\hat{e}_1, \tag{11}$$

$$-\Psi_x = v = \vec{u}\cdot\hat{e}_2. \tag{12}$$

A disturbance streamfunction is also defined [9] such that

$$\psi(x,y) \equiv \Psi(x,y) - \hat{y}, \tag{13}$$

$$\hat{y} = y\cos\alpha - x\sin\alpha, \tag{14}$$

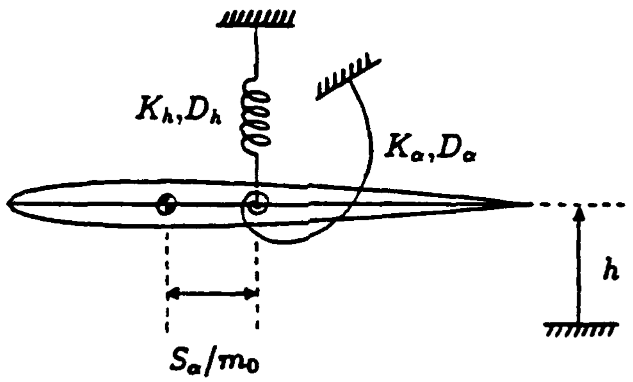

Figure 3. Airfoil with Linear and Torsional Springs Affixed

establishing

$$u = \cos\alpha + \psi_y, \tag{15}$$

$$v = \sin\alpha - \psi_x. \tag{16}$$

Ancillary to the vorticity-transport equation is the Poisson equation for ψ [8]

$$\nabla^2\psi \equiv \psi_{xx} + \psi_{yy} = -\omega. \tag{17}$$

The airfoil with the linear and torsional springs affixed is shown in Figure 3. The governing equations for the airfoil with two degrees of freedom, expressed in dimensional form, are

$$m_o\ddot{h} + S_\alpha\ddot{\alpha} + D_h\dot{h} + K_h h = Q_h, \tag{18}$$

$$S_\alpha\ddot{h} + I_\alpha\ddot{\alpha} + D_\alpha\dot{\alpha} + K_\alpha(\alpha - \alpha_o) = Q_\alpha. \tag{19}$$

where h is the vertical displacement, m_o is the airfoil mass per unit span, S_α is the mass static moment, I_α is the mass moment of inertia, K_h and K_α are the spring stiffness coefficients, and D_h and D_α are the structural damping coefficients. Q_h is the net applied aerodynamic force in the vertical direction, while Q_α is the net applied aerodynamic pitching moment.

The transformation of the airfoil equations of motion to a first-order, coupled system proceeds via the straightforward substitutions, $y_1 = h$, $y_2 = \dot{h}$, $y_3 = \alpha$, and $y_4 = \dot{\alpha}$, leading to

$$\begin{aligned}
\dot{y}_1 &= y_2, & (20)\\
\dot{y}_2 &= (Q_h - S_\alpha \dot{y}_4 - D_h y_2 - K_h y_1)/m_o, & (21)\\
\dot{y}_3 &= y_4, & (22)\\
\dot{y}_4 &= (Q_\alpha - S_\alpha \dot{y}_2 - D_\alpha y_4 - K_\alpha (y_3 - \alpha_o))/I_\alpha. & (23)
\end{aligned}$$

The equations, in this form, are then integrated in time using a fourth-order Runge-Kutta algorithm [33]. The integration takes place immediately after the calculation of the aerodynamic coefficients in the main algorithm and proceeds from time t to $t + \Delta t$. The linear and angular accelerations obtained are then returned to provide updated values for the aerodynamic calculations.

2.2 Coordinate Transformation

The equations of motion as presented are applicable to a Cartesian coordinate system. To transform the equations so that they apply to a general curvilinear coordinate system, the chain rule of differentiation is employed. The transformation is from the physical domain (x, y) to the computational domain (ξ, η), where

$$\xi = \xi(x, y), \qquad \eta = \eta(x, y). \tag{24}$$

The direct application of the chain rule then produces the derivative operators

$$\frac{\partial}{\partial x} = \xi_x \frac{\partial}{\partial \xi} + \eta_x \frac{\partial}{\partial \eta}, \tag{25}$$

$$\frac{\partial}{\partial y} = \xi_y \frac{\partial}{\partial \xi} + \eta_y \frac{\partial}{\partial \eta}. \tag{26}$$

Here, the subscripts denote differentiation with respect to time or spatial coordinate. The Jacobian of the inverse transformation is assumed to be non-vanishing [34]:

$$\tilde{J} \equiv x_\xi y_\eta - x_\eta y_\xi \neq 0. \tag{27}$$

The coordinate transformation results in the following form for the Laplace operator [8]:

$$\tilde{J}^2 \nabla^2 \psi = \phi_2 \psi_{\xi\xi} + \phi_1 \psi_{\eta\eta} - 2\phi_3 \psi_{\xi\eta} + \phi_4 \psi_\xi + \phi_5 \psi_\eta = -\tilde{J}^2 \omega. \tag{28}$$

where the transformation coefficients are functions of the metrics and their derivatives,

$$\begin{aligned}
\phi_1 &= x_\xi^2 + y_\xi^2, \\
\phi_2 &= x_\eta^2 + y_\eta^2, \\
\phi_3 &= x_\xi x_\eta + y_\xi y_\eta, \\
\phi_4 &= \tilde{J}^{-1}[\phi_1(y_{\eta\eta} x_\eta - x_{\eta\eta} y_\eta) + \phi_2(y_{\xi\xi} x_\eta - x_{\xi\xi} y_\eta) + 2\phi_3(x_{\xi\eta} y_\eta - y_{\xi\eta} x_\eta)], \\
\phi_5 &= -\tilde{J}^{-1}[\phi_1(y_{\eta\eta} x_\xi - x_{\eta\eta} y_\xi) + \phi_2(y_{\xi\xi} x_\xi - x_{\xi\xi} y_\xi) + 2\phi_3(x_{\xi\eta} y_\xi - y_{\xi\eta} x_\xi)].
\end{aligned}$$

The transformed Laplacian is applied to the Poisson equation for the streamfunction and to the vorticity transport equation, where the latter equation takes the following form:

$$\omega_t + \hat{u}\omega_\xi + \hat{v}\omega_\eta = \frac{1}{Re}\nabla^2 \omega + \hat{f}_1 - \hat{f}_2, \tag{29}$$

with

$$\hat{u} = \frac{\Psi_\eta}{\tilde{J}} = \frac{1}{\tilde{J}}(\hat{y}_\eta + \psi_\eta), \qquad \hat{v} = \frac{-\Psi_\xi}{\tilde{J}} = -\frac{1}{\tilde{J}}(\hat{y}_\xi + \psi_\xi),$$

$$\hat{f}_1 = \xi_y f_{1\xi} + \eta_y f_{1\eta}, \qquad \hat{f}_2 = \xi_x f_{2\xi} + \eta_x f_{2\eta}.$$

2.3 Aerodynamic Coefficients

The streamfunction-vorticity formulation of the governing equations eliminates pressure as a flow variable. Therefore, an alternate means of calculating pressure is required to obtain the aerodynamic coefficients. The procedure employed is similar to that utilized by Mehta [35]. The pressure is integrated along a path normal to the airfoil surface to establish the pressure at the leading edge; the integration then proceeds along the airfoil upper and lower surfaces to establish the pressure at these locations. It should be noted that the pressure at the leading edge is not required for the calculation of lift, drag, or moment. However, in other applications the surface pressure distribution was required, so the present technique is maintained. The basic approach is to manipulate the components of the momentum equation to yield p_ξ and p_η. The components of the momentum equation require modification to account for the non-inertial character of the airfoil-fixed coordinate frame. The transformation proceeds from Eqs. (6) and (7), and results in

$$u_t + \frac{1}{\tilde{J}}(\Psi_\eta u_\xi - \Psi_\xi u_\eta) \quad + \quad \frac{1}{\tilde{J}}(y_\eta p_\xi - y_\xi p_\eta) = \frac{1}{Re}\nabla^2 u - f_1, \tag{30}$$

$$v_t + \frac{1}{\tilde{J}}(\Psi_\eta v_\xi - \Psi_\xi v_\eta) \quad + \quad \frac{1}{\tilde{J}}(x_\xi p_\eta - x_\eta p_\xi) = \frac{1}{Re}\nabla^2 v - f_2, \tag{31}$$

where the Laplacian operator now refers to the transformed domain as in Eq. (28).

Using the identities

$$x_\xi \nabla^2 u + y_\xi \nabla^2 v = \frac{1}{\tilde{J}}(-\phi_1 \omega_\eta + \phi_3 \omega_\xi), \tag{32}$$

$$x_\eta \nabla^2 u + y_\eta \nabla^2 v = \frac{1}{\tilde{J}}(-\phi_3 \omega_\eta + \phi_2 \omega_\xi), \tag{33}$$

Eqs. (30) and (31) are manipulated to produce

$$p_\xi = \frac{1}{\tilde{J}}\left[\frac{1}{Re}(\phi_3\omega_\xi - \phi_1\omega_\eta) + \Psi_\xi(x_\xi u_\eta + y_\xi v_\eta) - \Psi_\eta(x_\xi u_\xi + y_\xi v_\xi)\right] \\ -x_\xi f_1 - y_\xi f_2 - x_\xi u_t - y_\xi v_t, \tag{34}$$

$$p_\eta = \frac{1}{\tilde{J}}\left[\frac{1}{Re}(\phi_2\omega_\xi - \phi_3\omega_\eta) + \Psi_\xi(x_\eta u_\eta + y_\eta v_\eta) - \Psi_\eta(x_\eta u_\xi + y_\eta v_\xi)\right] \\ -x_\eta f_1 - y_\eta f_2 - x_\eta u_t - y_\eta v_t. \tag{35}$$

On the airfoil surface, Eq. (34) simplifies to

$$p_\xi = \frac{1}{\tilde{J}Re}(\phi_3\omega_\xi - \phi_1\omega_\eta) - x_\xi f_1 - y_\xi f_2. \tag{36}$$

The pressure is first calculated at a node on the far-field boundary using Bernoulli's equation,

$$p_\infty = \frac{1}{2}(1 - u_\infty^2 - v_\infty^2). \tag{37}$$

This is followed by itegration along a line of constant ξ to obtain the pressure at the leading edge of the airfoil,

$$p_{le} = \int_\infty^{le} p_\eta d\eta + p_\infty. \tag{38}$$

The pressure along the upper and lower surfaces is then computed by integration of Eq. (36),

$$p(\xi_b) = \int_{\xi_a}^{\xi_b} p_\xi d\xi + p(\xi_a). \tag{39}$$

The aerodynamic coefficients may then be determined. The chord and normal forces are calculated first, from which the lift and drag coefficients are obtained

$$\begin{aligned} C_c &= 2\oint p dy - \frac{2}{Re}\oint \omega dx, & (40) \\ C_n &= -2\oint p dx - \frac{2}{Re}\oint \omega dy. & (41) \end{aligned}$$

The lift and drag coefficients are obtained by transforming C_c and C_n to the wind reference frame

$$\begin{aligned} C_l &= C_n \cos\alpha - C_c \sin\alpha, && (42) \\ C_d &= C_c \cos\alpha + C_n \sin\alpha. && (43) \end{aligned}$$

Finally, the pitching moment about the center of gravity is determined via

$$C_m = \oint \vec{r}_A \times f_t \hat{n} dA. \qquad (44)$$

where $\vec{r}_A$ is the vector from the center of gravity to the differential area, dA, $\hat{n}$ is a unit outward normal to dA , and f_t is the total force (per unit area) acting on element dA..

2.4 Boundary Conditions

The boundary conditions on the surface of the airfoil are given by Beran and Lutton [9], where Ψ is specified to vanish

$$\Psi = \psi + \hat{y} = 0, \qquad \text{(airfoil surface).} \qquad (45)$$

The no-penetration condition (45) and the no-slip condition require that Ψ_x and Ψ_y vanish on the surface, which is equivalent to the specification

$$\Psi_\eta = 0, \qquad \text{(airfoil surface).} \qquad (46)$$

This specification is used to develop an implicit condition for surface vorticity from the evaluation of the streamfunction at the surface [9]

$$\phi_1 \Psi_{\eta\eta} + \omega \tilde{J}^2 = 0. \qquad (47)$$

The specification of the conditions on the outer computational boundary is complicated by the fact that they are dependent upon $\Omega(t)$. The absolute velocity in the far-field is $\vec{V}_\infty = \cos\alpha\hat{e}_1 + \sin\alpha\hat{e}_2$ expressed in the a-frame coordinate system. From the previous analysis

$$\vec{V}_\infty = \frac{d\vec{R}}{dt} + \vec{u}_\infty + \vec{\Omega} \times \vec{r}, \tag{48}$$

so the relative velocity at the outer boundary is then

$$\begin{aligned} \vec{u}_\infty &= \vec{V}_\infty - \frac{d\vec{R}}{dt} - \vec{\Omega} \times \vec{r} \\ &= u_\infty\hat{e}_1 + v_\infty\hat{e}_2. \end{aligned} \tag{49}$$

Examining the components of the previous equation establishes the expression for the velocity components on the outer computational boundary

$$\vec{u}_\infty = (\cos\alpha - \dot{R}_1 + y\Omega)\hat{e}_1 + (\sin\alpha - \dot{R}_2 - x\Omega)\hat{e}_2. \tag{50}$$

The expressions for the vorticity and streamfunction on the outer boundary are then obtained by differentiation and integration, respectively,

$$\omega_\infty = -2\Omega, \tag{51}$$

$$\Psi_\infty = (\cos\alpha - \dot{R}_1)y - (\sin\alpha - \dot{R}_2)x + \frac{1}{2}\Omega(x^2 + y^2). \tag{52}$$

The disturbance streamfunction on the outer computational domain is then

$$\psi_\infty = \Psi_\infty - \hat{y} = -\dot{R}_1 y + \dot{R}_2 x + \frac{1}{2}\Omega(x^2 + y^2). \tag{53}$$

2.5 Numerical Implementation

The computational coordinates, ξ and η, are discretized and referenced by the indices i and j, respectively:

$$1 \leq i \leq I, \qquad 1 \leq j \leq J.$$

Spatial derivatives in the Laplacian are discretized using second-order accurate, central-difference expressions. The convective terms in the vorticity-transport equation are treated with a hybrid approach [8]. The convective term $\hat{v}\omega_\eta$ is approximated using central differences, while a second-order accurate, upwind difference is applied to the other convective term, $\hat{u}\omega_\xi$. This approach improves the smoothness of the vorticity field in the absence of explicit artificial viscosity.

The aerodynamic equations of motion, (Eqs. (28) and (29)), are integrated in time using a semi-implicit procedure applying LU decomposition, as developed by Beran [8]. The Poisson equation and the viscous terms in the vorticity-transport equation are treated implicitly. The convective terms in the vorticity-transport equation are treated explicitly via a first-order accurate Euler scheme.

The time-integration procedure is written in delta form, with the correction vectors, $\Delta^n\psi$ and $\Delta^n\omega$ defined by

$$\psi^{n+1} = \psi^n + (\psi^{n+1} - \psi^n) \equiv \psi^n + \Delta^n\psi,$$

$$\omega^{n+1} = \omega^n + (\omega^{n+1} - \omega^n) \equiv \omega^n + \Delta^n\omega,$$

where n is the temporal index such that $t = n\Delta t$.

The Poisson equation relating streamfunction and vorticity (Eq. 28), at points away from the airfoil surface, may be recast using operator notation as

$$L\psi^{n+1} + \omega^{n+1} = 0,$$

$$L\Delta^n\psi + \Delta^n\omega = -(L\psi^n + \omega^n) \equiv N_1. \tag{54}$$

Decomposing the Laplace operator into two linear operators, L_1 acting on the interior nodes, and L_2 acting on the nodes adjacent to the airfoil surface, yields

$$L_1\Delta^n\psi_i + L_2\Delta^n\psi_s + \Delta^n\omega_i = N_1, \tag{55}$$

where the subscripts i and s refer to interior and surface nodes, respectively. At the nodes on the airfoil surface, Ψ vanishes, leading to the discrete form of the boundary condition

$$\psi_s^{n+1} + \hat{y} = 0,$$

$$\Delta^n\psi_s = -(\psi_s^n + \hat{y}) \equiv N_2. \tag{56}$$

Likewise, the discrete boundary condition for vorticity on the airfoil surface may be expressed as

$$L_3\psi_i^{n+1} + \omega_s^{n+1} = 0,$$

$$L_3\Delta^n\psi_i + \Delta^n\omega_s = -(L_3\psi_i^n + \omega_s^n) \equiv N_3. \tag{57}$$

The vorticity-transport equation, evaluated at nodes away from the surface, is written in discrete form as

$$\Delta^n\omega - \frac{\Delta t}{Re}L\omega^{n+1} = -(\hat{u}\omega_\xi + \hat{v}\omega_\eta)^n\Delta t + (\hat{f}_1 - \hat{f}_2)\Delta t,$$

or when reexpressed in delta form

$$\Delta^n\omega - \frac{\Delta t}{Re}L\Delta^n\omega = -(\hat{u}\omega_\xi + \hat{v}\omega_\eta)^n\Delta t + \frac{\Delta t}{Re}L\omega^n + (\hat{f}_1 - \hat{f}_2)\Delta t \equiv N_4.$$

The operator $\hat{G}$ is defined such that

$$\hat{G}\Delta^n\omega \equiv \left[I - \frac{\Delta t}{Re}L\right]\Delta^n\omega,$$

$$\hat{G}_i\Delta^n\omega_i + \hat{G}_s\Delta^n\omega_s = N_4. \tag{58}$$

Provided that Δt is held constant, $\hat{G}_i$ and $\hat{G}_s$ are constant matrices. The resulting blocked system of equations, (55-57), can be reduced to a single, banded system for $\Delta^n\psi_i$

$$\mathcal{A}\Delta^n\psi_i = N_4 + \hat{G}_i(L_2N_2 - N_1) - \hat{G}_sN_3, \tag{59}$$

where

$$\mathcal{A} \equiv -(\hat{G}_iL_1 + \hat{G}_sL_3).$$

The matrix $\mathcal{A}$ is time-invariant (for a constant time step and Reynolds number), and is therefore decomposed into the product of lower and upper triangular matrices at the start of the time-integration procedure. Once $\Delta^n\psi_i$ and ψ^{n+1} are calculated, the vorticity can be updated by applying Eqs. (55) and (57):

$$\Delta^n\omega_i = N_1 - L_1\Delta^n\psi_i - L_2N_2, \tag{60}$$

$$\Delta^n\omega_s = N_3 - L_3\Delta^n\psi_i. \tag{61}$$

The far-field boundary conditions, implemented in delta form, are

$$\begin{aligned} \Delta^n\omega_\infty &= -2\Delta^n\Omega, & (62)\\ \Delta^n\psi_\infty + \Delta^n\omega_\infty &= -\Delta^n\dot{R}_1y + \Delta^n\dot{R}_2x + \frac{1}{2}\Delta^n\Omega(x^2+y^2-4). & (63) \end{aligned}$$

Finally, the velocities and aerodynamic coefficients are calculated, and the integration of the airfoil equations of motion accomplished. The aerodynamic coefficients are calculated immediately after the resolution of ψ and ω and are treated as constants over the interval t to $t + \Delta t$. The integration of the airfoil equations of motion (18,19) proceeds over the same interval by subdividing this interval to apply the Runge-Kutta integration, using the constant values for the applied aerodynamic loads. The resulting linear and angular accelerations are then returned to provide up-

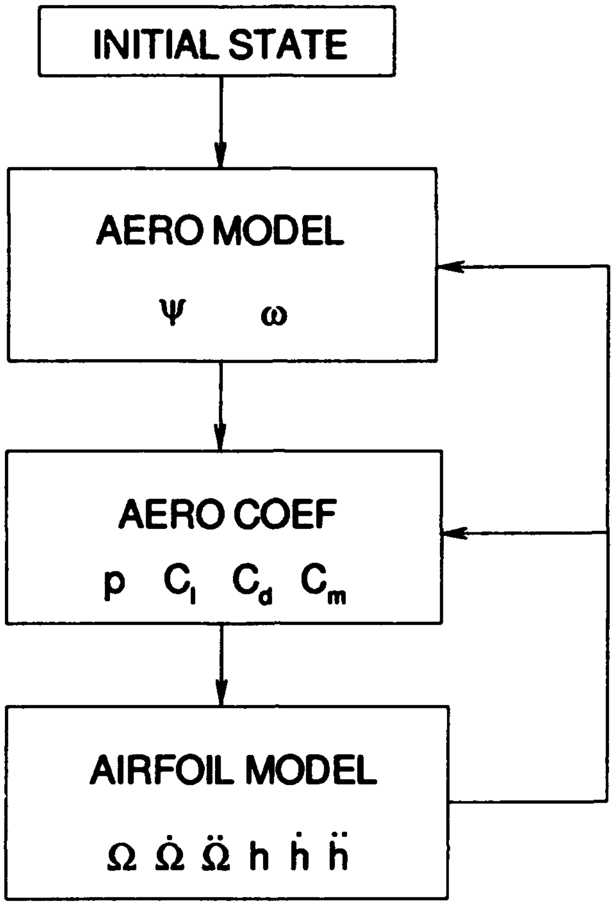
INITIAL STATE
AERO MODEL
Ψ ω
AERO COEF
p C_l C_d C_m
AIRFOIL MODEL
Ω Ω̇ Ω̈ h ḣ ḧ

Figure 4. Flowchart Detailing Implementation of Aerodynamic and Structural Models

dated values for the aerodynamic calculations at the beginning of the next timestep. This introduces a phase lag of up to Δt in the application of the loads, however this is consistent with the first-order accuracy in time of the overall scheme. The implementation of the structural model is detailed in Figure 4. This procedure has been established as robust by comparing airfoil response to a prescribed forcing function. The validation procedure is documented in Appendix A.

III. Results and Conclusions: Part I

3.1 Grid Refinement and Sensitivity

Numerical experiments were conducted with a NACA 0012 airfoil using a variety of C-grids. All grids were constructed with a hyperbolic grid generation algorithm developed by Barth and Kinsey [36]. The grid generation algorithm proceeds from a point distribution specified on the airfoil surface. Hyperbolic partial differential equations are employed to establish the normal point distribution, providing a nearly orthogonal mesh. Grids 1 and 2 are shown in Figures 5 and 6. Table 1 provides the numerical characteristics of the grids, displaying the grid dimensions, the number of nodes on the upper surface (N_u), lower surface (N_l), and wake (N_w), the tangential node spacing at the leading edge (Δs_{le}), and trailing edge (Δs_{te}), and node spacing normal to the surface (Δs_n). Also provided in Table 1 is the distance to the outer boundary (R_d), in chord lengths. Because of computational constraints, the majority of numerical investigations were performed using Grid 1; selected data points were reexamined using other grids.

To assess the impact of grid refinement, the Strouhal number and the critical Reynolds number, Re_{crit}, defined as the Reynolds number at which the flow becomes unsteady, were determined for the fixed airfoil case. The Strouhal number was determined by measuring the period of the oscillations in C_l at $Re = 1200$ for each grid. Re_{crit} was determined by starting from an equilibrium solution, and integrating

C-Grid	I x J	N_u	N_l	N_w	Δs_{le}	Δs_{te}	Δs_n	R_d
1	59x25	20	19	10	.0100	.0200	.0010	2
2	99x40	26	25	24	.0050	.0020	.0010	5
3	139x50	35	34	35	.0040	.0015	.0010	6
4	179x60	40	39	50	.0030	.0010	.0010	7

Table 1. Grid Characteristics

C-Grid	I x J	St	Re_{crit}
1	59x25	0.93	550
2	99x40	0.95	760
3	139x50	0.98	810
4	179x60	0.99	850

Table 2. Strouhal no. at $Re = 1200$ and Hopf points, $\alpha = 0.2$ rad

in time to assess the stability of the initial solution, as in Beran and Lutton [9]. The results are displayed in Table 2. The Strouhal number shows a clear convergence, varying by slightly more than one percent between grids 3 and 4. The Re_{crit} data show a similar convergence, varying by less than five percent between grids 3 and 4. This increased variation is expected, as the determination of Re_{crit} is less precise than the Strouhal number determination.

In addition, the effect of varying the placement of the outer boundary, R_d, was explored. This was accomplished by constructing a series of grids, each with parameters identical to those of Grid 2, except for the variation of R_d. The Strouhal number is determined in each case, again at $Re = 1200$. The results are displayed in Figure 7. The Strouhal number shows very little variation for $R_d > 4$. It should be noted that grid parameters play an important role in this type of investigation. For instance, if the trailing edge spacing, Δs_{te}, is increased to .005 for Grid 2, the Strouhal number decreases to 0.41, clearly inconsistent with the stated results. This is attributed to the failure to resolve flow structure, namely vortices, in the vicinity of the trailing edge. At increased domain sizes ($R_d > 10$) a slight decrease in the Strouhal number is noted, apparently due to an insufficient number of wake points. Considering these effects, it is a necessity to perform at least a limited grid refinement study when addressing similar topics.

3.2 Variation of Natural Frequencies: Single and Dual Axes

The procedure employed to determine the approximate location of Hopf points is explained here. Steady solutions were obtained, using time integration, at very low Reynolds numbers ($Re < 100$). Continuation in Reynolds number was then employed, i.e., the Reynolds number was gradually increased in increments between 10 and 100, depending on the rate of convergence of the previous solution, until an oscillatory solution was obtained. The instantaneous change in Reynolds number introduces perturbations into the numerical flowfield, which are then either numerically damped, or evolve to an unsteady flow. The value of Reynolds number at which the flow becomes unsteady is denoted as Re_{crit}, representing the approximate location of the Hopf point. This procedure is not exact; the main interest being the shift in the Reynolds number between the fixed and moving airfoils. The principal difficulty in this type of investigation is the amount of computational time required to accurately determine the Hopf point. As the structural and inertial properties of the airfoil are varied, the described procedure must be reapplied. However, as the Hopf point is approached, the aerodynamic damping becomes less effective, and a large number of time steps are required to assess the stability of the computation.

Numerical investigations were performed for $\alpha_o = 0.1$ rad and $\alpha_o = 0.2$ rad, where α_o is the value of α at which the torsional spring delivers no moment (cf. Eq. (19)). For each of these, a variety of cases were considered. The natural frequency in pitch, $\omega_\alpha = \sqrt{K_\alpha / I_\alpha}$, was varied from 5 to 50; similarly, the variation of the natural frequency in plunge, $\omega_h = \sqrt{K_h / m_o}$, was varied across the same range. These investigations are undertaken with both axes active (dual axes), and with the complimentary axis disabled (single axis), to assess the influence of the the individual axes, and the axes in tandem, on the location of the Hopf point. In the dual axes case, ω_α was varied, while ω_h was held constant. The structural coupling term, S_α, was initially set to zero.

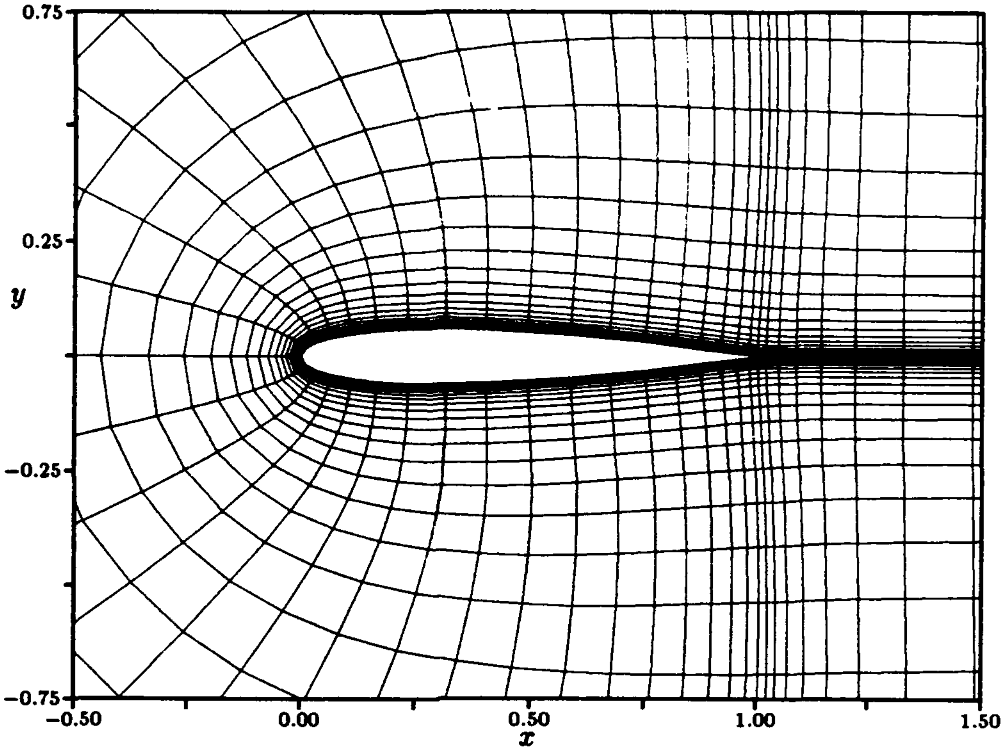

Figure 5. Grid 1 (59x25)

The results for the $\alpha_o = 0.2$ case are shown in Figure 8. The onset of periodic motion for the fixed airfoil, determined by the procedure outlined above, was determined to occur at approximately $Re = 475$. This is reasonably close to the value predicted by a direct method for calculation of the Hopf point, which yields $Re = 550$ for the fixed airfoil [9]. The direct method involves solving an extended set of equations, augmented to capture the eigenvalue migration as the Reynolds number changes (cf. Appendix C). In the direct method, the Reynolds number represents an unknown, and the solution delivers the Reynolds number for which a pair of complex conjugate eigenvalues are migrating across the imaginary axis (cf. Appendix C). This represents a mathematical description of Hopf bifurcation. Two methods are therefore available to determine the Hopf bifurcation point: the direct method and time integration. See Beran and Lutton [9] and Jackson [3] for a detailed presentation of the direct method. The difference in the two methods suggests that

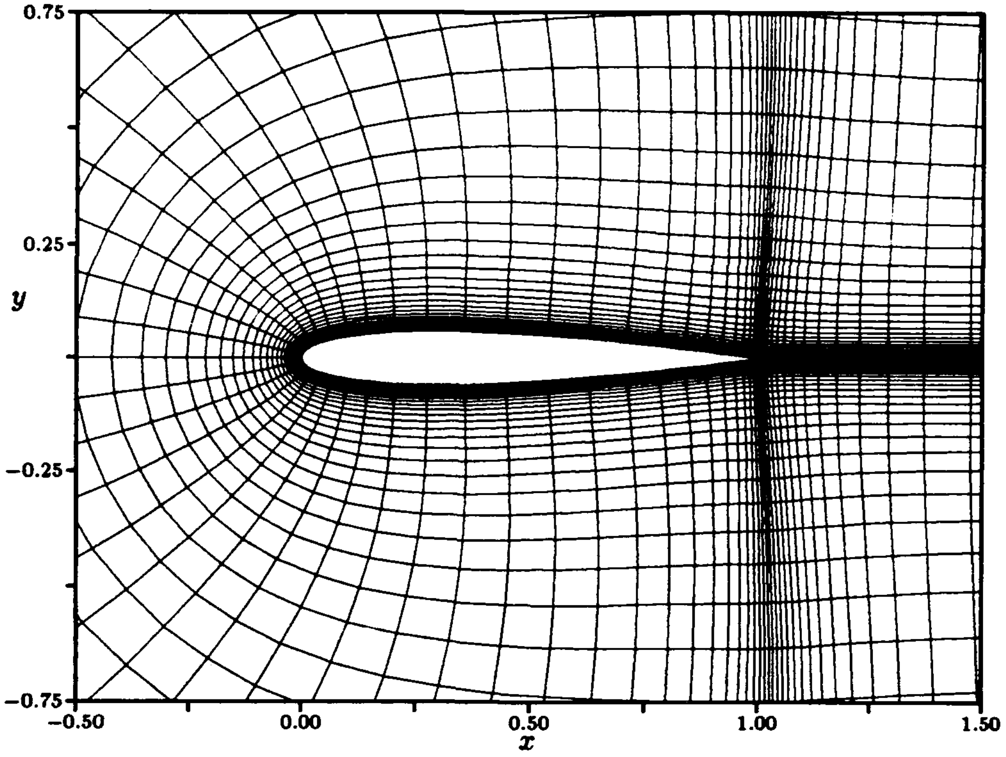

Figure 6. Grid 2 (99x40)

the structure of the Hopf bifurcation is *subcritical*, a question explored further in Sections 3.3 and 3.4. With both axes active, there was a significant reduction in the Reynolds number at which the flow became periodic, to approximately $Re = 300$, across a broad range of ω_α. The exception occurs for values of ω_α below 10. This effect is attributed to the smaller value of K_α employed. The lower value of K_α allows the airfoil to equilibrate to a new, lower angle of attack, for which a larger value of the critical Reynolds number is expected. This is consistent with earlier results [9]. The single-axis experiments are also displayed in Figure 8. The most notable result is that, with the pitch axis fixed, the effect of the vertical axis on the Hopf point location is negligible across the range of ω_h, except at $\omega_h = 5$, where a reduction to $Re = 350$ is noted. This result is due to resonance, since the angular frequency of the aerodynamics, determined by examining the fixed airfoil at $Re = 500$ and $\alpha = 0.2$ rad, is 5.06 rad/sec. It should be noted that the angle of attack was fixed

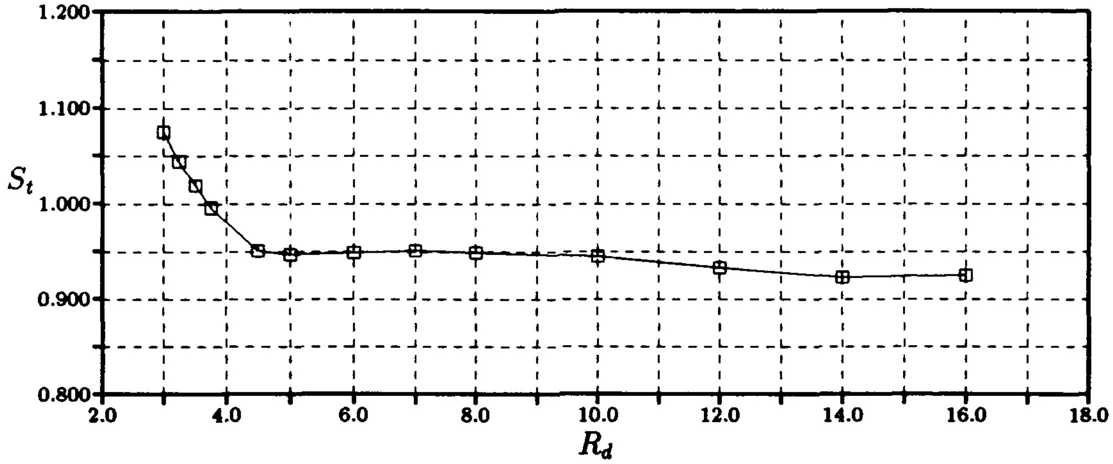

Figure 7. Variation of Strouhal no. with Domain Size

in this case (at $\alpha = 0.2$), unlike the previous case, where α was not fixed. The results of a second, single-axis experiment are also shown in Figure 8. Here, the vertical axis was fixed, and the pitch axis was active. A reduction in the critical Reynolds number was again noted, with the same trend observed for ω_h less than 10. The differences in the critical Reynolds number noted in the dual and single-axis experiments indicate that the axes become coupled via the aerodynamics even in the absence of direct structural coupling. The aerodynamic coupling occurs, and has an effect on the onset of periodic motion, despite the fact that the vertical axis, alone, has a minimal impact for $\omega_h > 10$.

The same set of numerical experiments was then repeated at $\alpha_o = 0.1$ rad to determine if the same trends are evident at a lower angle of attack. See Figure 9. The critical Reynolds number for the fixed airfoil occurs at $Re = 1600$ when applying Re continuation, while the direct solver yields $Re = 2320$. The increased difference between these two numbers, when compared with the $\alpha = 0.2$ case, again indicates the subcritical nature of the bifurcation, and that the bistable region grows as the angle of attack decreases. This may explain the results observed for the vertical axis case: no effect upon the location of the critical Reynolds number for $\omega_h = 50$, however, at lower values of ω_h, the value of the critical Reynolds number is actually *increased.* The differences in the critical Reynolds number observed between the fixed airfoil

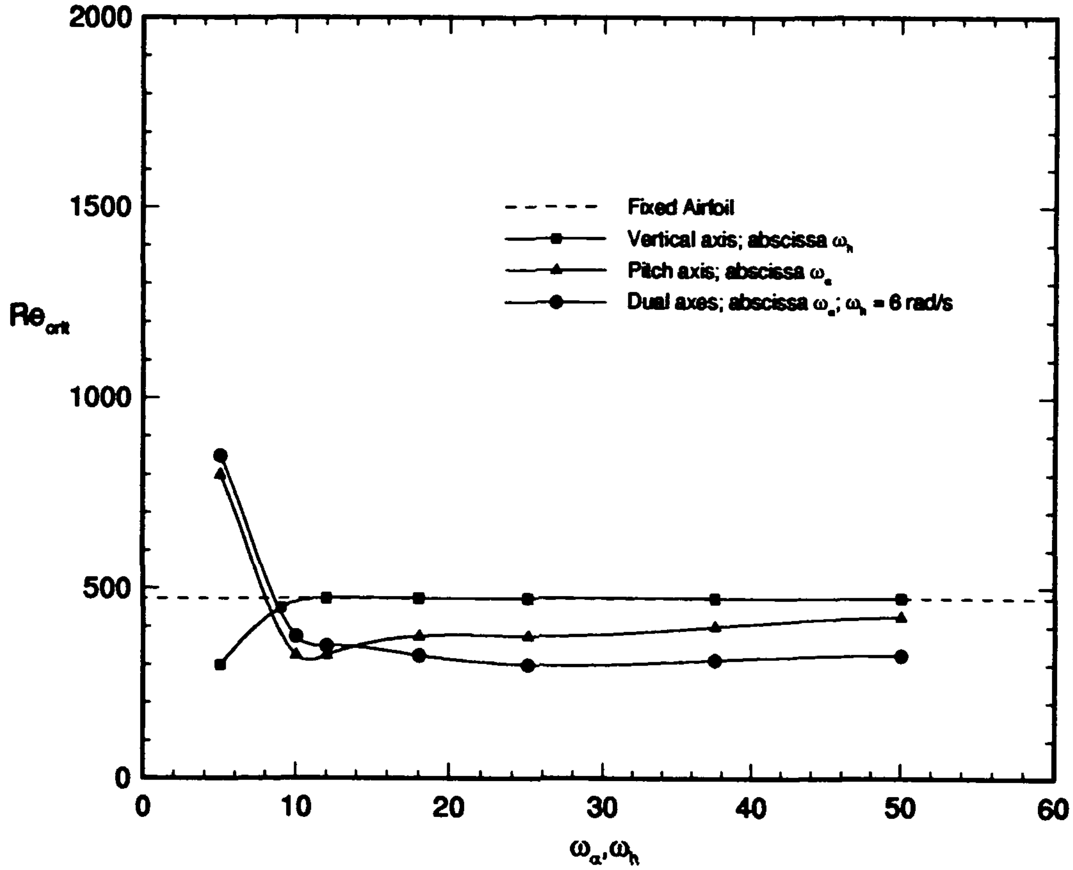

Figure 8. Critical Reynolds no. vs ω, $\alpha = 0.2$ rad

and vertical-axis case indicate that the effect of the structural model is the migration of the stable and unstable periodic orbits associated with the bistable region. That is, the location of the periodic orbits (both stable and unstable branches) in the bistable region are more sensitive to the addition of a structural model than is the actual location of the Hopf point. This may occur because these orbits are inherently periodic, and hence immediately have the potential to excite the airfoil. See Figure 15 for an indication of this effect. Since analysis reveals the vertical axis, singularly, should have no direct influence upon the location of the Hopf bifurcation point, the numerical results presented are attributed to the migration of periodic orbits in the bistable region.

The dual-axis experiments show the same trend (reduction in the critical

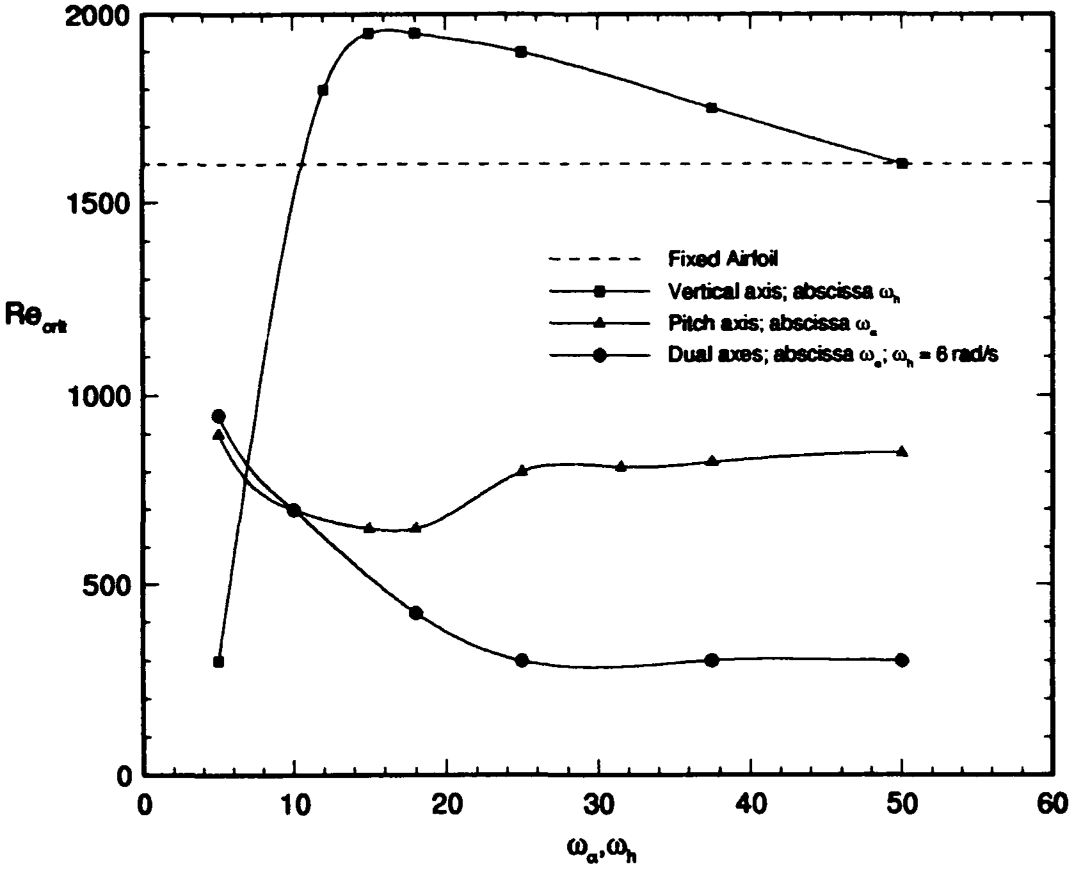

Figure 9. Critical Reynolds no. vs ω, $\alpha = 0.1$ rad

Reynolds number) as the $\alpha_o = 0.2$ case, except that the reduction is of greater magnitude. It is observed that the initial onset of oscillations begins at the *same* Reynolds number, $Re = 300$, for both the $\alpha = 0.1$ and $\alpha = 0.2$ cases with $\omega_\alpha > 10$. The same trend at lower values of ω_α is evident as the airfoil equilibrates to a lower angle of attack. The differences in the value of critical Reynolds number between the dual-axis results and the pitch-axis results are again apparent, but are also of greater magnitude than in the $\alpha_o = 0.2$ rad case.

The effect of structural coupling, S_α, was also examined. The value for the previously discussed data was $S_\alpha = 0.0$. The value of S_α was increased to 0.1, and again to 0.2. With both axes active, $\omega_\alpha = 50$ and $\omega_h = 10$, there was no significant change in the critical Reynolds number for either value of S_α. Since the single-axis and dual-axis experiments demonstrated the influence of coupling, it is probable that the axes are strongly coupled aerodynamically, regardless of the presence of direct structural coupling.

3.3 Influence of Structural Damping

The influence of structural damping, D_α and D_h, was explored next. Since the onset of oscillatory flow is closely related to the ratio of the convective and dissipative phenomena inherent in the flow via the Reynolds number, it is of interest to determine the effect on the onset of oscillations if an additional dissipative mechanism is applied. The results are shown in Figures 10, 11 and 12. These figures present the aerodynamic response, as indicated by C_l, and the structural response of the airfoil, indicated by α and h, as the levels of structural dissipation are varied. A Fourier analysis [37] is also presented to quantify the frequency content of the aerodynamic response. The frequency is presented as Hertz (Hz), here measured as cycles per aerodynamic time unit. The amplitude is scaled such that a constant signal will provide an amplitude equal to its value, while a single-frequency, harmonic signal will provide an amplitude equal to half of its peak-to-peak amplitude.

The results indicate that the effect of increased levels of structural dissipation are dependent upon the Reynolds number. The damping factor, ζ, is defined such that $\zeta = D/D_{crit}$, where D_{crit} represents the critical damping level, here equal to $2\sqrt{m_o K_h}$ for the vertical axis or $2\sqrt{I_\alpha K_\alpha}$ for the pitch axis. All numerical experiments were performed with the damping factor equal for both axes, hence a single value of ζ is given for each result rather than stating a value for each axis. Figure 10 displays the results at $Re = 450, \zeta = 0.5$, representing an underdamped case. The unsteady flow results in oscillatory airfoil motion. As the damping levels are increased to $\zeta = 2.0$ for the same Reynolds number (Figure 11), the airfoil motion is damped and eventually a steady state is achieved. The behavior is different at $Re = 650$, however. When the damping levels were increased to $\zeta = 2.0$, the flow field and the airfoil remain oscillatory, as shown in Figure 12. The difference in these two cases appears to be related to the Hopf bifurcation structure. In the first case, $Re = 450$, the Reynolds number is located in the bistable region (See Figure 15), and the added dissipation has the effect of changing branches from the (stable) limit cycle solution to the (stable) equilibrium solution. Conversely, $Re = 650$ is beyond the bistable region and the added dissipation cannot damp the airfoil motion, as the equilibrium solution in this case is unstable. Further numerical experiments were performed with ζ ranging up to 50. Even at these high levels, the results remained the same: at $Re = 450$ an equilibrium solution was obtained, while at $Re = 650$ oscillations persisted in C_l, α, and h.

Once the Reynolds number has increased past the upper bound of the bistable region, the additional dissipation is seen to reduce the amplitude of the airfoil oscillations, but does not eliminate them, even at very high damping levels ($\zeta = 50$). This result is explained by the nature of the additional dissipation applied. That is, viscosity in the flowfield has an impact whenever velocity gradients develop in the flow, principally in the boundary layer and the wake. In contrast, the structural dissipation is only effective when the airfoil is moving, and is proportional to $\dot{\alpha}$ and $\dot{h}$. Therefore, the impact of the structural dissipation only becomes apparent *after* the airfoil begins to oscillate in either pitch or vertical displacement. In this Reynolds number range (650), the lift coefficient, for example, will remain oscillatory for any level of damping (i.e. the fixed airfoil exhibits oscillatory lift).

3.4 Impact of the Structural Model on the Solution Space

In this section, comparisons are made between the solution spaces for the cases of the fixed and the moving airfoils. The general term "solution space" is employed because it refers to a variety of results: vorticity in the near wake, bifurcation structure, and C_l phase plots. In general, the addition of structural elements to the airfoil tends to produce a more dynamically varying result: additional frequency content, migration of bifurcation points, and an inherently different behavior.

The impact of the structural model on the flowfield is shown in Figures 13 and 14. Both solutions were obtained by integrating from the same initial state at $\alpha = 0.2$ rad using Grid 2. In the case of the fixed airfoil, a steady flow ensues. A small, stationary vortex is seen at the trailing edge. The dissipative, convective and generative forces are in balance: the vorticity generated in the boundary layer is being convected to the stationary vortex at the same rate vorticity is being dissipated from the same structure. In contrast, Figure 14 displays the vorticity when the airfoil is permitted to move. The aerodynamic response is heightened, and vortex shedding occurs. The airfoil is pitching nose down at an instantaneous rate of 0.1 rad/sec, a large region of (negative) vorticity generated in the boundary layer on the upper surface has convected into the lower wake. Behind this vortex, also in the lower wake, is a second region of (positive) vorticity initially generated in the boundary layer on the lower surface. The differences in the vorticity patterns clearly demonstrate that the movement of the airfoil induces the development of unsteady flow before that which would occur for the fixed airfoil.

As discussed earlier, the structure of the Hopf point, when examined using the procedure outlined, appears subcritical. The perturbations introduced into the flowfield, when continuation in Reynolds number is applied, appear to initiate the appearance of undamped, limit-cycle oscillations at a lower Reynolds number than would otherwise be the case. In contrast, if the steady-state solver of Beran [8] is applied, and an equilibrium solution is used as the initial state, then the onset of periodic flow is delayed with respect to Reynolds number. Figure 15 illustrates the structure of the subcritical bifurcation. The results were obtained using Grid 1 at $\alpha = 0.2$ rad. The solid line represents stable equilibrium solutions, obtained using the equilibrium solver of Beran [8]. The equilibrium solutions become unstable at the Hopf point ($Re = 550$), as determined by the direct Hopf solver, and the solid line is replaced by the dashed line. An eigenvalue analysis at $Re = 550$ further demonstrates a conjugate pair of eigenvalues migrating across the imaginary axis [9]. In contrast, no Hopf point is exhibited along the path of equilibrium solutions where the upper and lower branches of the periodic orbits appear to converge. The outer branches of Figure 15 represent the C_l extrema of the limit-cycle oscillations for the fixed airfoil, the vertical axis, and dual axes respectively. The solutions along these branches are obtained by continuation from a previous, oscillatory solution. The results for the fixed airfoil and the vertical axis show a small difference, while the branch associated with the dual-axes case shows a considerable shift, clearly indicating the impact of the structural model on the location of the stable, periodic orbits. It should be noted that, given the subcritical structure of the bifurcation, it becomes problematic to determine if the structural model has an effect on the Hopf point, or whether the principal effect is the migration of the path of periodic orbits associated with the bistable region. In a practical setting, the question may not be of paramount importance, since some level of perturbation is likely in any event: the examination of the periodic orbits in the bistable region would then be of more practical importance.

In order to examine the dynamics of the numerical solutions and to capture the approach to attractors in the solution space (i.e., equilibrium or fixed points and limit cycles), phase plots are introduced. In a C_l phase plot, for instance, $C_l(t)$ is plotted against $C_l(t + \delta t)$, where δt is chosen to be on the order of one-tenth of the period. Thus for these representations, an equilibrium solution is represented by a single point, while a limit cycle represents a single, closed orbit. The shape of the orbit is dependent upon the value chosen for δt. Figure 16a shows the evolution towards a limit cycle for the fixed airfoil, with time integration proceeding from an equilibrium solution at $Re = 1200$, $\alpha = 0.2$ rad, using Grid 2 ($R_d = 14$). The phase plot displays a trajectory emanating from the center (equilibrium state), which then overshoots the stable orbit before contracting back to a fixed amplitude. Figure 16b indicates the corresponding time history. Contrast this solution with the case of the airfoil with the vertical axis active ($\omega_h = 6$ rad/s), displayed in Figure 17. Time integration proceeds from the same equilibrium solution. In this case, the progression to a set of bounding orbits is less regular, and the solution never cleanly approaches an orbit of constant amplitude. This is also indicated in the time history, where additional frequency content and reduced amplitude is evident when compared to the prior case, as indicated in the Fourier analysis of C_l.

It is of interest to consider the difference in the behavior of the two cases in the neighborhood of the equilibrium solution, i.e., to examine the behavior of the small perturbations which ultimately bifurcate the solution to another branch, as in Figure 15. The phase plot of this regime, representing trajectories in the immediate vicinity of the equilibrium solution, is shown in Figure 18 for the fixed airfoil. The choppy character of the plot is due to the finite decimal representation of C_l, but the general trend remains obvious. The trajectories appear to construct an inner structure, as C_l is slightly perturbed about the equilibrium state. However, after leaving this inner region, the trajectory no longer intersects itself (until much later as it approaches a limiting orbit), and proceeds to spiral outward in a regular fashion. Contrast this with the result for the case with the vertical axis active, shown in Figure 19. In this case, the trajectory also spirals outward from the neighborhood of the equilibrium solution. However, the trajectory appears to double back and intersect itself repeatedly, indicating the additional frequency content of the solution. While it may appear macroscopically that the difference between the two cases are initially negligible, with differences appearing only over extended time intervals, these results indicate the nature of the bifurcations are fundamentally different and that the small perturbations about an equilibrium solution behave differently.

The next plot (Figure 20) was extracted from the same data set used to construct Figure 15 (Grid 1, dual axes, $\omega_\alpha = 25$ rad/s, $\omega_h = 6$ rad/s). It is essentially a cross section of Figure 15 and is intended to exhibit the evolution towards a stable limit-cycle solution in the bistable region ($Re = 380$). Time integration proceeds from the center outward in the phase plot (a); the corresponding time history being shown in (b). The interesting point is the apparent influence of the unstable limit-cycle branch which connects the stable limit-cycle branch to the Hopf point. A limit cycle of lesser amplitude than the final, stable limit cycle appears to be approached during the time integration. However, since such a solution must be unstable, the evolution continues to the larger amplitude limit cycle. It is noteworthy that this phenomenon appears uniquely in the bistable region, and was not observed outside of this region, see for example Figure 16. Behavior of this type has also been observed in flutter experiments, see Yang and Zhao [11].

The final plot in this series, shown in Figure 21, is provided to indicate the range of dynamic behavior. The plot represents a case with both axes active, at $Re = 950$, and $\alpha = 0.2$, with $\omega_\alpha = \omega_h = 25$ rad/s, utilizing Grid 2. The phase plot indicates the complex, multiple frequency solutions available to the augmented dynamic system. The multiple frequencies are also apparent in the time history and in the corresponding Fourier analysis.

3.5 Conclusions

The influence of the structural model of the airfoil on the location of the Hopf bifurcation structure has been demonstrated. In general, the structural model allows the development of sustained, limit-cycle oscillations in the flowfield to develop at a lower Reynolds number than would be the case for a fixed airfoil. This effect is most evident when the structural model incorporates multiple degrees of freedom. Coupling between the axes can occur through either direct structural coupling, or indirectly via the aerodynamics. Single-axis experiments demonstrate that the vertical axis has a minimal impact on the value of Reynolds number at which the flow becomes oscillatory in the absense of a resonance effect, while the pitch axis has a more pronounced effect. The effect of structural damping is most pronounced in the bistable region, beyond this region, the structural damping impacts the airfoil motion more strongly than the aerodymanic flowfield, which will remain unsteady regardless of the structural damping level. The structure of the bifurcation is subcritical, as the existence of perturbations in the flowfield can initiate sustained oscillations at a Reynolds number lower than would occur when starting from an initial equilibrium state. The influence of the structural model may be more pronounced on the branch of periodic solutions in the bistable region than on the Hopf point itself. In addition, the structural model is seen to provoke additional frequency content in the time history of C_l, for instance. The addition of structural elements may induce secondary bifurcations which perturb the solution path from a single, closed orbit in phase space to a more complicated orbit. This is true in the long-term time behavior and in the immediate evolution away from an equilibrium solution.

Grid sensitivities to critical parameters such as the Strouhal number and critical Reynolds number are considerable. Relatively minor changes in grid spacing or domain size may have a sizeable effect on numerical results. At a minimum, a limited grid refinement study is therefore required to establish consistent results.

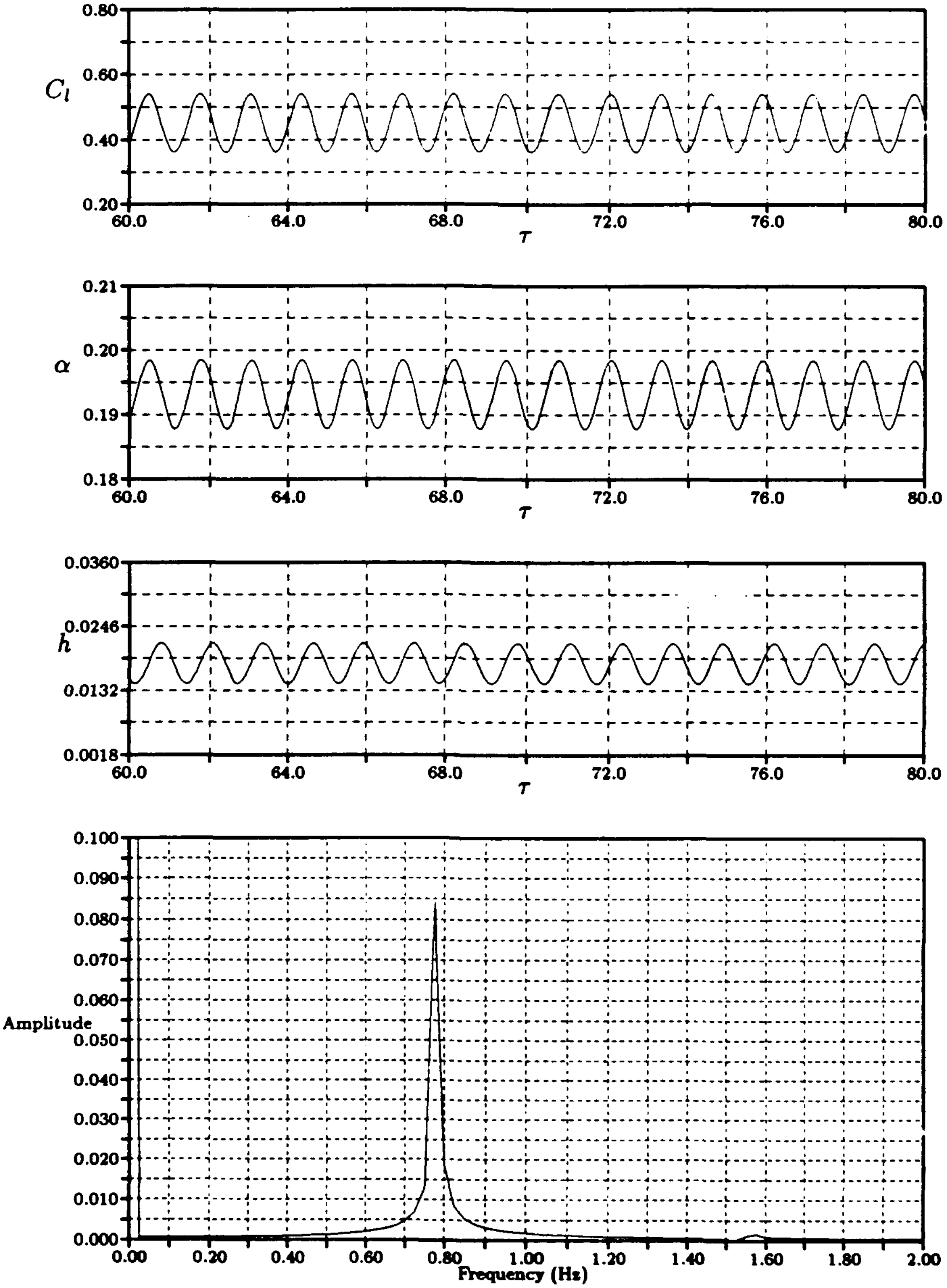

Figure 10. Effect of Structural Damping $Re = 450, \zeta = 0.5$; Fourier Analysis of C_l

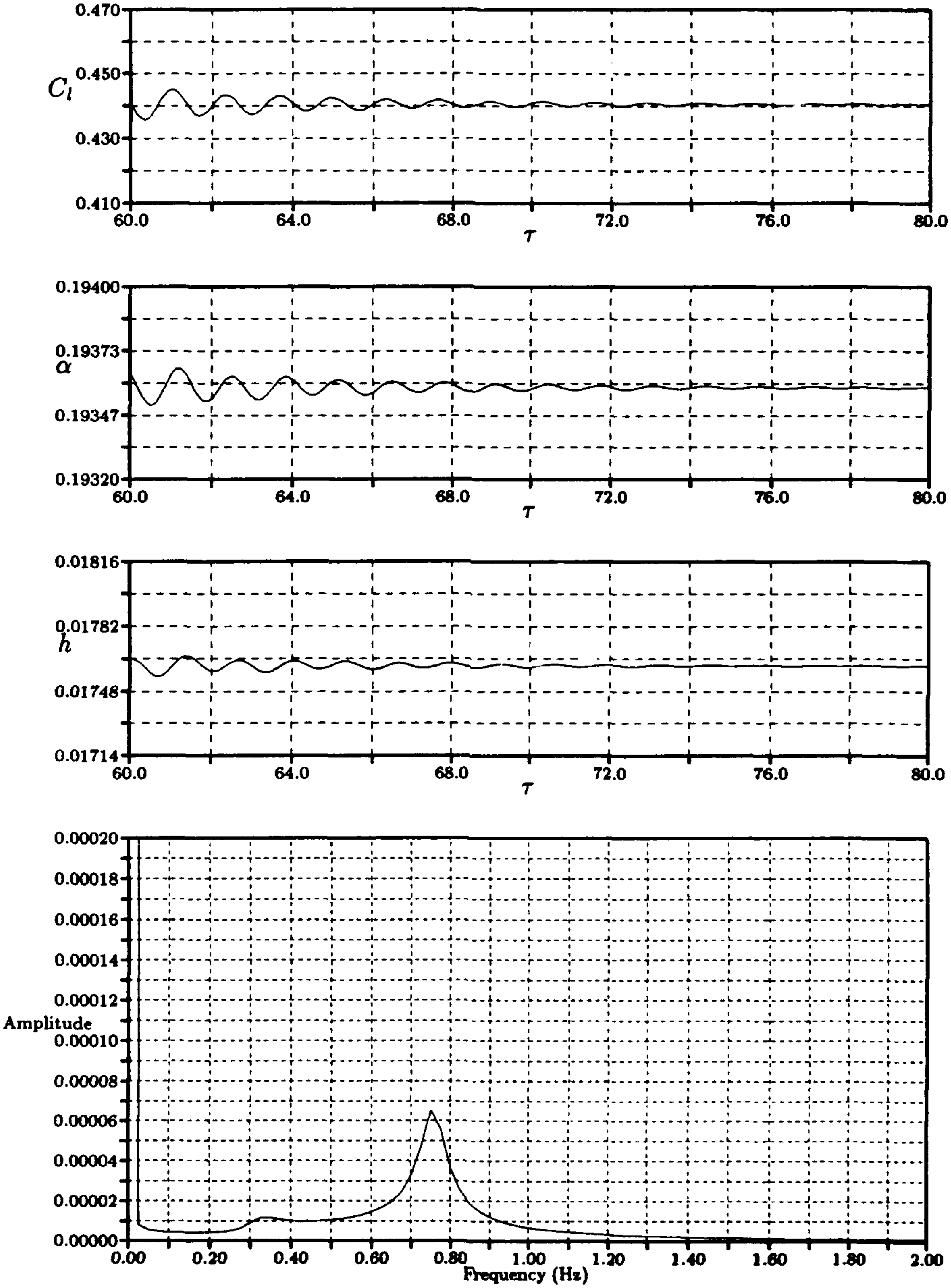

Figure 11. Effect of Structural Damping $Re = 450, \zeta = 2.0$; Fourier Analysis of C_l

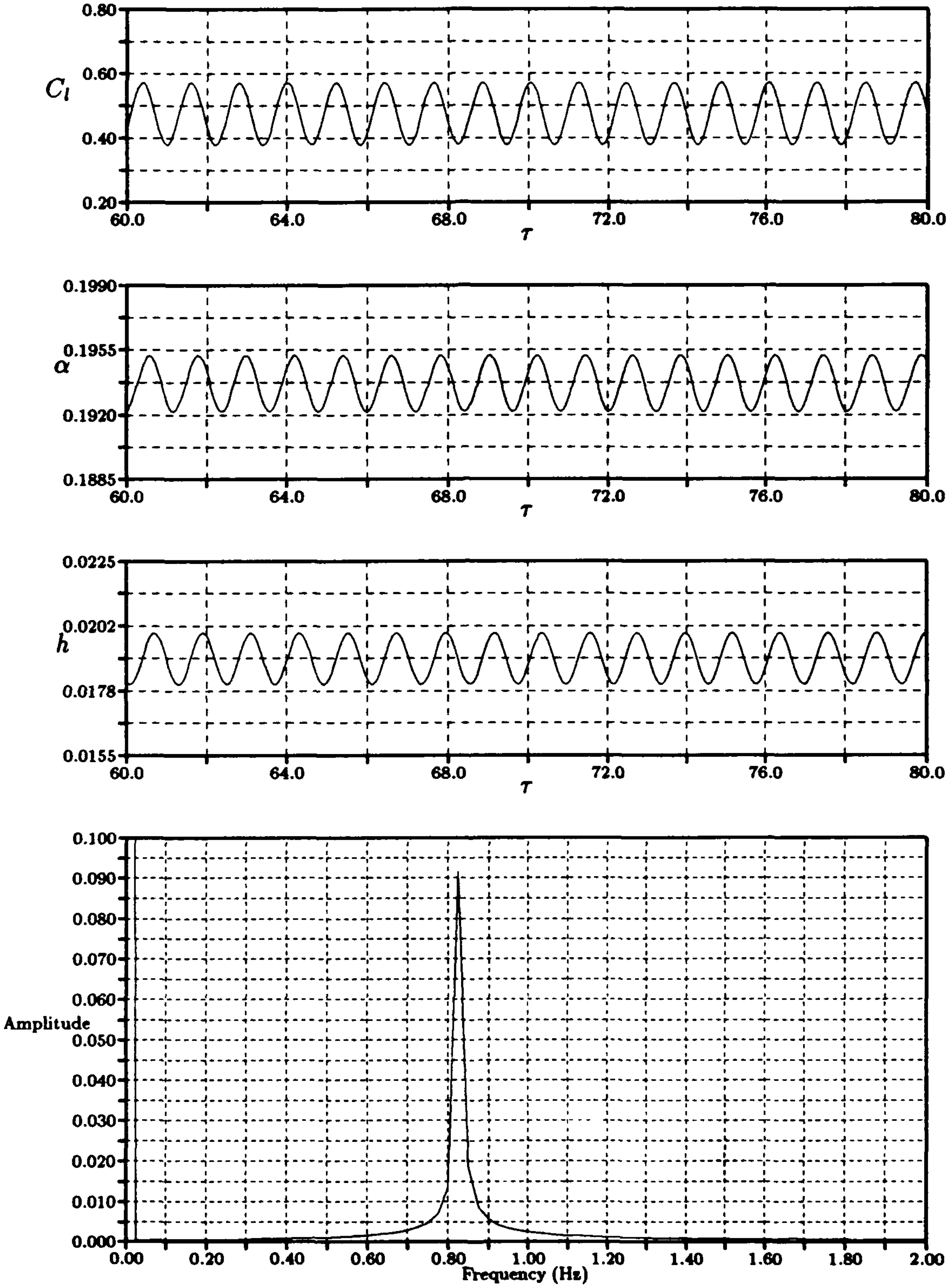

Figure 12. Effect of Structural Damping $Re = 650, \zeta = 2.0$; Fourier Analysis of C_l

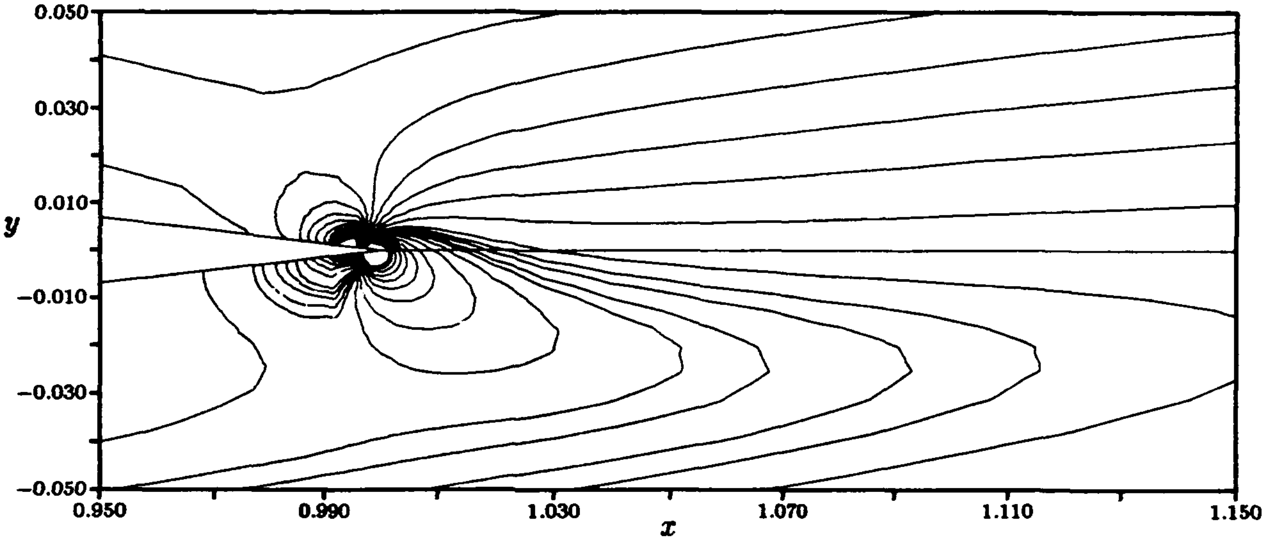

Figure 13. Vorticity in Near Wake, Fixed Airfoil, $Re = 750$

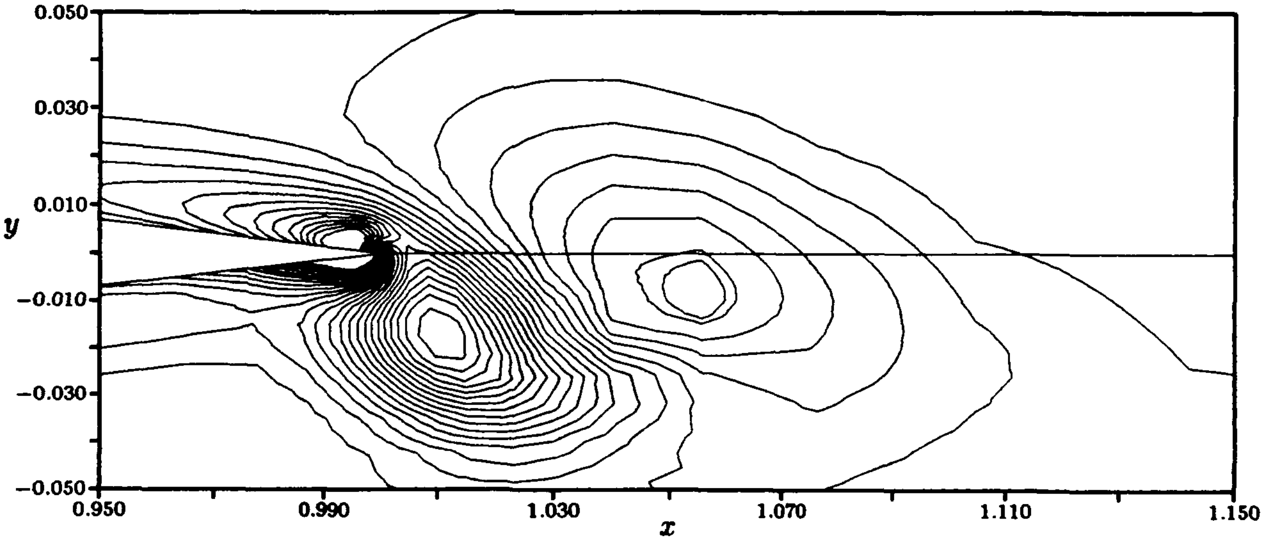

Figure 14. Vorticity in Near Wake, Moving Airfoil, $Re = 750$

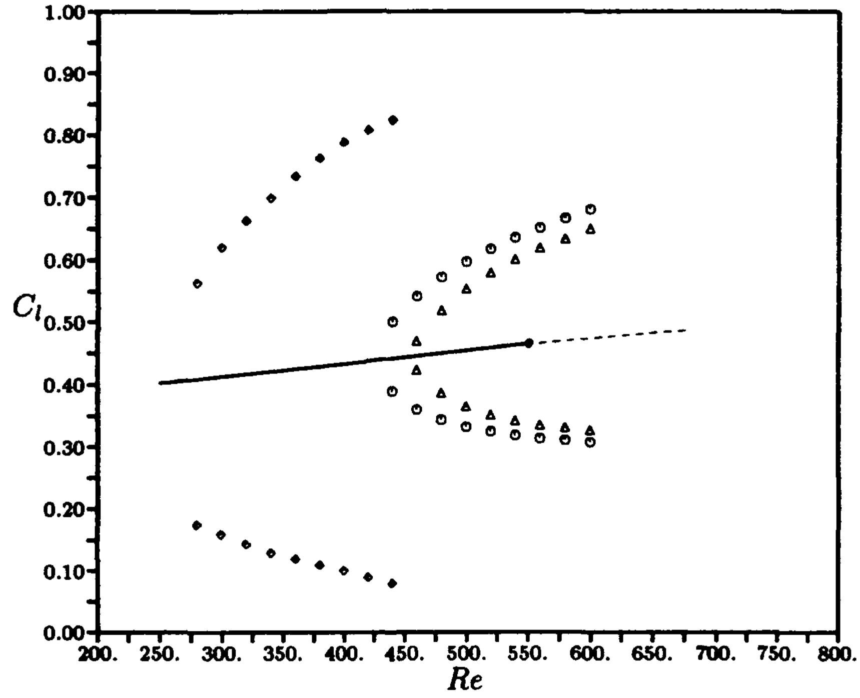

Figure 15. Hopf Bifurcation Structure: $\alpha = 0.2$ rad, Stable Equilibrium Path (solid line), Unstable Equilibrium Path (dashed line), Dual Axes (◇), Fixed Axes (⊙), Vertical Axis (△)

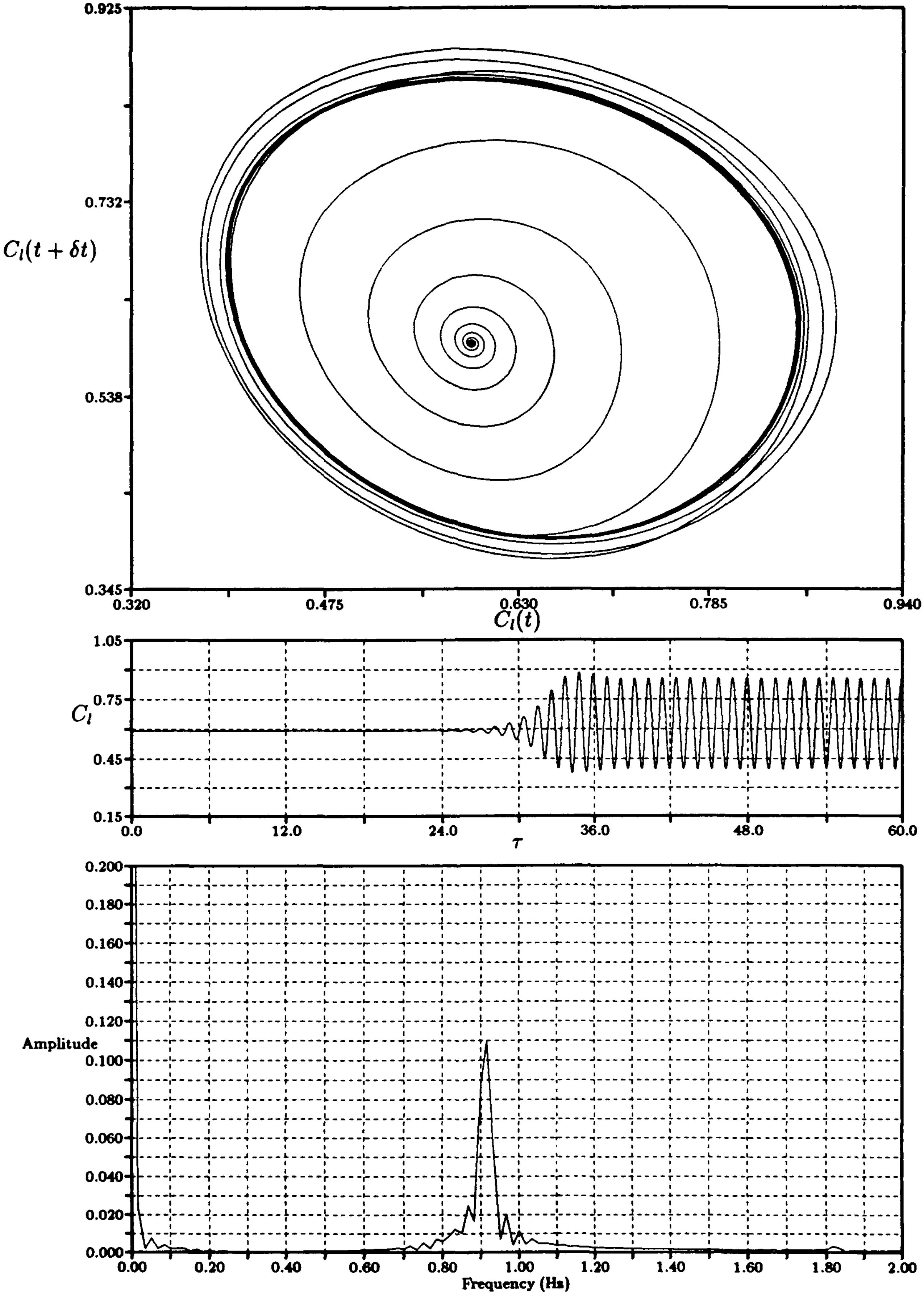

Figure 16. Fixed Airfoil Case, $Re = 1200$, $\alpha = 0.2$ rad: (a) C_l Phase Plot (b) Time History (c) Fourier Analysis

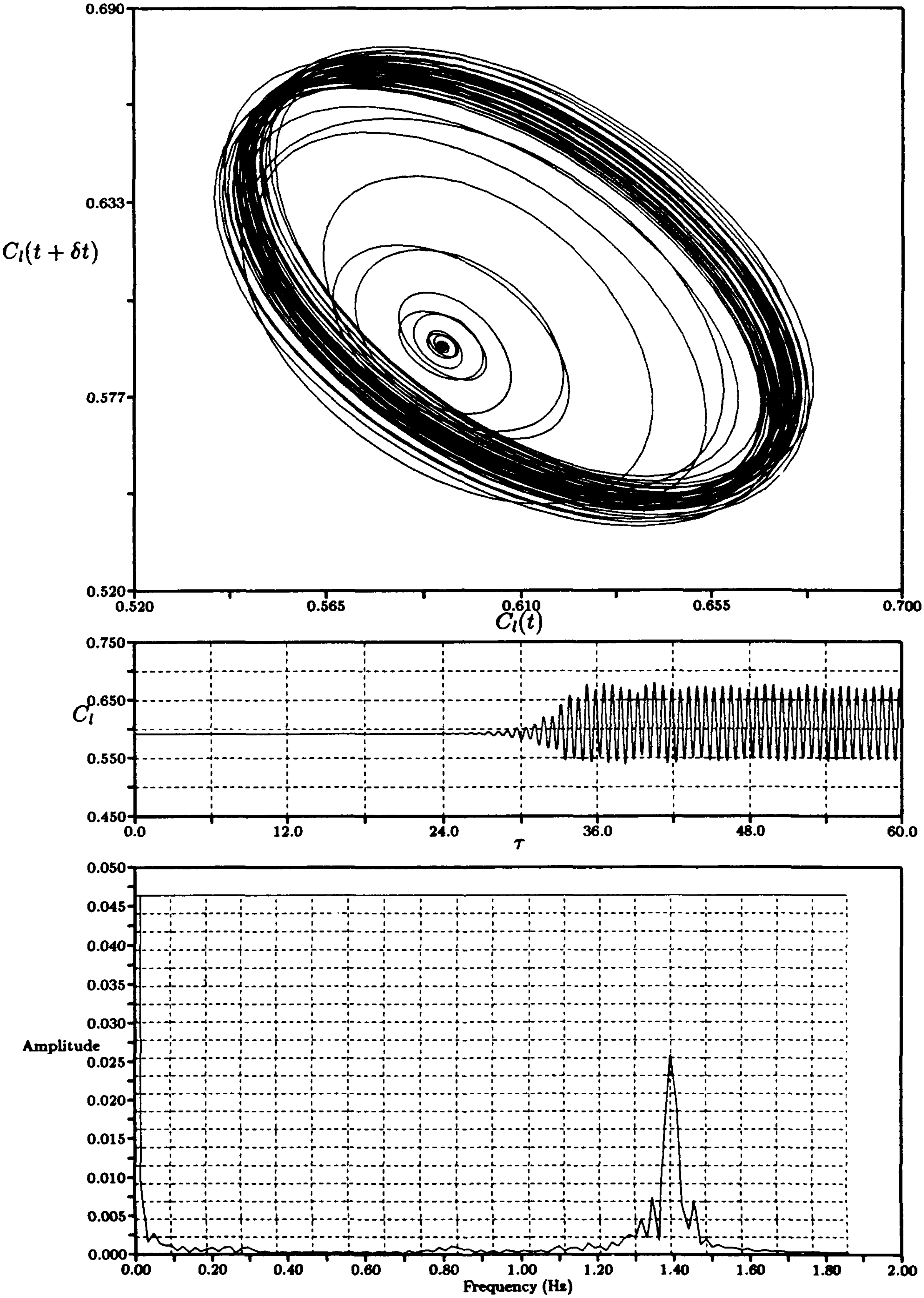

Figure 17. Vertical Axis Case, $Re = 1200$, $\alpha = 0.2$ rad; (a) C_l Phase Plot (b) Time History (c) Fourier Analysis[44]

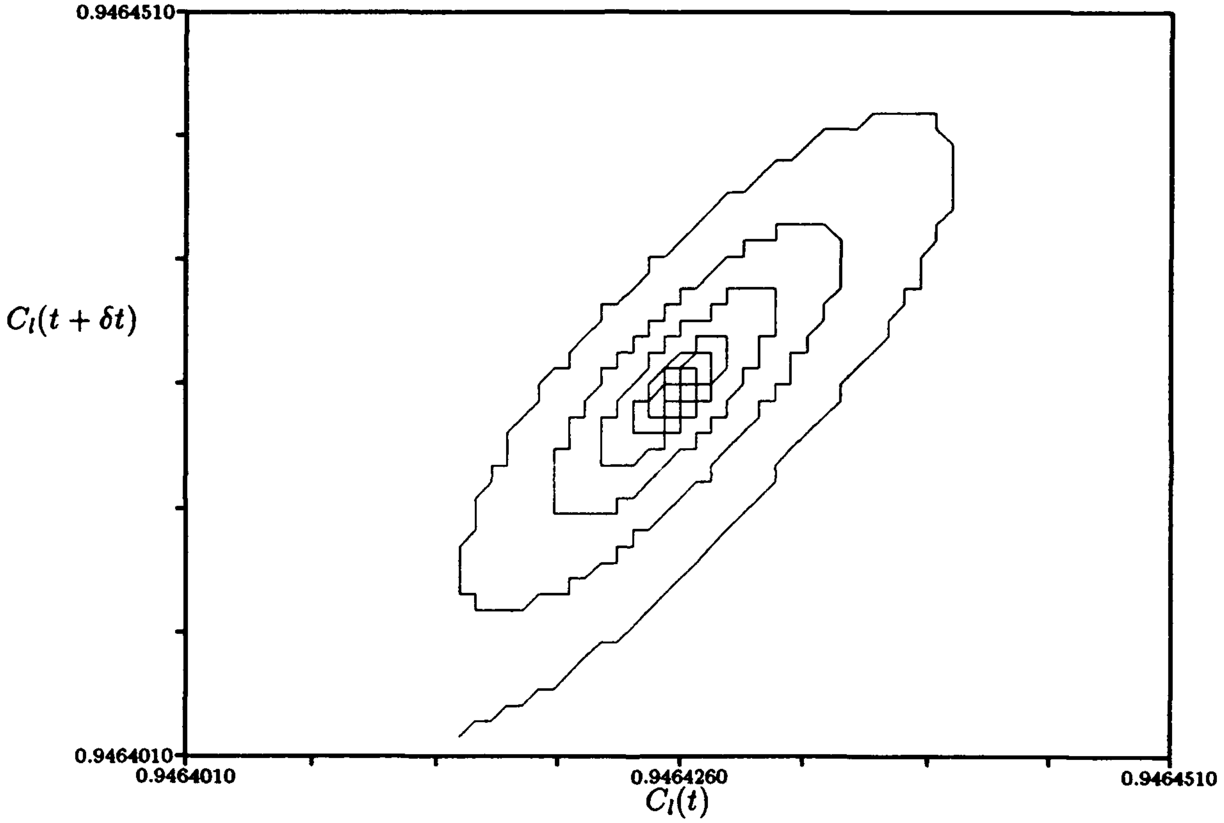

Figure 18. Fixed Airfoil Case, $Re = 1600$, $\alpha = 0.25$ rad; C_l Phase Plot Near Equilibrium

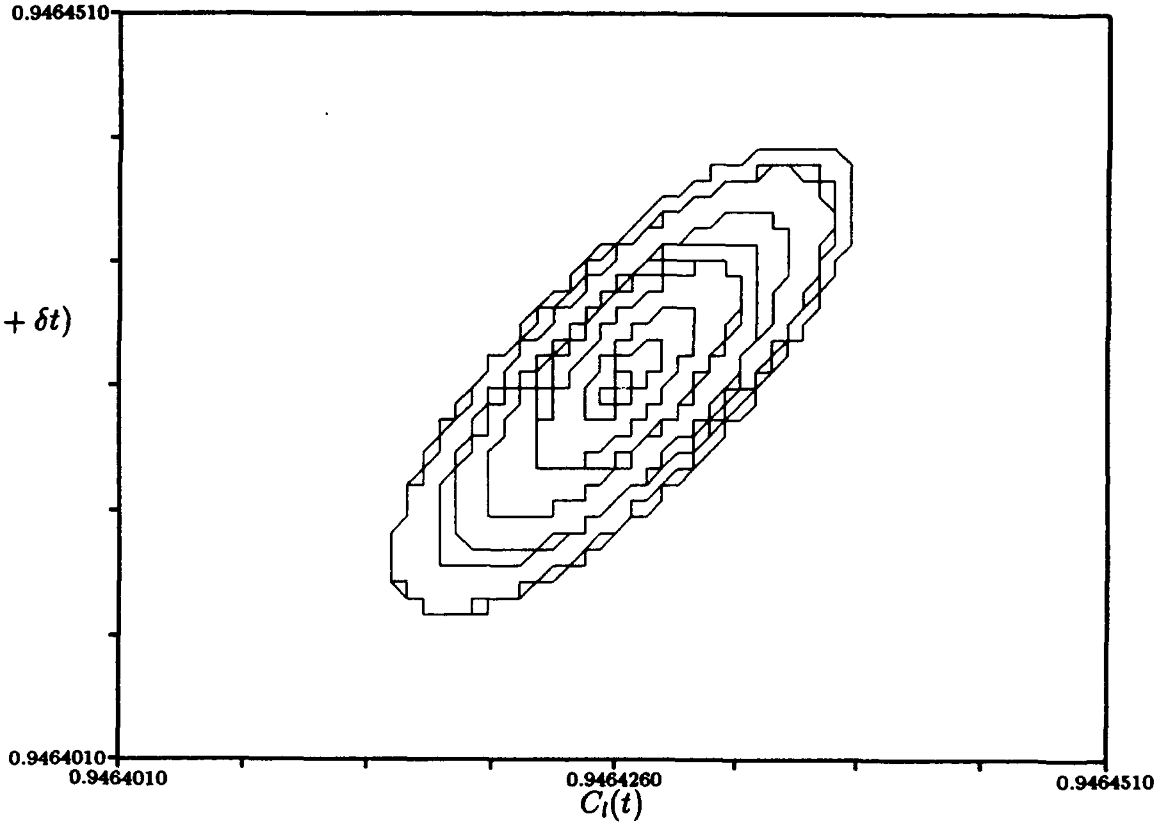

Figure 19. Vertical Axis Case, $Re = 1600$, $\alpha = 0.25$ rad; C_l Phase Plot Near Equilibrium

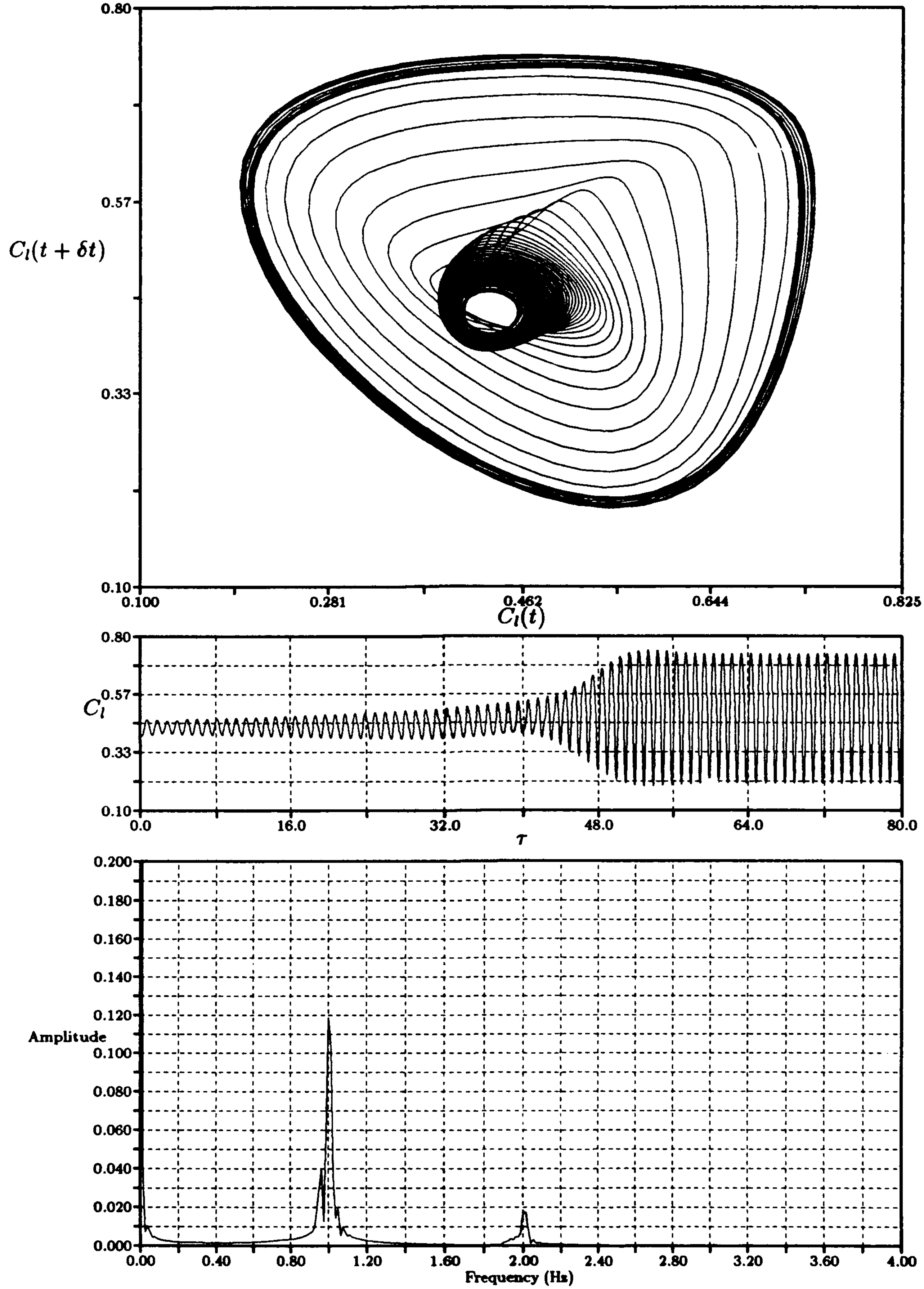

Figure 20. Dual Axes Case, Re = 380, α_o = 0.2 rad; (a) C_l Phase Plot (b) Time History (c) Fourier Analysis

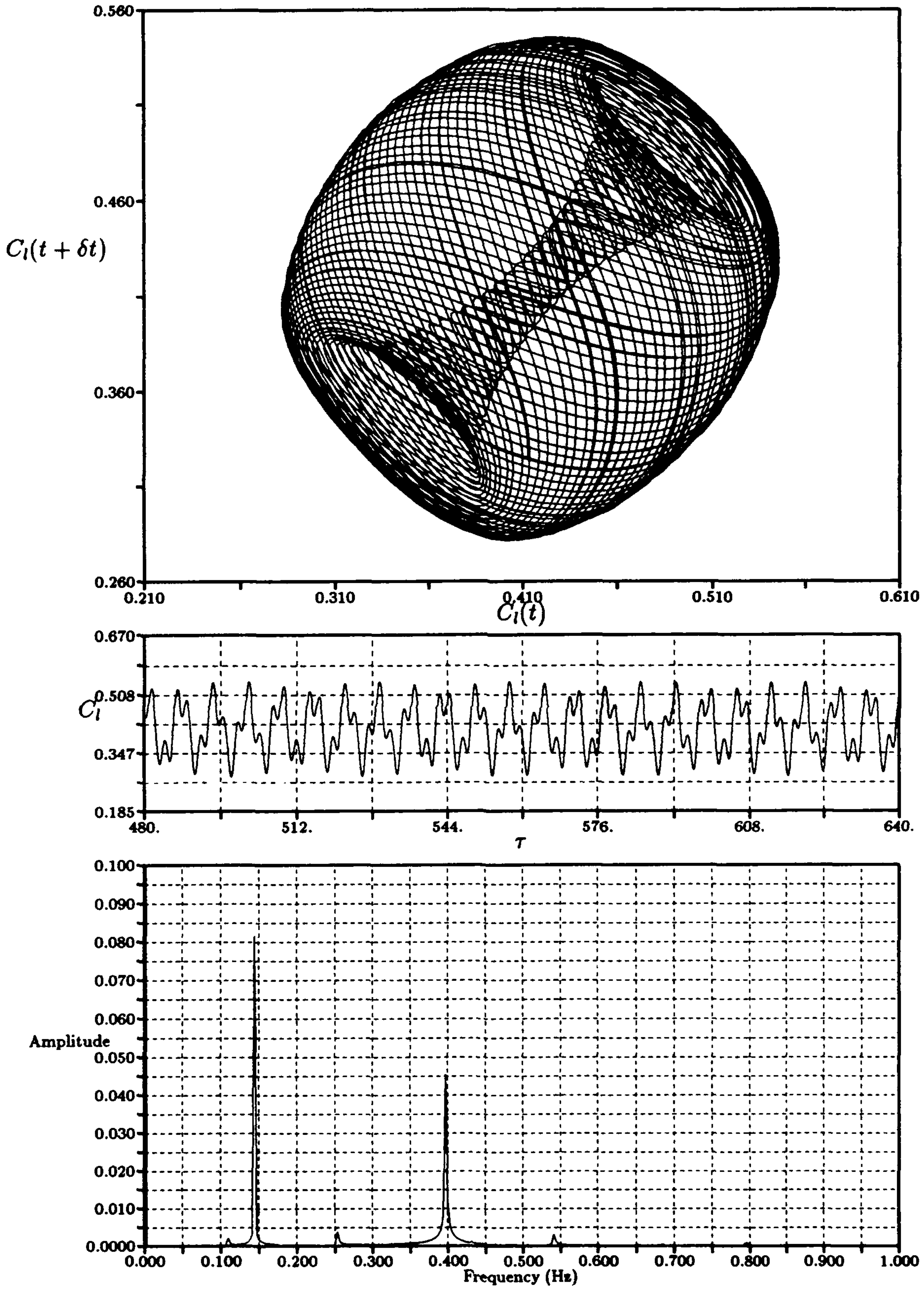

Figure 21. Dual Axes Case, $Re = 950$, $\alpha_o = 0.2$ rad; (a) C_l Phase Plot (b) Time History (c) Fourier Analysis

IV. Analysis: Part II

4.1 Turbulence Model Implementation

One of the most difficult and challenging problems in modern computational fluid dynamics is the correct modeling of turbulent flow. According to Bushnell [38] the importance of turbulence modeling is so paramount that it represents a primary pacing technology in the development of CFD. This is particularly true for complex geometries or flowfields: separated and recirculating flows, dynamic flows, and surfaces with curvature or corners [14].

The turbulence model employed here is a modified version of the algebraic, eddy-viscosity model of Baldwin and Lomax [13] as modified by Knight and Visbal [14]. The primary reason for selecting the Baldwin-Lomax model is the relatively low computational cost and ease of application. In this regard the application is utilized as a tool to capture the relevant physics without resolving the critical issues mentioned above. It is assumed that the Baldwin-Lomax model will perform adequately in the applied regime. There is some justification for this assumption, as the pertinent issue is the determination of the *onset* of unsteady motion. No statement is made about the relevance of the turbulence model after a dynamic flow has evolved. That is, the turbulence model does not necessarily have to accurately model the large-scale, unsteady flow structures mentioned above.

The turbulence model is applied in three separate regions: the boundary layer on the airfoil, the wake proximal to the airfoil trailing edge, and the far-field wake (see Figure 22). The boundary layer of the airfoil is divided into inner and outer regions. In the inner region, the eddy viscosity, ε_i, is given by the Prandtl-Van Driest formula [13]

$$\varepsilon_i = \rho(KYD)^2 \left|\omega\right|, \tag{64}$$

where ω is the vorticity, Y represents the normal distance from the airfoil surface, $K = 0.40$ is the von Karman constant, and the Van Driest damping factor is given by

$$D = 1 - \exp\left[-\frac{Y}{26}\left(\frac{\rho_s|\omega_s|}{\mu_s}\right)^{1/2}\right] \tag{65}$$

The subscript s denotes conditions at the surface (wall).

In the outer region of the boundary layer, the eddy viscosity is defined by

$$\varepsilon_o = \rho K_{cl} C_{cp} Y_{max} F_{max} F_k, \tag{66}$$

where $F_{max} = \max(Y|\omega|D)$, and Y_{max} is the value of Y corresponding to F_{max}. The function F_{max} is maximized over the Y values at a particular station. Values for the constants are taken to be those for an equilibrium incompressible boundary layer [14], for which $C_{cp} = 1.2$, $C_k = 0.65$. The intermitancy factor, F_k, is given by

$$F_k = \left[1 + 5.5(C_k Y/Y_{max})^6\right]^{-1}, \tag{67}$$

and the Clauser constant, $K_{cl} = 0.0168$.

The turbulence model switches from the inner to outer formulation at the first value of Y for which $\varepsilon_i \geq \varepsilon_o$. Transition from laminar to turbulent flow is specified by user input.

The turbulence model in the far-wake is modeled by defining the turbulent eddy viscosity there as [39]

$$\varepsilon_{wk} = \rho C_{wk} \frac{Y_{max} \Delta U^2}{F_{max}} F_k, \tag{68}$$

where

$$C_{wk} = 0.058,$$

$$F_{max} = \max(Y|\omega|),$$
$$\Delta U = (u^2+v^2)^{1/2}_{max} - (u^2+v^2)^{1/2}_{min}.$$

In the wake, Y_{max} is measured from the wake centerline as determined by the location of minimum velocity. The intermitancy factor, F_k, is again obtained from Eq. (67). The value of the constant C_{wk} was chosen to match the theoretical value for an incompressible turbulent wake [40].

In the near-wake, the turbulent eddy viscosity is determined by algebraically smoothing the eddy viscosity profile at the trailing edge to the far-wake profile [39]. The distance to the far wake application was chosen to be of order 10δ, where δ is the average boundary layer thickness at the trailing edge [39].

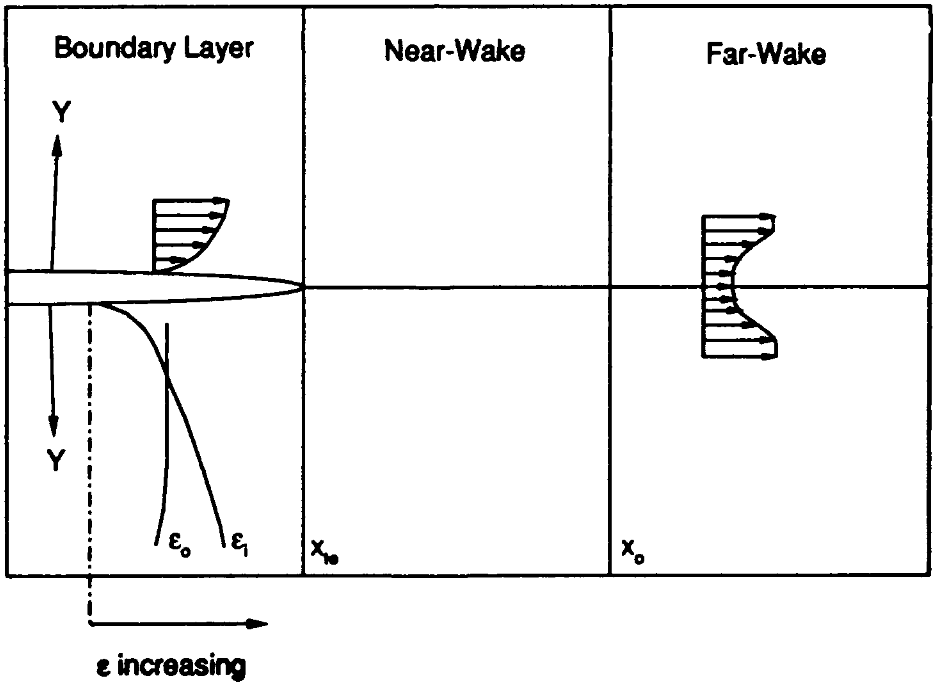

Figure 22. Regions of Application for Turbulence Model

4.2 *Modification of the Incompressible Code*

In order to compare the numerically calculated lift with the lift predicted by Theodorsen's function, it is necessary to forcibly oscillate the airfoil at moderate rotational rates (reduced frequencies, k, greater than 2). The incompressible code utilized in Part I was not robust enough to sustain these rotational rates. At values as low as $k = 2$, computational instabilities arose, and the time history of C_l began to display asymmetric behavior. Difficulties of this type have been experienced by other investigators [41, 42]. The difficulties arose only at increased rotational rates. The low frequencies associated with the initial onset of unsteady motion did not destabilize the computations. Hegna [41] and Mehta [35] have also applied the same procedure with success when the rotational rates were low.

To approach the higher rotational rates, the incompressible code was modified to employ a time-dependent coordinate transformation [34] of the form

$$\xi = \xi(x, y, t), \qquad \eta = \eta(x, y, t), \qquad \tau = t, \tag{69}$$

with transformation metrics given by

$$\begin{aligned} &\xi_x = -y_\eta \tilde{J}^{-1}, \qquad &&\xi_y = -x_\eta \tilde{J}^{-1}, \qquad &&\xi_t = -x_\tau \xi_x - y_\tau \xi_y, \\ &\eta_x = -y_\xi \tilde{J}^{-1}, \qquad &&\eta_y = -x_\xi \tilde{J}^{-1}, \qquad &&\eta_t = -x_\tau \eta_x - y_\tau \eta_y. \end{aligned}$$

The grid speeds are determined by $x_\tau = -\Omega \bar{y}$ and $y_\tau = \Omega \bar{x}$, where $\bar{x}$ and $\bar{y}$ represent the components of the moment arm between the axis of rotation and the point in question (see Figure 23). The Jacobian of the transformation is given by

$$\tilde{J} \equiv x_\xi y_\eta - x_\eta y_\xi \neq 0.$$

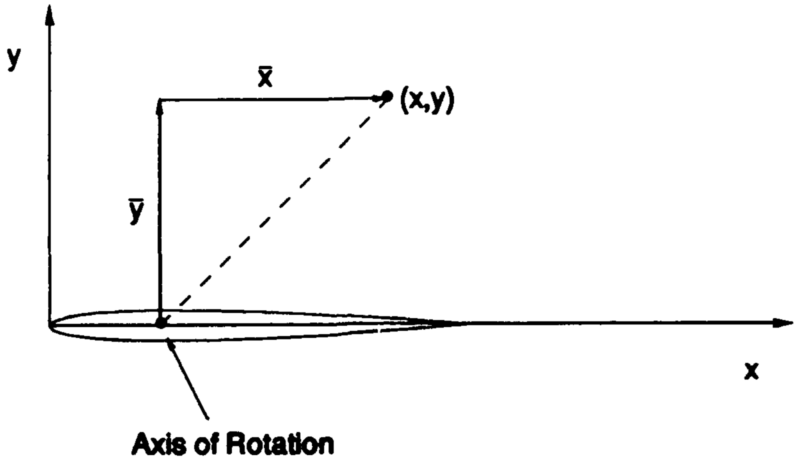

Figure 23. Definition of $\bar{x}, \bar{y}$ Coordinate System

Applying this transformation results in an identical form for the vorticity-transport equation (cf. Eq. (29))

$$\omega_t + \hat{u}\omega_\xi + \hat{v}\omega_\eta = \frac{1}{Re}\nabla^2\omega, \tag{70}$$

provided the convective coefficients are modified as

$$\hat{u} = \Psi_\eta \tilde{J}^{-1} + \xi_t, \qquad \hat{v} = -\Psi_\xi \tilde{J}^{-1} + \eta_t.$$

In a similar fashion, the calculation of pressure presented in Part I (Eqs. (34)-(35)) is modified to produce

$$(u_t + \xi_t u_\xi + \eta_t u_\eta) + \tilde{J}^{-1}(\Psi_\eta u_\xi - \Psi_\xi u_\eta) + \tilde{J}^{-1}(y_\eta p_\xi - y_\xi p_\eta) = \frac{1}{Re}\nabla^2 u, \tag{71}$$

$$(v_t + \xi_t v_\xi + \eta_t v_\eta) + \tilde{J}^{-1}(\Psi_\eta v_\xi - \Psi_\xi v_\eta) + \tilde{J}^{-1}(x_\xi p_\eta - x_\eta p_\xi) = \frac{1}{Re}\nabla^2 v, \tag{72}$$

and these equations are manipulated to yield

$$\begin{aligned} p_\xi = \frac{1}{\tilde{J}}\left[\frac{1}{Re}(\phi_3\omega_\xi - \phi_1\omega_\eta) + \Psi_\xi(x_\xi u_\eta + y_\xi v_\eta) - \Psi_\eta(x_\xi u_\xi + y_\xi v_\xi)\right] \\ -x_\xi(u_t + \xi_t u_\xi + \eta_t u_\eta) - y_\xi(v_t + \xi_t v_\xi + \eta_t v_\eta), \end{aligned} \tag{73}$$

$$p_\eta = \frac{1}{\bar{\bar{J}}}\left[\frac{1}{Re}(\phi_2\omega_\xi - \phi_3\omega_\eta) + \Psi_\xi(x_\eta u_\eta + y_\eta v_\eta) - \Psi_\eta(x_\eta u_\xi + y_\eta v_\xi)\right]$$
$$-x_\eta(u_t + \xi_t u_\xi + \eta_t u_\eta) - y_\eta(v_t + \xi_t v_\xi + \eta_t v_\eta). \qquad (74)$$

The quantities ϕ_i are the coefficients associated with the transformed Laplace operator, and are defined in Eq. (28). As in Part I, Eq. (74) is integrated along a line of constant ξ to obtain the pressure at the leading edge of the airfoil, while Eq. (73) is integrated along the upper and lower airfoil surfaces to obtain the pressures there. No further simplification of Eq. (73) is assumed along the airfoil surface.

A fundamental difference in the present approach, as compared with the method presented Part I, is the application of the boundary conditions. In Part I, the equations were expressed in a non-inertial frame, and the inclusion of the apparent body forces (centrifugal, tangential, and Coriolis) accounted for the non-inertial character of the reference frame. For such an approach, the velocities on the airfoil surface are zero and the freestream velocities vary as the airfoil oscillates. Conversely, when applying the time-dependent coordinate transformation, the freestream velocities are fixed and the surface velocities are equal to the actual velocity at a point on the moving surface. This, of course, simplifies the application of the freestream velocities, but complicates those applied on the airfoil surface. The non-zero velocities on the surface necessitate a change in the definition of the operator L_3 (cf. Eq. (57)) and the expression for the discrete boundary condition for vorticity on the airfoil surface

$$L_3\Psi_i + \omega_s + S = 0, \qquad (75)$$

where S represents a known source term arising from the prescribed velocities on the airfoil surface. In delta form, Eq. (75) becomes

$$L_3\Delta^n\psi + \Delta^n\omega = -L_3\psi^n - \omega^n - L_3\hat{y}^{n+1} - S^{n+1}, \qquad (76)$$

where

$$\hat{y} \equiv y\cos\alpha - x\sin\alpha, \tag{77}$$

and the components of S are given by

$$\begin{aligned} S_i^{n+1} = \tilde{J}^{-2}\Big[&-2(\phi_1+\phi_2)a_i^{n+1} + \phi_2 a_{i+1}^{n+1} + \phi_2 a_{i-1}^{n+1} + \phi_1 b_i^{n+1} \\ &+\tfrac{1}{2}\phi_3 b_{i+1}^{n+1} - \tfrac{1}{2}\phi_3 b_{i-1}^{n+1} + \phi_4 c_i^{n+1} + \phi_5 d_i^{n+1}\Big], \end{aligned} \tag{78}$$

and to first-order accuracy in time, which is consistent with the overall time-accuracy of the scheme,

$$\begin{aligned} a_i^{n+1} &= (uy - vx)_i^{n+1} = (uy - vx)_i^n - \Delta t[\dot{\Omega}(y\bar{y} + x\bar{x}) - \Omega^2(x\bar{y} - y\bar{x})]_i^n, \\ b_i^{n+1} &= (2vx_\eta - 2uy_\eta)_i^{n+1} = (2vx_\eta - 2uy_\eta)_i^n + 2\Delta t\dot{\Omega}(\bar{x}x_\eta + \bar{y}y_\eta)_i^n, \\ c_i^{n+1} &= (uy_\xi - vx_\xi)_i^{n+1} = (uy_\xi - vx_\xi)_i^n - \Delta t\dot{\Omega}(\bar{y}y_\xi + \bar{x}x_\xi)_i^n, \\ d_i^{n+1} &= (uy_\eta - vx_\eta)_i^{n+1} = (uy_\eta - vx_\eta)_i^n - \Delta t\dot{\Omega}(\bar{y}y_\eta + \bar{x}x_\eta)_i^n. \end{aligned} \tag{79}$$

The superscript n refers to the temporal index while the subscript i refers to the node index on the airfoil surface. The terms $\bar{x}$ and $\bar{y}$ represent the respective moment arms from a point on the airfoil surface to the center of rotation. The terms Ω and $\dot{\Omega}$ are known from the prescribed nature of the rotation.

In addition, the streamfunction on the surface is now nonzero. Thus Eq. (45) is modified to

$$\Psi_s = \psi_s + \hat{y}_s = -\Omega(\bar{y}y + \bar{x}x) = -\Omega\tilde{r}, \tag{80}$$

$$\tilde{r} \equiv (\bar{y}y + \bar{x}x),$$

leading to

$$\psi_s + \hat{y}_s + \Omega\tilde{r} = 0. \tag{81}$$

In delta form, the surface boundary condition on streamfunction is written as

$$\Delta^n \psi_s = -(\psi_s^n + \hat{y}_s^n) - \Delta^n \hat{y}_s - \Omega^{n+1} \tilde{r}^{n+1}, \tag{82}$$

with first-order accurate approximations

$$\begin{aligned}
\Delta^n \hat{y}_s &= \hat{y}_s^{n+1} - \hat{y}_s^n \\
&= y^{n+1} \cos\alpha - x^{n+1} \sin\alpha - y^n \cos\alpha + x^n \sin\alpha \\
&= (y^{n+1} - y^n) \cos\alpha - (x^{n+1} - x^n) \sin\alpha, \\
\Delta^n \hat{y}_s &\doteq \Delta t (y_\tau \cos\alpha - x_\tau \sin\alpha), \qquad (83)
\end{aligned}$$

and

$$\begin{aligned}
\Omega^{n+1} &\doteq \Omega^n + \Delta t \dot{\Omega}^n, \qquad (84) \\
\tilde{r}^{n+1} &= (\hat{y} y + \hat{x} x)^{n+1}, \\
\tilde{r}^{n+1} &\doteq (\bar{y}^n + y_\tau \Delta t)(y^n + y_\tau \Delta t) + (\bar{x}^n + x_\tau \Delta t)(x^n + x_\tau \Delta t). \qquad (85)
\end{aligned}$$

A comparative Fourier (von Neumann) stability analysis between the approach indicated in Part I and the time-dependent metric approach described in this section is presented in Appendix B. The stability analysis is applied to the linearized, viscous Burger's equation modeling the vorticity-transport equation.

4.3 The Genesis of Theodorsen's Function

The unsteady aerodynamic forces on an oscillating airfoil in potential flow were determined by Theodorsen [15] in 1935. The development is based on potential flow theory and an assumed distribution of circulation in the wake. The magnitude of the circulation is established by imposing the Kutta condition at the airfoil trailing edge. The solution is resolved into Bessel functions of the first and second kind, and is expressed in terms of the reduced frequency k. Small perturbations about an equilibrium solution are applied and the resultant motion is assumed harmonic. The development of the velocity potentials proceeds by dividing them into two groups: those due to the noncirculatory flow, and those due to circulatory flow.

Pursuing the noncirculatory potentials first, the airfoil is represented by a unit circle (see Figure 24). The potential of a source of strength ϵ at the origin is given by [15]

$$\varphi = \frac{\epsilon}{4\pi} \log(x^2 + y^2). \tag{86}$$

For a source ϵ at (x_1, y_1) on the unit circle, the potential is

$$\varphi = \frac{\epsilon}{4\pi} \log[(x - x_1)^2 + (y - y_1)^2]. \tag{87}$$

Placing a double source 2ϵ at (x_1, y_1) and a double negative source at $(x_1, -y_1)$, the potential becomes

$$\varphi = \frac{\epsilon}{2\pi} \log \frac{(x - x_1)^2 + (y - y_1)^2}{(x - x_1)^2 + (y + y_1)^2}. \tag{88}$$

The function φ on the unit circle provides, upon integration, the surface potential of line pq (see Figure 24). To determine the potential due to α, substitute for the source strength

$$\epsilon = -U\alpha b, \tag{89}$$

where U is the freestream velocity, and b is the half-chord. Taking $y = \sqrt{1 - x^2}$ on the unit circle and integrating yields the potential due to angle of attack,

$$\varphi_\alpha = \frac{-U\alpha b}{2\pi} \int_{-1}^{1} \log \frac{(x - x_1)^2 + (y - y_1)^2}{(x - x_1)^2 + (y + y_1)^2} dx_1, \tag{90}$$

or

$$\varphi_\alpha = U\alpha b\sqrt{1 - x^2}. \tag{91}$$

The potential due to an airfoil in downward motion with a velocity $\dot{h}$ (positive downward) is obtained by substituting $\dot{h}/U$ for α in Eq. (91).

$$\varphi_{\dot{h}} = \dot{h}b\sqrt{1-x^2}. \tag{92}$$

The potential for an airfoil rotating about a point located a distance a (positive to the right) from the midchord point is determined by considering a superposition of potentials. The first being the potential associated with rotation about the leading edge, and the second associated with the vertical motion with velocity $-\dot{\alpha}(1+a)b$. The latter results in a modification to Eq. (92), resulting in

$$\varphi_{\dot{h}} = -\dot{\alpha}(1+a)b^2\sqrt{1-x^2}. \tag{93}$$

The potential due to rotation about the leading edge with angular velocity $\dot{\alpha}$ is described by setting $\epsilon = -(x_1+1)\dot{\alpha}b^2$ in Eq. (88) and integrating

$$\varphi_{\dot{\alpha}LE} = -\frac{\dot{\alpha}b^2}{2\pi}\int_{-1}^{1}\log\frac{(x-x_1)^2+(y-y_1)^2}{(x-x_1)^2+(y+y_1)^2}(x_1+1)dx_1, \tag{94}$$

or

$$\varphi_{\dot{\alpha}LE} = \frac{\dot{\alpha}b^2}{2}(x+2)\sqrt{1-x^2}. \tag{95}$$

As indicated, the potential for an airfoil rotating with angular velocity $\dot{\alpha}$ about a prescribed axis of rotation is the sum of Eqs. (93) and (95)

$$\varphi_{\dot{\alpha}} = \varphi_{\dot{\alpha}LE} + \varphi_{\dot{h}}, \tag{96}$$

$$\varphi_{\dot{\alpha}} = \dot{\alpha}b^2(\tfrac{1}{2}x - a)\sqrt{1-x^2}. \tag{97}$$

Employing the extended Bernoulli equation, the local pressure is, to within a spatially invariant function of time

$$p = -\frac{\rho}{2}\left(V^2 + 2\frac{\partial\varphi}{\partial t}\right), \tag{98}$$

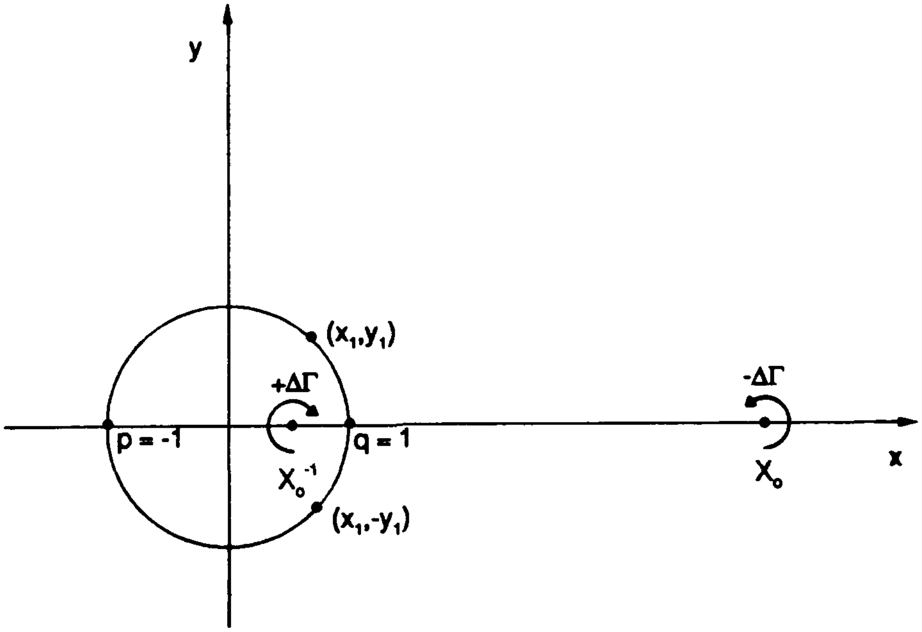

Figure 24. Conformal Map of Wing Profile with Circulation Element in Wake

where V is the local velocity and φ the velocity potential at a point. Substituting $V = U + \frac{\partial\varphi}{\partial x}$, the pressure difference between the upper and lower surfaces at a point x is given by

$$\Delta p = -2\rho\left(U\frac{\partial\varphi}{\partial x} + \frac{\partial\varphi}{\partial t}\right). \tag{99}$$

Substituting the individual velocity potentials (Eqs. (91) and (97)) into Eq. (99) and integrating produces the net force on the airfoil for the noncirculatory potentials

$$P_o = \int_{-1}^{1} \Delta p dx = -\rho b^2[U\pi\dot{\alpha} - ab\pi\ddot{\alpha}]. \tag{100}$$

In a like manner, the circulatory velocity potentials due to an assumed distribution of circulation of strength $\Lambda(x)$ extending from the trailing edge to $x = +\infty$ (see Figure 24) are derived. The potential at a point (x_1, y_1) on the unit circle due to a vortex element pair of strength $\Delta\Gamma$ is given by Theodorsen [15]

$$\varphi_\Gamma(x_1, y_1) = \frac{\Delta\Gamma}{2\pi}\left[\arctan\left(\frac{y_1}{x_1 - X_o}\right) - \arctan\left(\frac{y_1}{x_1 - X_o^{-1}}\right)\right], \tag{101}$$

Introducing the transformation

$$X_o + X_o^{-1} = 2x_o, \tag{102}$$

or on the x axis

$$X_o = x_o + \sqrt{x_o^2 - 1}, \tag{103}$$

with the further substitutions (on the unit circle)

$$x_1 = x, \tag{104}$$

$$y_1 = \sqrt{1 - x^2}, \tag{105}$$

provides

$$\varphi_\Gamma(x_1, y_1) = -\frac{\Delta\Gamma}{2\pi} \arctan\left(\frac{\sqrt{1-x^2}\sqrt{x_0^2 - 1}}{1 - x x_o}\right). \tag{106}$$

Equation (106) gives the clockwise circulation about the airfoil due to the vortex element $-\Delta\Gamma$ at x_o. The extended Bernoulli equation (Eq. (99)) is again applied. However, the vortex element $-\Delta\Gamma$ is regarded as convecting to the right relative to the airfoil with velocity U

$$\frac{\partial\varphi}{\partial t} = \frac{\partial\varphi}{\partial x_o}\frac{\partial x_o}{\partial t} = \frac{\partial\varphi}{\partial x_o}U. \tag{107}$$

Hence Bernoulli's equation is written

$$p = -2\rho U\left(\frac{\partial\varphi}{\partial x} + \frac{\partial\varphi}{\partial x_o}\right). \tag{108}$$

Differentiation of Eq. (106) provides

$$\frac{\partial\varphi}{\partial x} = \frac{\Delta\Gamma}{2\pi}\frac{\sqrt{x_o^2 - 1}}{(x_o - x)\sqrt{1 - x^2}}, \tag{109}$$

and

$$\frac{\partial \varphi}{\partial x_o} = \frac{\Delta \Gamma}{2\pi} \frac{\sqrt{1-x^2}}{(x_o - x)\sqrt{x_o^2 - 1}}. \tag{110}$$

Integration provides the force on the airfoil due to the element $-\Delta\Gamma$

$$\Delta P_\Gamma = -2\rho U b \frac{\Delta \Gamma}{2\pi} \int_{-1}^{1} \left(\frac{\partial \varphi}{\partial x} + \frac{\partial \varphi}{\partial x_o} \right) dx, \tag{111}$$

$$\Delta P_\Gamma = -\rho U b \Delta \Gamma \frac{x_o}{\sqrt{x_o^2 - 1}}. \tag{112}$$

Further integration, with $\Delta\Gamma = \Lambda dx_o$ along the wake, provides the total circulatory force on the airfoil

$$P_\Gamma = -\rho U b \int_1^\infty \frac{x_o}{\sqrt{x_o^2 - 1}} \Lambda dx_o. \tag{113}$$

The magnitude of the circulation is determined by imposing the Kutta condition, requiring that the velocity components are finite at the trailing edge

$$\frac{\partial}{\partial x}(\varphi_\alpha + \varphi_{\dot\alpha} + \varphi_\Gamma) \neq \infty. \tag{114}$$

Introducing the velocity potentials (Eqs. (91),(97), and (106)), Eq. (114) is further expressed by the relationship

$$Q \equiv \frac{1}{2\pi} \int_1^\infty \frac{\sqrt{x_o + 1}}{\sqrt{x_o - 1}} \Lambda dx_o = U\alpha + b(\tfrac{1}{2} - a)\dot\alpha. \tag{115}$$

The distribution of circulation in the wake is assumed harmonic, with the substitution

$$\Lambda = \Lambda_o \exp\{i[k(s/b - x_o) + \phi]\}, \tag{116}$$

where $s = Ut$ is the distance from the first vortex element to the airfoil, $i = \sqrt{-1}$, and k is the reduced frequency representing the wavelength. The circulatory forces

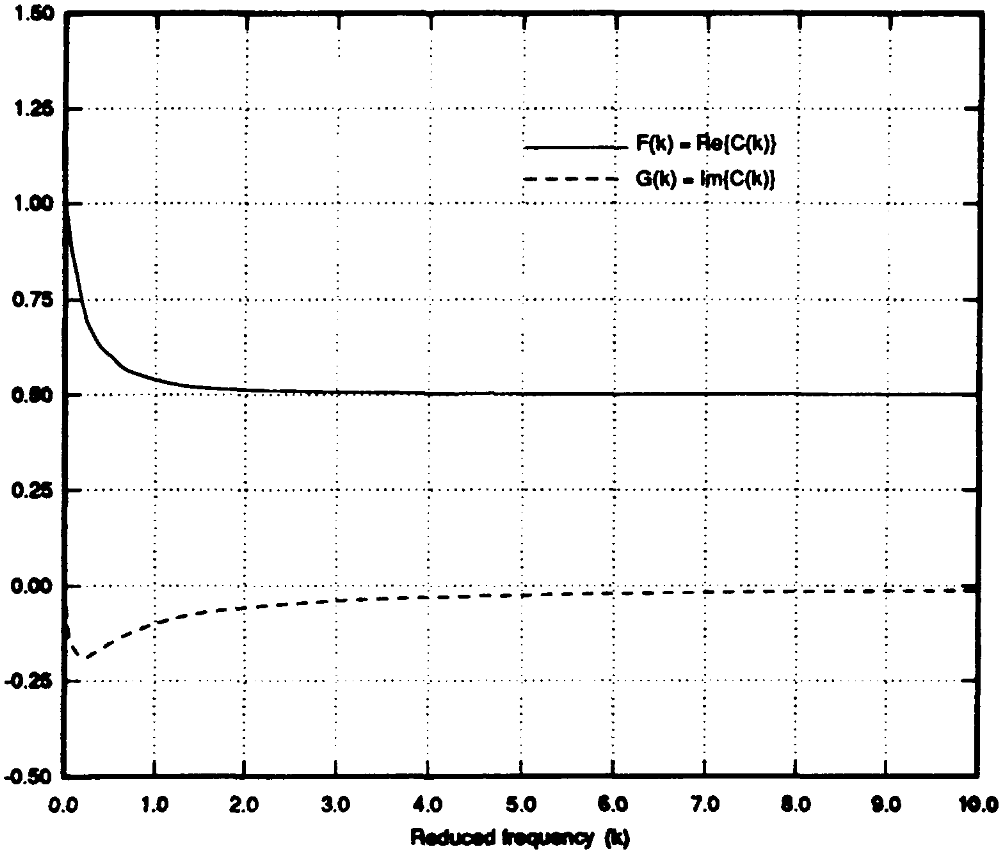

Figure 25. Real and Imaginary Components of the Theodorsen Function

on the airfoil then become

$$P_\Gamma = -2\rho U b\pi Q C(k), \tag{117}$$

where the complex function $C(k)$ is the Theodorsen function, given by

$$C(k) \equiv \frac{\displaystyle\int_1^\infty \frac{x_o}{\sqrt{x_o^2-1}} e^{-ikx_o} dx_o}{\displaystyle\int_1^\infty \frac{x_o+1}{\sqrt{x_o^2-1}} e^{-ikx_o} dx_o}. \tag{118}$$

The real and imaginary parts for the complex function $C(k) = F(k) + iG(k)$ are shown in Figure 25.

The net force on the airfoil is then obtained by summing the forces due to the noncirculatory potentials with those of the circulatory potentials

$$\begin{aligned} P &= P_o + P_\Gamma, \\ &= -\rho\pi b^2(U\dot{\alpha} - ab\ddot{\alpha}) - 2\pi\rho U b C(k)\left\{U\alpha + b(\tfrac{1}{2} - a)\dot{\alpha}\right\}. \end{aligned} \tag{119}$$

The expression for P is then nondimensionalized. Along with a small angle assumption and the substitutions $\theta = -\alpha$, $\dot{\theta} = -(c/U)\dot{\alpha}$, and $\ddot{\theta} = -(c/U)^2\ddot{\alpha}$, the lift coefficient can be expressed as

$$C_k = \tfrac{1}{2}\pi\dot{\theta} + \tfrac{1}{4}a\pi\ddot{\theta} - C(k)\left[2\pi\theta + (\tfrac{1}{2} - a)\pi\dot{\theta}\right]. \tag{120}$$

where the time derivatives of θ are now taken with respect to nondimensional time, i.e., aerodynamic time units nondimensionalized by c/U. This is the form used for comparison with the numerical results. It should be noted that for the steady case

$$\dot{\theta}, \ddot{\theta} \rightarrow 0, \tag{121}$$

with

$$F(k) \rightarrow 1 \text{ and } G(k) \rightarrow 0, \tag{122}$$

so that

$$C_k = -2\pi\theta = 2\pi\alpha. \tag{123}$$

as predicted by thin-airfoil theory [43].

4.4 Beam and Warming Code

The Beam and Warming code of Visbal [27] applied to the two-dimensional, compressible Navier-Stokes equations is utilized for comparison with the modified incompressible code and the results predicted by Theodorsen's function. The Beam and Warming algorithm [44] is an implicit approximate-factorization scheme, and is implemented by Visbal for a moving O-grid configuration. The same time-dependent coordinate transformation described earlier is utilized

$$\xi = \xi(x, y, t), \ \eta = \eta(x, y, t), \ \tau = t.$$

The resulting equations, in strong-conservation law form [39], are

$$\frac{\partial \hat{U}}{\partial t} + \frac{\partial E_1}{\partial \xi} + \frac{\partial E_2}{\partial \eta} =$$

$$\frac{\partial V_1(\hat{U}, \hat{U}_\xi)}{\partial \xi} + \frac{\partial V_2(\hat{U}, \hat{U}_\eta)}{\partial \xi} + \frac{\partial W_1(\hat{U}, \hat{U}_\xi)}{\partial \eta} + \frac{\partial W_2(\hat{U}, \hat{U}_\eta)}{\partial \eta}, \tag{124}$$

where

$$\hat{U} = \tilde{J} \begin{pmatrix} \rho \\ \rho u \\ \rho v \\ \rho e \end{pmatrix}, \tag{125}$$

$$E_1 = \tilde{J} \begin{pmatrix} \rho \mathcal{U} \\ \rho u \mathcal{U} + \xi_x p \\ \rho v \mathcal{U} + \xi_y p \\ (p + \rho e)\mathcal{U} - \xi_t p \end{pmatrix}, \tag{126}$$

$$E_2 = \tilde{J} \begin{pmatrix} \rho \mathcal{V} \\ \rho u \mathcal{V} + \eta_x p \\ \rho v \mathcal{V} + \eta_y p \\ (p + \rho e)\mathcal{V} - \eta_t p \end{pmatrix}, \tag{127}$$

$$V_1 = \tilde{J}\begin{pmatrix} 0 \\ b_1 u_\xi + b_2 v_\xi \\ b_2 u_\xi + b_3 v_\xi \\ b_1 u u_\xi + b_2(v u_\xi + u v_\xi) + b_3 v v_\xi + b_4 T_\xi \end{pmatrix}, \tag{128}$$

$$V_2 = \tilde{J}\begin{pmatrix} 0 \\ c_1 u_\eta + c_2 v_\eta \\ c_3 u_\eta + c_4 v_\eta \\ c_1 u u_\eta + c_2 u v_\eta + c_3 v u_\eta + c_4 v v_\eta + c_5 T_\eta \end{pmatrix}, \tag{129}$$

$$W_1 = \tilde{J}\begin{pmatrix} 0 \\ c_1 u_\xi + c_3 v_\xi \\ c_2 u_\xi + c_4 v_\xi \\ c_1 u u_\xi + c_2 v u_\xi + c_3 u v_\xi + c_4 v v_\xi + c_5 T_\xi \end{pmatrix}, \tag{130}$$

$$W_2 = \tilde{J}\begin{pmatrix} 0 \\ d_1 u_\eta + d_2 v_\eta \\ d_2 u_\eta + d_3 v_\eta \\ d_1 u u_\eta + d_2(v u_\eta + u v_\eta) + d_3 v v_\eta + d_4 T_\eta \end{pmatrix}, \tag{131}$$

where $\mathcal{U}$ and $\mathcal{V}$ denote the contravariant velocities

$$\mathcal{U} = \xi_x u + \xi_y v + \xi_t, \tag{132}$$

$$\mathcal{V} = \eta_x u + \eta_y v + \eta_t. \tag{133}$$

and b_i, c_i, and d_i represent the viscous coefficients [39]. Closure for the equations is enforced by Sutherland's viscosity formula, a constant Prandtl number, and the perfect-gas law.

The implicit implementation is applied to the strong conservation form of the Navier-Stokes equations. In delta form, with first-order Euler time differencing, the scheme is written as [14]:

$$\left\{I + \Delta t\left(\frac{\partial A^n}{\partial \xi} - \frac{\partial^2 M^n}{\partial \xi^2}\right)\right\}\left\{I + \Delta t\left(\frac{\partial B^n}{\partial \eta} - \frac{\partial^2 N^n}{\partial \eta^2}\right)\right\}\Delta \hat{U}^n =$$
$$-\Delta t\left\{\frac{\partial}{\partial \xi}(E_1 - V_1 - V_2)^n + \frac{\partial}{\partial \eta}(E_2 - W_1 - W_2)^n\right\}. \tag{134}$$

The scheme provides the correction vector, $\Delta\hat{U}$, to the current solution, $\hat{U}^n$

$$\hat{U}^{n+1} = \hat{U}^n + \Delta\hat{U}, \tag{135}$$

where n represents the temporal index such that $t = (n-1)\Delta t$ and A, B, M, and N represent the Jacobian matrices [39].

$$A = \frac{\partial E_1}{\partial \hat{U}}, \qquad B = \frac{\partial E_2}{\partial \hat{U}}, \tag{136}$$
$$M = \frac{\partial V_1}{\partial \hat{U}_\xi}, \qquad N = \frac{\partial W_2}{\partial \hat{U}_\eta}. \tag{137}$$

To maintain numerical stability and provide smooth solutions, explicit fourth-order damping is added to the right-hand side of Eq. (134)

$$D_\xi = -f_e \Delta t J^{-1}_{i,j} \delta^4_\xi U^n_{i,j}, \tag{138}$$

and implicit fourth-order damping is applied to the left side of Eq. (107)

$$D_\eta = -f_i \Delta t J^{-1}_{i,j} \delta^4_\eta U^n_{i,j}, \tag{139}$$

where δ is a second-order accurate, central-difference operator. The recommended values of the damping coefficients are [45]

$$f_e = \mathcal{O}(0.01), \quad f_i = 2f_e, \tag{140}$$

The values employed for this application are

$$f_e = 0.02, \quad f_i = 0.04. \tag{141}$$

V. Results and Conclusions: Part II

5.1 Overview

The focus of Chapter 5 is delineated into two major areas. The first area of exploration is the numerical prediction of flutter onset in the turbulent regime. As indicated in Part I (cf. Figure 1), there is a fundamental difference between the laminar and turbulent regimes, and this is reflected in the numerical results. The onset of flutter in the laminar, low-speed regime occurs at a significantly lower Reynolds number than the experimental results indicate [11, 15]. The original rationale for incorporating a turbulence model was to address this issue. The incompressible code is well validated in the low-speed, laminar regime (see Appendix A) for the case of the circular cylinder. However, the experimental efforts for the airfoil case have been exclusively concentrated in the higher Reynolds number range ($Re > 5 \times 10^5$) [11, 15, 12]. Therefore, the Baldwin-Lomax turbulence model is incorporated to capture the experimental data. Previous computational efforts in this regime include the work of Strganac, Mook and Mitchum [21], who numerically investigated subsonic flutter for a finite wing using a potential flow model. As previously discussed, Guruswamy [16] completed a similar effort using the full Navier-Stokes equations. Robinson et al. [20] have applied the Euler equations to predict the aeroelastic behavior of a wing with a deforming mesh.

The second area examined in Chapter 5 is the correlation between the numerically predicted aerodynamic transfer function and that obtained by Theodorsen's potential flow development. The effort is undertaken with the goal of establishing a basis for the numerical prediction of flutter onset. This is accomplished by comparing the theoretical lift coefficient predicted by Theodorsen's function to the numerically predicted lift coefficient. A NACA 0012 airfoil is oscillated with a prescribed frequency and amplitude to generate the unsteady lift coefficient. The modified incompressible code and the compressible code of Visbal are applied in this capacity.

Chaing and Fleeter [46] have undertaken a similar computational effort, computing the unsteady pressure distribution over an airfoil and comparing the results to those generated by Theodorsen's method. This was accomplished by applying a locally analytical method to the solution of the potential flow equations.

5.2 Flutter Onset: Comparison with Theory and Experiment

In this section results are presented in which the numerically predicted flutter onset velocity and those established by experiment and predicted by theory are compared. The numerical results are obtained using Grid 1, with a NACA 0015 profile substituted, as per the experiments of Yang and Zhao [11]. The incompressible code used in Part I is used along with the modified Baldwin-Lomax turbulence model. To allow operation of the code at the higher Reynolds number range, η-upwinding of identical form to the ξ-upwinding described in Part I is applied. The theoretical and additional experimental results are due to Theodorsen [15].

The numerical procedure employed is similar to the method described in Part I for the laminar case. A steady solution is obtained at relatively low Reynolds number ($Re \cong 2 \times 10^5$). The Reynolds number is then incremented and a new solution is obtained. The increase in Reynolds number introduces perturbations into the numerical flowfield, which are either damped or amplified to an unsteady solution. The Reynolds number increase was on the order of 5×10^4, however, smaller increments ($\sim 10^4$) were applied when the aerodynamic damping was reduced, i.e., as the critical point was approached.

The results are shown in Figure 26. The general trend of the numerical data is correct. However, the results are seen to be a function of the natural frequencies, ω_α and ω_h, rather than the ratio. This is in contrast to the theoretically predicted result [15]. The reason for this effect is the subcritical nature of the bifurcation. At lower values of ω_α and ω_h, a more dynamic augmented system is provided; perturbations are amplified more readily in this case. The presence of perturbations of increased magnitude then allow the possiblity of approaching a limit-cycle attractor rather than an equilibrium attractor. As a further consideration, consider a pitch-axis case where the value of ω_α is fixed, but $K_\alpha, I_\alpha \ll 1$. In this case it is obvious that the airfoil will be extremely responsive to perturbation. Additionally, Yang and Zhao [11] have observed a plunge-dominated, unsteady mode that could only be excited by providing an initial displacement in plunge. This result represents a differential response to perturbation level and thus offers experimental evidence of subcritical bifurcation. The results shown in Figure 26 are explained on this basis, i.e., subcritical bifiurcation and a consequent differential response to perturbation level. For instance, as ω_α is decreased (for a fixed airfoil mass and momemt of inertia), the torsional spring constant K_α is reduced. The weaker torsional spring allows a more dynamic response to aerodynamic perturbation, i.e., the aerodymamic perturbations introduced by the *Re*-continuation method explained above.

There are additional sources of error in the numerical computations which should be addressed. Firstly, the Baldwin-Lomax turbulence model has been criticized in unsteady flow applications [14, 47], and in the ability to predict self-induced oscillations [16]. Secondly, compressibility effects remain unresolved and are likely a factor in this regime. Thirdly, when employing the turbulence model at higher Reynolds numbers, timestep requirements became too restrictive, and therefore, examining results with a finer grid was computationally prohibitive. And lastly, in the course of subsequent computations, it became apparent that the concurrent application of η- and ξ-upwinding, when combined with the non-conservative form of the equations, impacted the phase response of the aerodynamic output. Nonetheless, the results do indicate clearly the demarcation between these results and those presented in Part I, and the role of turbulence in this demarcation (See Figure 1).

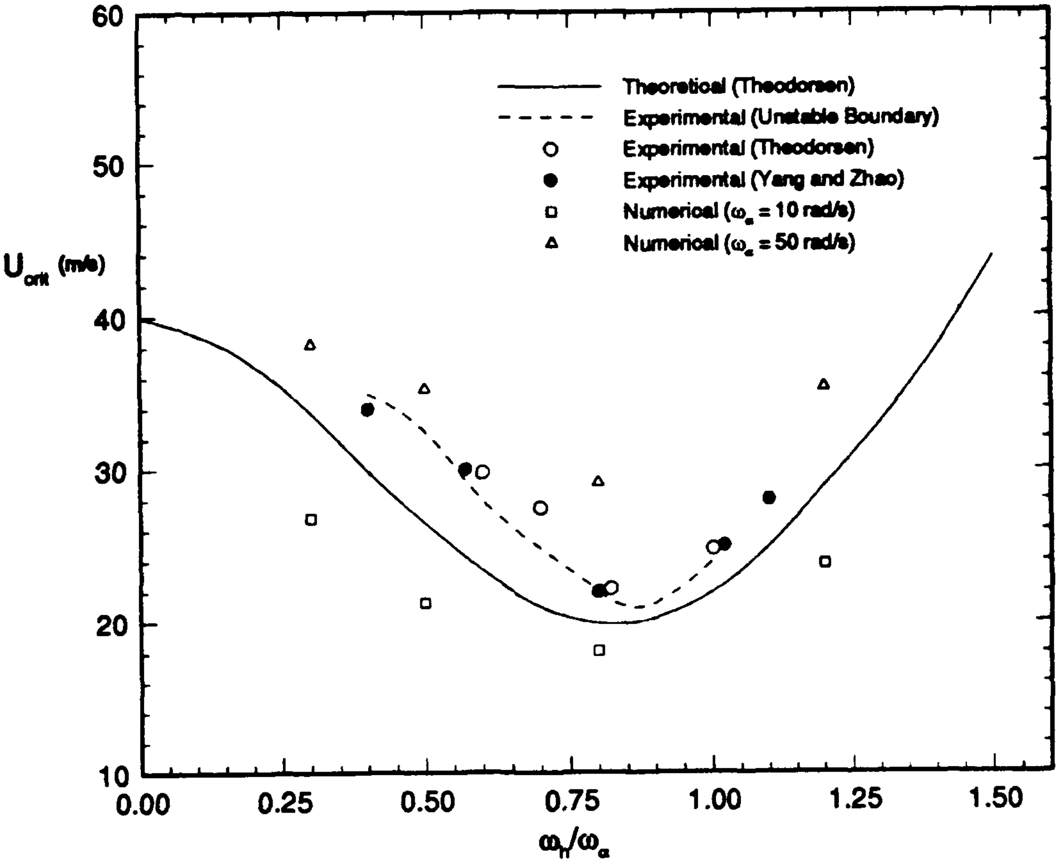

Figure 26. Flutter Onset Velocity as a Function of ω_h/ω_α.

5.3 Comparison with Inviscid Aerodynamic Transfer Function

In this section, a basis is established for the application of the considered numerical algorithms to the prediction of flutter onset for an airfoil. The theoretical development of the prediction of flutter was pioneered by Theodorsen [15], using potential flow theory in conjuntion with an assumed distribution of circulation in the wake and the application of the Kutta condition at the trailing edge. In the theoretical approach, the derivation of Theodorsen's function models the inviscid aerodynamic transfer function. It provides the aerodynamic response to an input of prescribed amplitude and frequency.

The general intent of the numerical efforts in this regard is to compare the aerodynamic transfer function described by Theodorsen to that predicted numerically. This is done for two codes: the modified form of the incompressible code and the compressible code of Visbal [27], modeling the full Navier-Stokes equations (see Chapter 4). The approach is to apply a forcing function, angle of attack, $\alpha(t)$, of known amplitude and frequency and assess whether the numerical results correspond to the theoretical results of Theodorsen, across a broad range of frequencies. Since Theodorsen's approach is derived assuming small perturbations about an equilibrium state, the amplitude of the angular oscillation is fixed at 0.01 radians. The airfoil is oscillated at reduced frequencies, k, ranging from 0.05 to 6, with the Reynolds number varied between $Re = 100$ and $Re = 3 \times 10^6$. All cases are initiated from an equilibrium solution at $\alpha = 0$ for a given Reynolds number.

Results are compared in Figures 27-32 for the compressible code and Figures 33-36 for the incompressible code. The lift coefficient predicted by Theodorsen's function is denoted C_k, (cf. Eq. (120)) and is represented by long-dashed lines in Figures 27-36. C_l refers to the numerically computed lift coefficient, and is represented by solid lines. The angle of attack, α, is indicated by short-dashed lines.

The agreement with Theodorsen's function is seen to be a function of the reduced frequency k, but in general the results are good. An exact correspondence was not anticipated; differences in the approaches remain, primarily consisting of:

- Reynolds number effects
- airfoil thickness effects
- validity of the assumed distribution of circulation
- grid-related effects
- artificial dissipation effects
- compressibility effects

The theoretical result is derived assuming an inviscid fluid, corresponding to an infinite Reynolds number. The numerical computations are constrained to finite Reynolds numbers, and therefore some differences due to Reynolds number effects may remain. This is particularly true for the incompressible code, since it is constrained to a lower Reynolds number range than the compressible code. The distribution of circulation assumed in the theoretical development (cf. Eq. (116)) in conjunction with the application of the Kutta condition (cf. Eq. (115)), allows a framework for incorporating viscous effects into the inviscid analysis. The manifestation of vorticity in the wake and the satisfaction of the Kutta condition for the viscous codes are accomplished by a completely different mechanism, i.e., the direct solution of the field equations with an associated set of boundary conditions. Grid-related effects are important because the moving grid establishes time-dependent numerical errors which must be damped. The ability to damp these errors is dependent upon the grid resolution. Errors of this type occur in addition to the discretization or truncation errors associated with numerical computations performed on a fixed grid. Artificial dissipation can further influence the numerical results, for instance, it was mentioned earlier that concurrent application of ξ- and η-upwinding introduces phase errors into the numerical calculations. And lastly, for the case of the compressible code, compressibility effects are a factor. Of the above items, only Reynolds number effects are addressed in a systematic fashion.

The most meaningful trend is the convergence of the numerical results to those of theory as the Reynolds number increases, i.e., as an inviscid solution is approached. This trend is evident at every frequency considered, except for one case for the incompressible code, which will be addressed later. The results for the compressible code are discussed first. More runs were performed with this code because the required modifications were much simpler, and data was collected during the development of the modified incompressible code. All displayed results for the compressible code were performed using an O-grid with grid characteristics equivalent to Grid 1. The freestream Mach number was set at 0.2, with fourth-order explicit and implicit damping levels fixed at $f_e = 0.02$ and $f_i = 0.04$. No second-order damping was employed. Previous numerical studies [48, 49] indicate that the timestep required for an accurate temporal resolution may be less than that required for numerical stability. To ensure accuracy, the timestep, Δt, is adjusted to enforce a minimum of 1000 timesteps per period of oscillation, as recommended by Stanek and Visbal [49].

The first result shown is for $k = 0.05$, see Figure 27. As the Reynolds number is increased from 100 to 3×10^6, a clear convergence to theory is apparent. The trend occurs for each increment in Reynolds number; the amplitude appears almost exact for the $Re = 3 \times 10^6$ case. A slight phase error between C_l and C_k is not rectified by the increased Reynolds number. The $k = 0.2$ case shows an identical trend; the amplitude is nearly exact, but the phase lag is slightly exacerbated at this frequency. At $k = 1$, an interesting transition appears, as the error appears to express itself as an amplitude rather than a phase error. The amplitude shows a slight error while the phase lag is negligible. An increase to $k = 2$ appears to resolve both the phase and amplitude errors, as the solution at $Re = 3 \times 10^6$ displays almost no amplitude or phase error. The results for $k = 4$ mimics the results for $k = 0.05$ in that the amplitude error now appears negligible but the phase error is reintroduced. Finally, the results for $k = 6$ appear to follow the same trend as the $k = 0.2$ case, i.e., the phase lag is exacerbated compared with the prior result. The results indicate a cyclic trend in the phase and amplitude errors. The graphical presentation of this trend is shown in Figure 38, which summarizes the phase and amplitude errors as a function of k, where the phase error is indicated as a percentage of the period and the amplitude error is based on peak values. It is expected that beyond $k = 6$, numerical errors would begin to predominate, and that poor numerical results would eventually ensue. See the stability analysis presented in Appendix B for an indication of this behavior.

The results for the incompressible code are displayed in Figures 33-36. Several difficulties arose in the application of the incompressible code. The primary difficulty, already mentioned, is the problem associated with concurrent application of ξ- and η-upwinding in conjunction with the non-conservative form of the equations. It became apparent that the application of η-upwinding produced unwanted phase errors in the solution. However, η-upwinding is required to approach the higher Reynolds numbers. Therefore, η-upwinding was not applied to assess the correspondence with Theodorsen's function, This, in turn, imposed a restriction on the Reynolds number range, and a more stringent timestep requirement. For this reason, the maximum Reynolds number considered in this case was 2000. However, this proved satisfactory to demonstrate the trends previously observed with the compressible code. It should be noted that for $Re \geq 4000$, the numerical results were degraded, as a function of k, for the reasons expressed above.

Figure 33 shows the progression in Reynolds number for $k = 0.05$. A clear convergence to the theoretical result is indicated. However, at $Re = 2000$ there is still a small amplitude error. Figure 34 displays the results for the $k = 0.2$ case. Again, a clear convergence is noted, with a very close agreement in both phase and amplitude for $Re = 2000$. The results for $k = 2$ (Figure 35) also show close agreement at $Re = 2000$. The limitations of the incompressible code becomes apparent at higher frequencies, as the results for $k = 4$, shown in Figure 36, indicate. The results appear to be converging as Re increases from 100 to 500, however, when

Re is increased to 1000, the solution is degraded rather than improved. This result is attributed to the lack of dissipation in the η direction. This argument is supported by the apparent convergence for the lower Reynolds numbers, where the natural dissipation is presumably sufficient. However, as the Reynolds number continues to increase, the natural dissipation becomes insufficient. Additionally, this problem predominates only at higher frequencies, when the oscillations in velocity normal to the surface assume a larger magnitude, exacerbating the difficulties due to the lack of η-upwinding. The trend continues to develop as the solution at $Re = 2000$ exhibits increased amplitude, with slight variation in peak amplitudes noted.

The convergence to the theoretical result is quantified by defining a norm

$$||\Delta C_l|| \equiv \sqrt{\sum (C_l - C_k)^2 / N}, \tag{142}$$

where N is the number of discrete points over which the summation is applied. The summation is applied over I periods, where I is an integer. The beginning of a period was taken to be when $C_k = 0$, which generally corresponded to the least error. The variation of $||\Delta C_l||$ with Re for $k = 0.2$ is displayed in Figure 39 for the incompressible code.

A parametric investigation is presented in Table 3. The results were computed using the compressible code, at $k = 1$. Case 1 represents the baseline result presented in Figure 29d. In cases 2 through 4 the artificial dissipation levels, f_e and f_i, were reduced by a factor of two, successively. In cases 2 and 3 there is a slight increase in $||\Delta C_l||$, indicating that the initial dissipation levels were required to provide sufficient damping for the case of the oscillating airfoil. The dissipation levels employed in case 4 were insufficient and resulted in divergence. Case 5 explores the influence of the turbulence model. With the turbulence model active, there is no discernable change in the computed results, and $||\Delta C_l||$ remains invariant to five significant figures. Cases 6 through 11 explore the impact of compressibility by incrementing the Mach number from 0.2 to 0.5. Initially, (case 6) there is a slight improvement compared to the theoretical result and $||\Delta C_l||$ decreases slightly. However, as Mach number continues to increase, a pronounced degredation in the results ensues, and $||\Delta C_l||$ increases by an order of magnitude (case 11). Cases 12 through 15 examined the trend for increasing Reynolds number (beyond 3×10^6). The Reynolds number was increased in increments of 3×10^6 up to 15×10^6. The results indicate a continued, albeit gradual, convergence to the theoretical result. Finally, in cases 16 through 19, a limited grid refinement effort was undertaken. A slight degredation in accuracy was noted for the finer grids, when compared with the coarse grid, as $||\Delta C_l||$ increased slightly (cases 17 and 19). This may be due, in part, to a better resolution of the wake and boundary layer, where the resolved viscous effects may have an influence. It should be noted that for grids finer than 60x25, the turbulence model must be employed to prevent secondary oscillations from developing. The secondary oscillations further increase the $||\Delta C_l||$ norm, as indicated in cases 16 and 18. The development of the secondary oscillations, due principally to the reduced levels of effective dissipation when the turbulence model is not applied, is shown in Figure 37.

Also displayed in Figures 40-43, at $\tau = 1$, 2, and 3 are the vorticity contours in the wake. The solutions were obtained with the incompressible code using Grid 2 at $Re = 500$ and $k = 2$, starting from an equilibrium solution at $\tau = 0$ and $\alpha = 0$, with a peak angular amplitude of approximately 2 degrees. Positive vorticity is generated on the lower surface, while negative vorticity predominates near the upper surface. The effect of the oscillations on the wake development is pronounced, as the shed vorticity indicates. The aforementioned difficulty concerning η-upwinding is evident in the wake. That is, with no η-upwinding applied, there is no effective damping in the η direction except for that provided by natural dissipation. A close examination of the contours in the wake reveals negligible oscillations occuring along the contours in the ξ direction. However, increased numerical oscillations are noted when the

Case No.	O-Grid	*Re*	*Mach*	f_e	f_i	turb	$\Vert \Delta C_l \Vert$
1	60x25	3×10^6	0.20	0.0200	0.0400	off	6.7613×10^{-3}
2	60x25	3×10^6	0.20	0.0100	0.0200	off	6.9609×10^{-3}
3	60x25	3×10^6	0.20	0.0050	0.0100	off	7.3971×10^{-3}
4	60x25	3×10^6	0.20	0.0025	0.0050	off	diverged
5	60x25	3×10^6	0.20	0.0200	0.0400	on	6.7613×10^{-3}
6	60x25	3×10^6	0.25	0.0200	0.0400	off	6.5250×10^{-3}
7	60x25	3×10^6	0.30	0.0200	0.0400	off	6.7287×10^{-3}
8	60x25	3×10^6	0.35	0.0200	0.0400	off	7.8803×10^{-3}
9	60x25	3×10^6	0.40	0.0200	0.0400	off	3.3959×10^{-2}
10	60x25	3×10^6	0.45	0.0200	0.0400	off	3.4943×10^{-2}
11	60x25	3×10^6	0.50	0.0200	0.0400	off	3.4351×10^{-2}
12	60x25	6×10^6	0.20	0.0200	0.0400	off	6.7163×10^{-3}
13	60x25	9×10^6	0.20	0.0200	0.0400	off	6.7011×10^{-3}
14	60x25	12×10^6	0.20	0.0200	0.0400	off	6.6935×10^{-3}
15	60x25	15×10^6	0.20	0.0200	0.0400	off	6.6889×10^{-3}
16	125x50	3×10^6	0.20	0.0200	0.0400	off	1.2043×10^{-2}
17	125x50	3×10^6	0.20	0.0200	0.0400	on	8.1662×10^{-3}
18	208x108	3×10^6	0.20	0.0200	0.0400	off	2.6902×10^{-2}
19	208x108	3×10^6	0.20	0.0200	0.0400	on	7.7829×10^{-3}

Table 3. Tabulated Parametric Results; Reduced Frequency, $k = 1$

contours are oriented in the η direction. The oscillations cannot be solely attributed to grid courseness in the wake region because, for the particular region in question, the grid spacing in the ξ direction is actually coarser than that in the η direction, particularly near the branch-cut (cf. Figure 5). A comparison with the O-Grid case is offered in Figure 43, using the compressible code at the same conditions. In general the development of vorticity near the trailing edge and the subsequent convection into the wake is less pronounced. There are two possible reasons for this. Primarily, the differences in topology are considerable at the trailing edge. The O-grid has a rounded trailing edge while the C-grid ends in a sharp point. The sharp trailing edge in the case of the C-grid appears to act as a vortex generator as the airfoil oscillates. Another significant difference is the application of the boundary conditions. The branch cut, for the case of the C-grid, extends from the trailing edge to the outer computational domain. In contrast, the branch cut for the O-grid extends from the leading edge to the computational boundary.

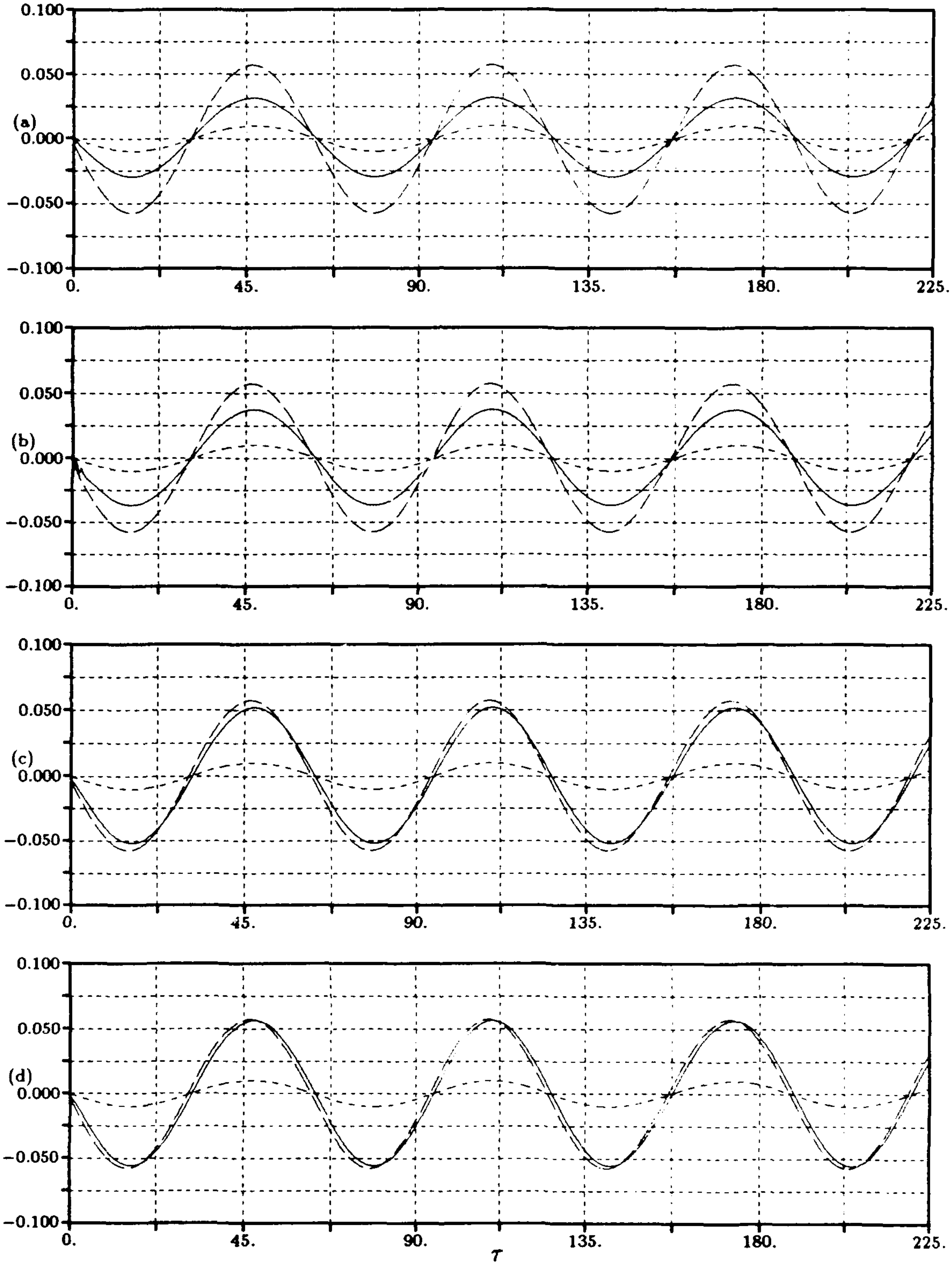

Figure 27. Comparison of Calculated (solid line) and Theoretical (long-dashed line) Lift Coefficient, Compressible Code, α (short-dashed line), Reduced Frequency $k = 0.05$; (a) $Re = 100$, (b) $Re = 1000$, (c) $Re = 1.5 \times 10^5$, (d) $Re = 3.0 \times 10^6$

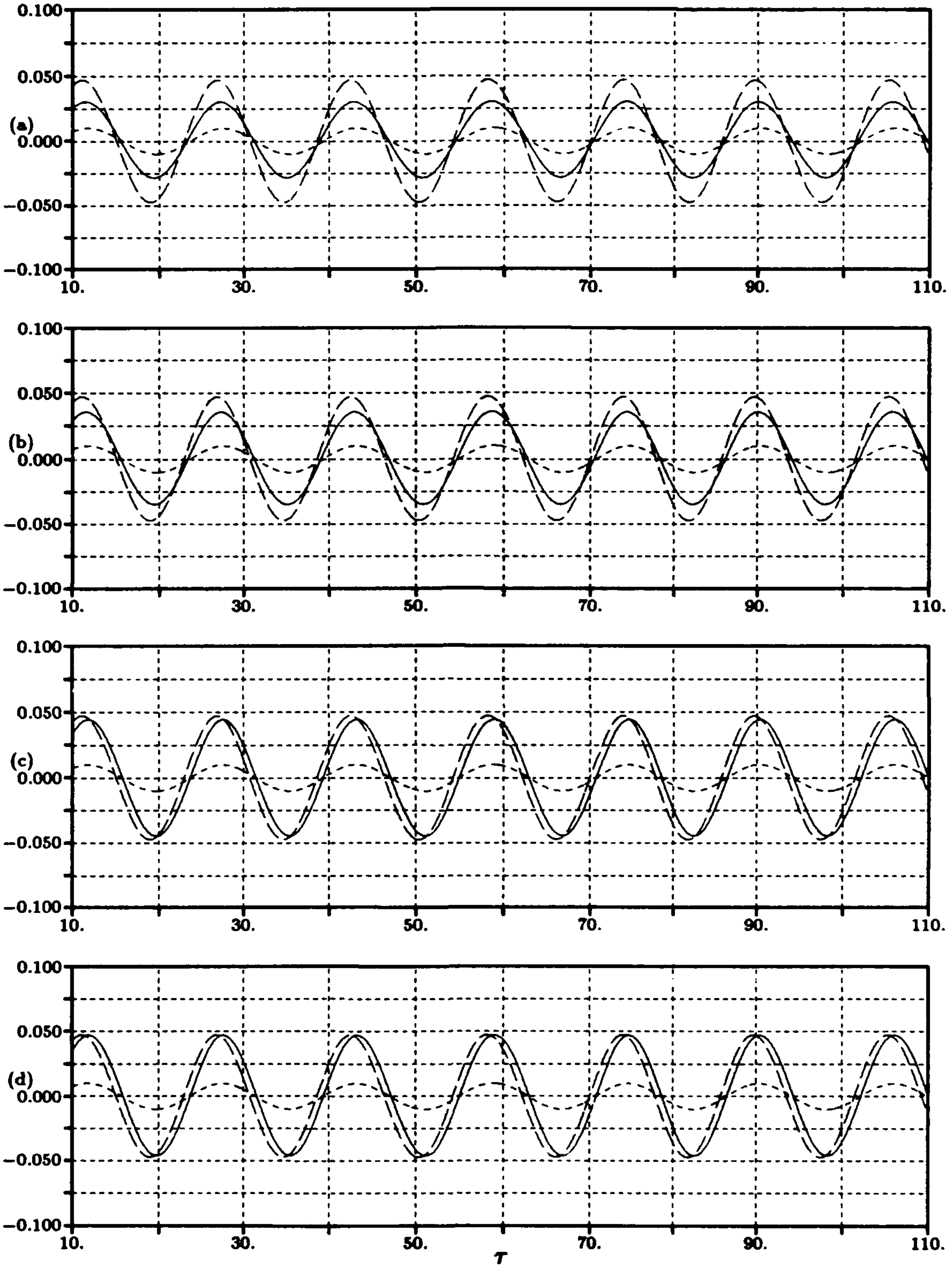

Figure 28. Comparison of Calculated (solid line) and Theoretical (long-dashed line) Lift Coefficient, Compressible Code, α (short-dashed line), Reduced Frequency $k = 0.2$; (a) $Re = 100$, (b) $Re = 1000$, (c) $Re = 1.5 \times 10^5$, (d) $Re = 3.0 \times 10^6$

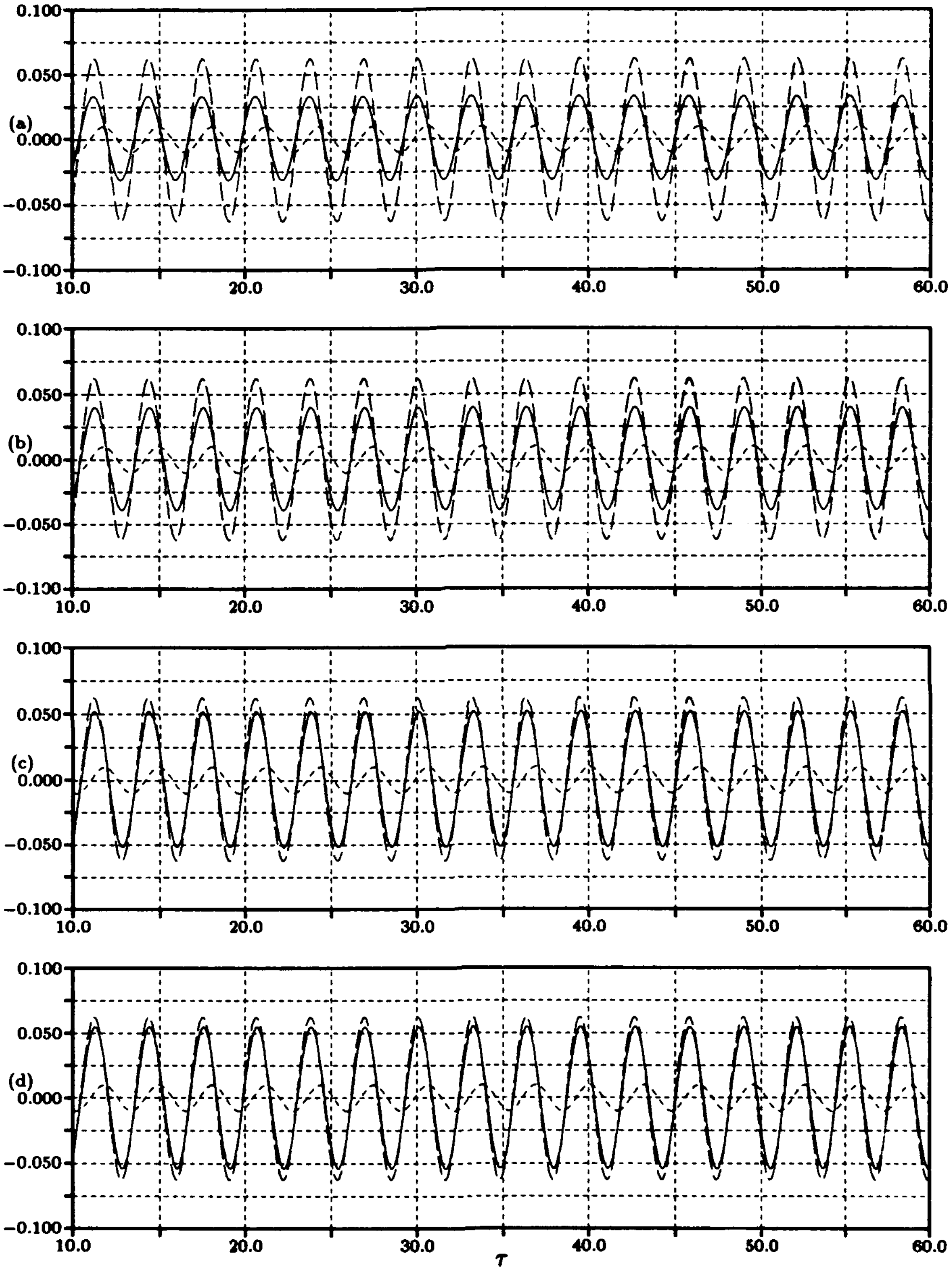

Figure 29. Comparison of Calculated (solid line) and Theoretical (long-dashed line) Lift Coefficient, Compressible Code, α (short-dashed line), Reduced Frequency $k = 1$; (a) $Re = 100$, (b) $Re = 1000$, (c) $Re = 1.5 \times 10^5$, (d) $Re = 3.0 \times 10^6$

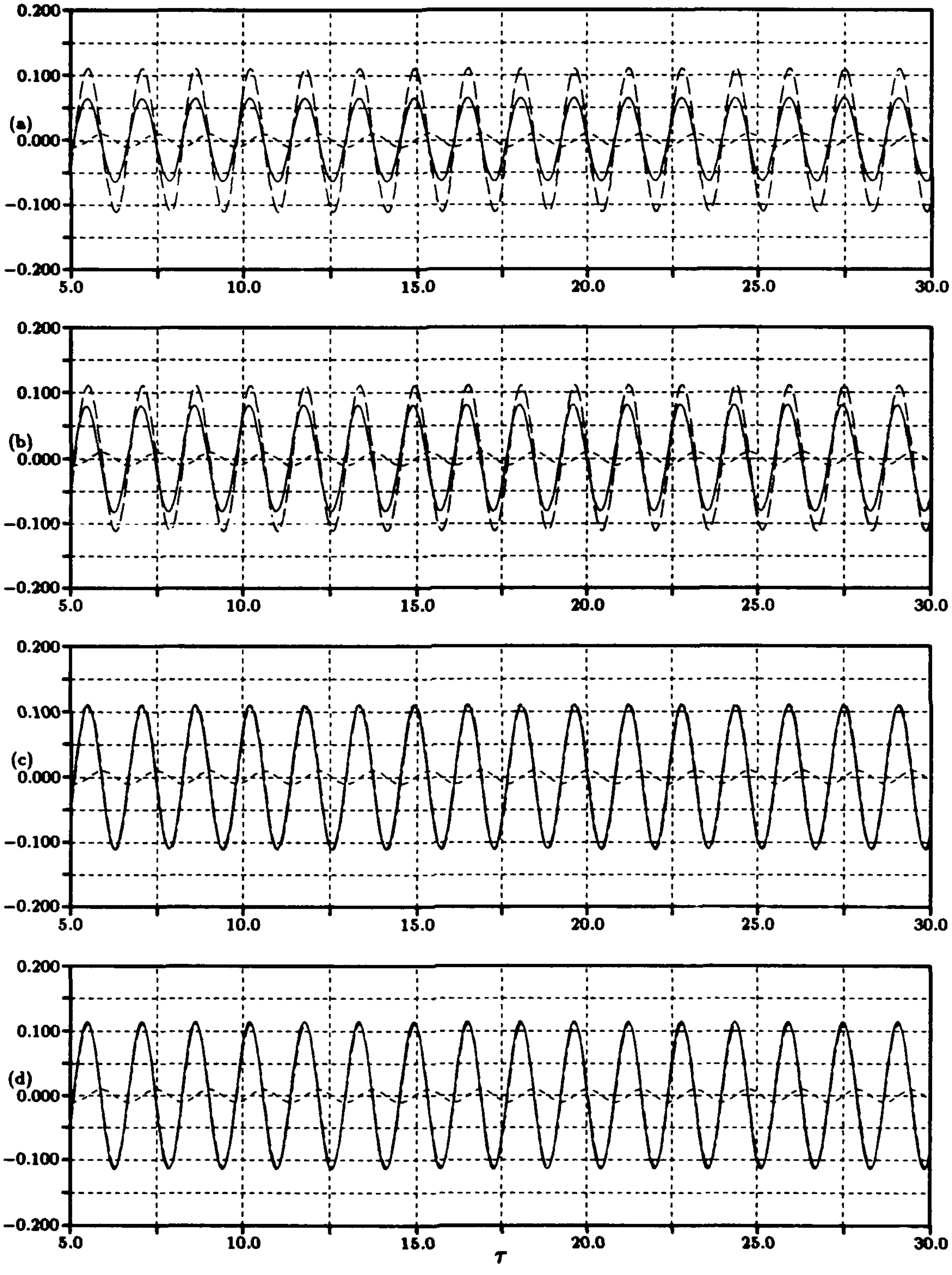

Figure 30. Comparison of Calculated (solid line) and Theoretical (long-dashed line) Lift Coefficient, Compressible Code, α (short-dashed line), Reduced Frequency $k = 2$; (a) $Re = 100$, (b) $Re = 1000$, (c) $Re = 1.5 \times 10^5$, (d) $Re = 3.0 \times 10^6$

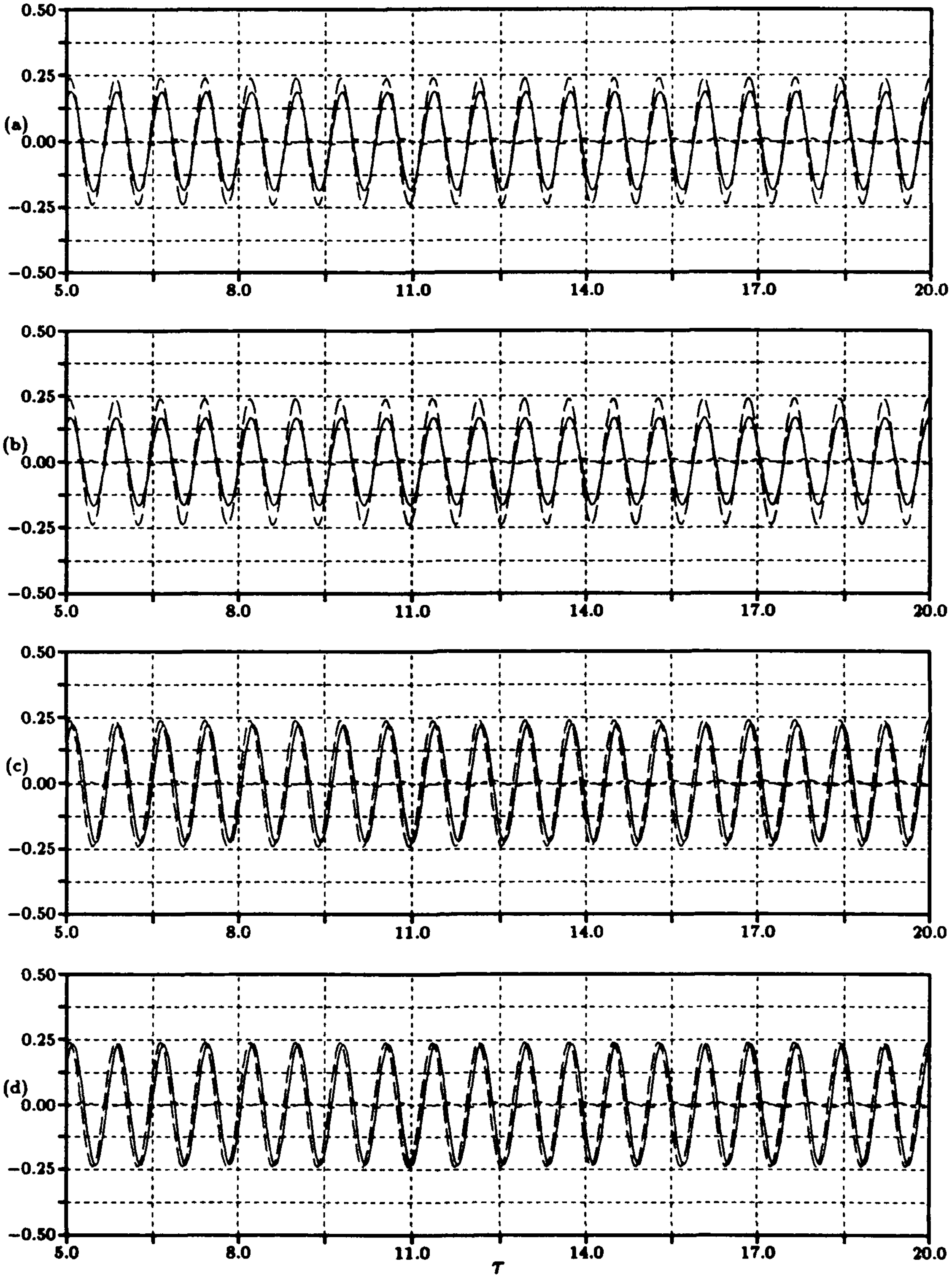

Figure 31. Comparison of Calculated (solid line) and Theoretical (long-dashed line) Lift Coefficient, Compressible Code, α (short-dashed line), Reduced Frequency $k = 4$; (a) $Re = 100$, (b) $Re = 1000$, (c) $Re = 1.5 \times 10^5$, (d) $Re = 3.0 \times 10^6$

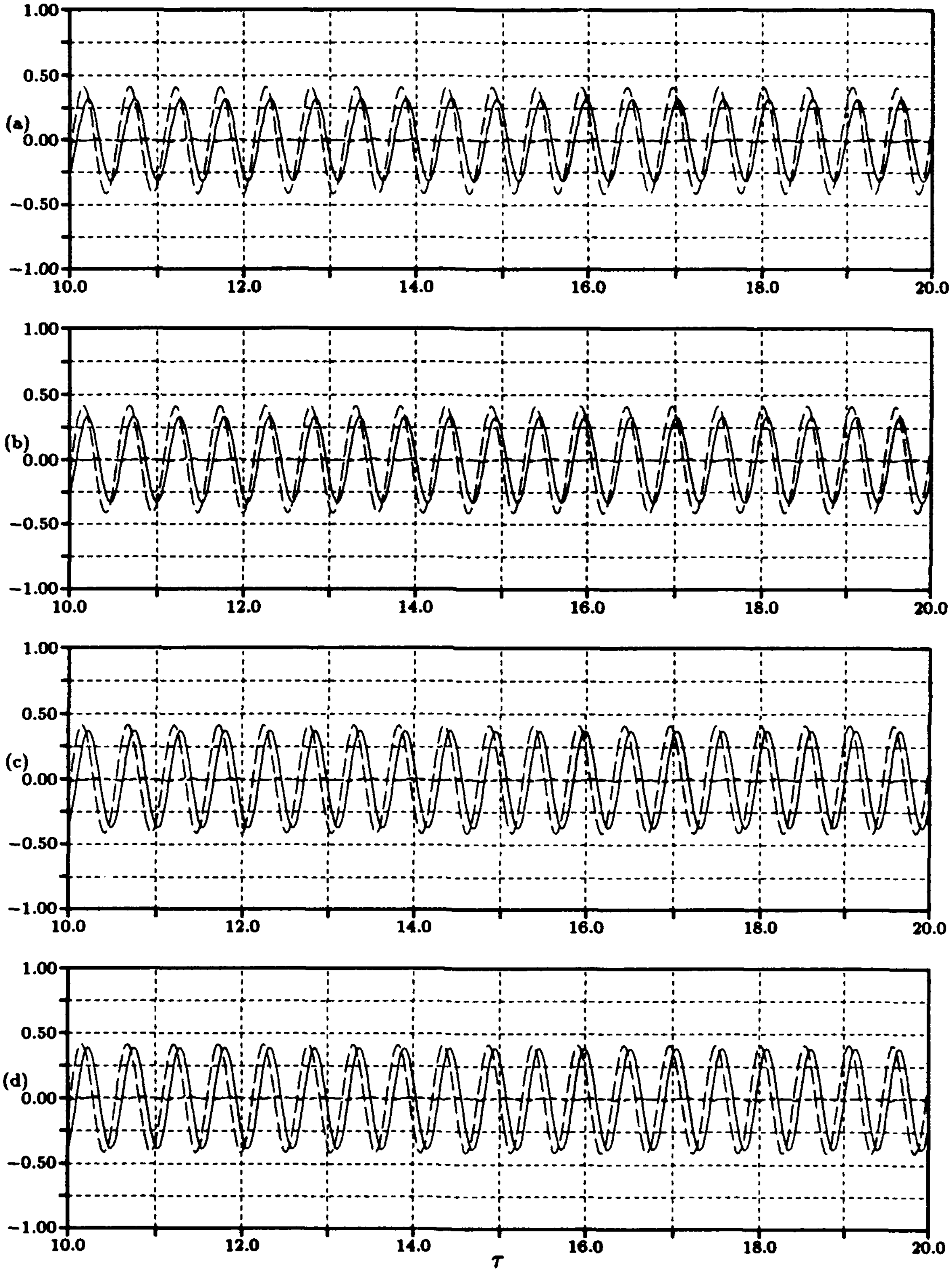

Figure 32. Comparison of Calculated (solid line) and Theoretical (long-dashed line) Lift Coefficient, Compressible Code, α (short-dashed line), Reduced Frequency $k = 6$; (a) $Re = 100$, (b) $Re = 1000$, (c) $Re = 1.5 \times 10^5$, (d) $Re = 3.0 \times 10^6$

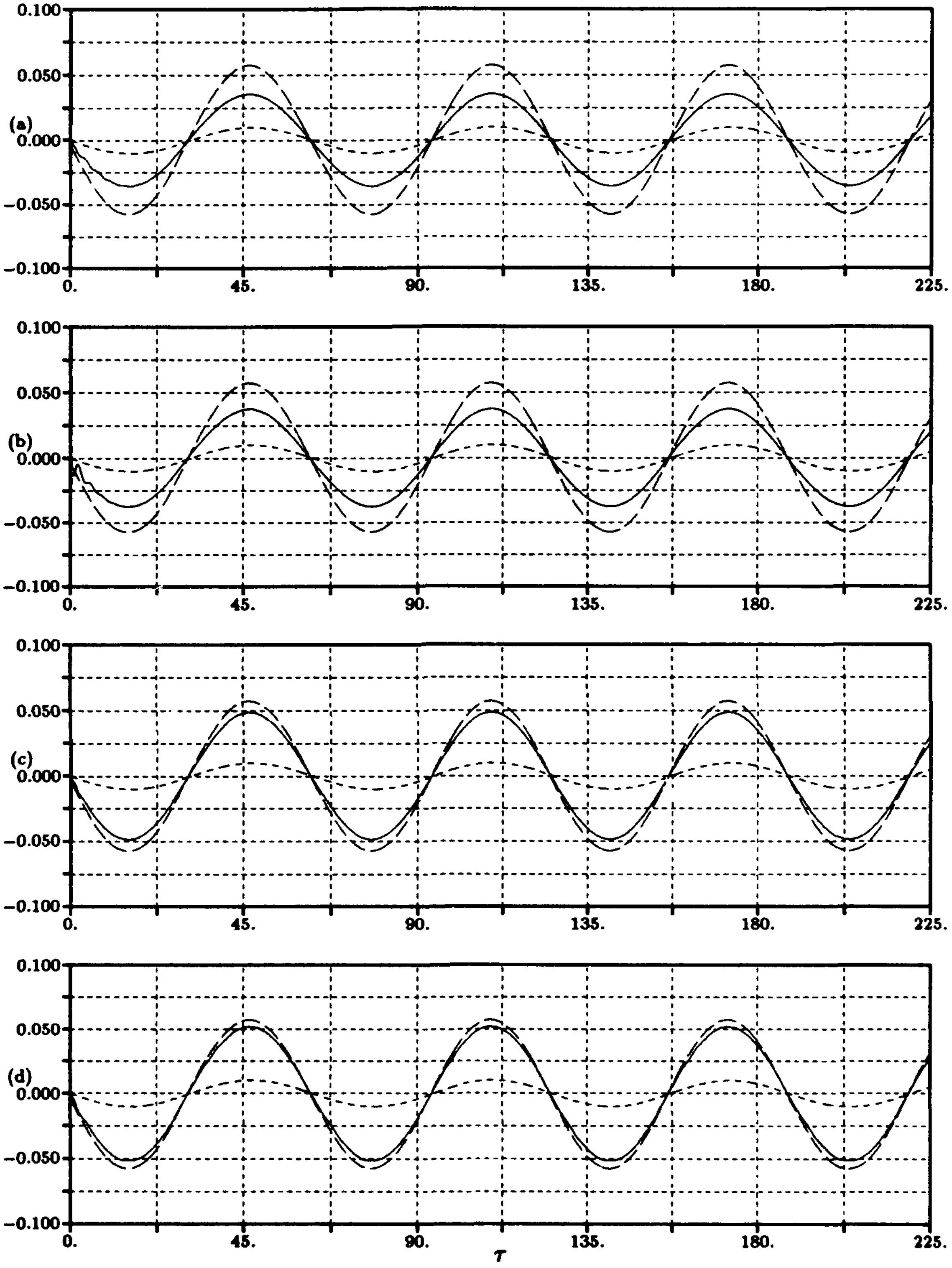

Figure 33. Comparison of Calculated (solid line) and Theoretical (long-dashed line) Lift Coefficient, Incompressible Code, α (short-dashed line), Reduced Frequency $k = 0.05$; (a) $Re = 100$, (b) $Re = 500$, (c) $Re = 1000$, (d) $Re = 2000$

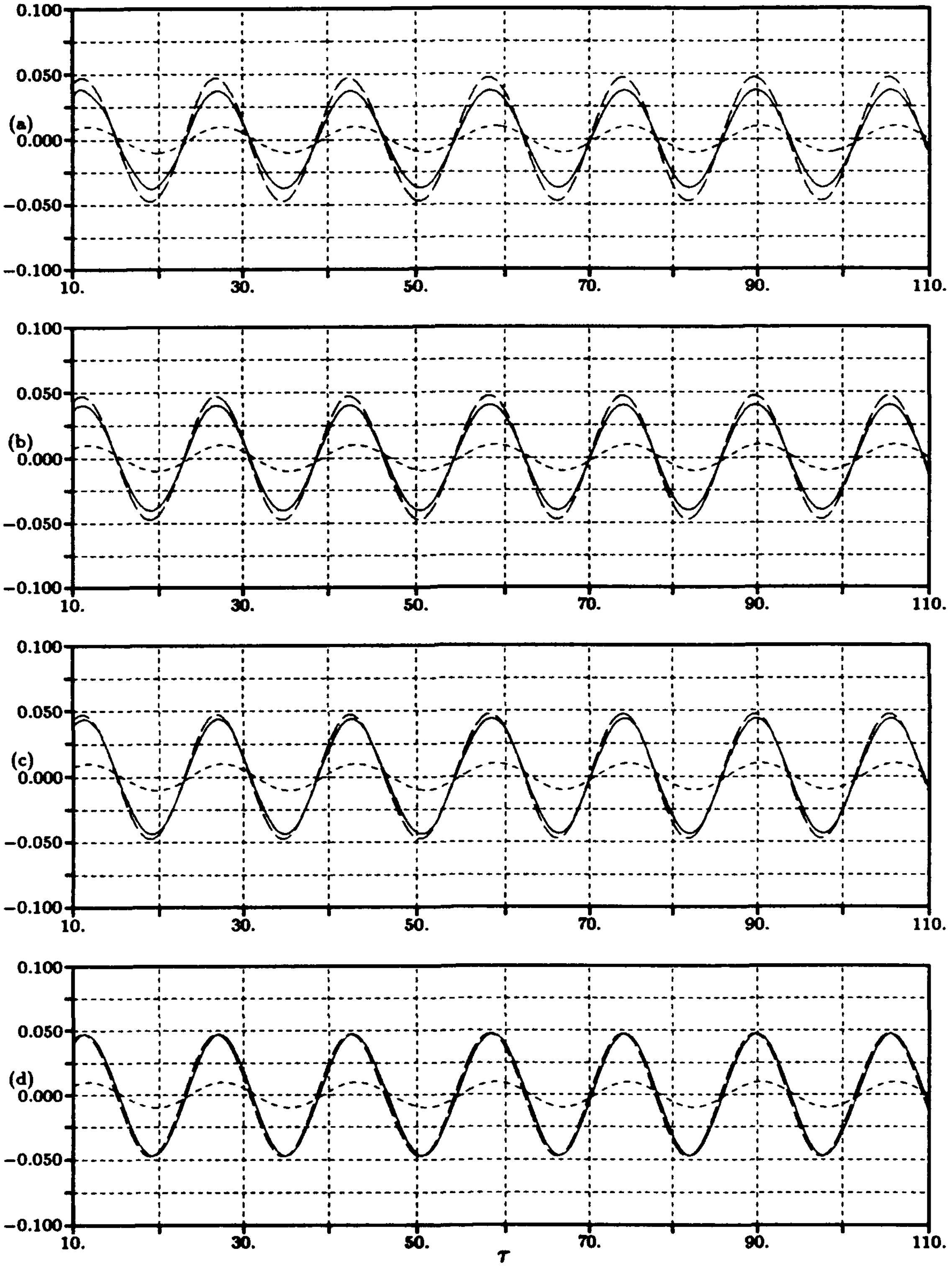

Figure 34. Comparison of Calculated (solid line) and Theoretical (long-dashed line) Lift Coefficient, Incompressible Code, α (short-dashed line), Reduced Frequency $k = 0.2$; (a) $Re = 100$, (b) $Re = 500$, (c) $Re = 1000$, (d) $Re = 2000$

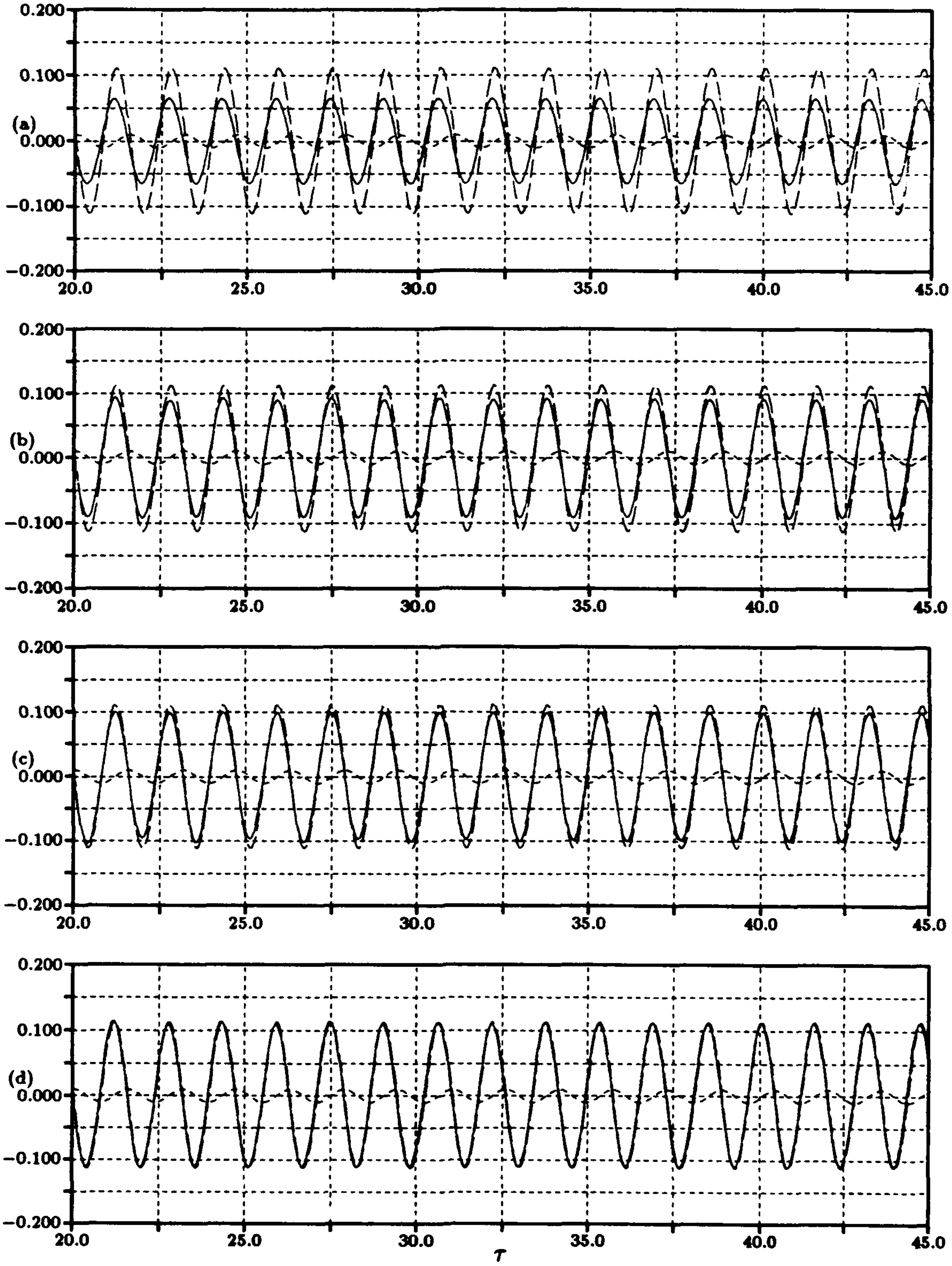

Figure 35. Comparison of Calculated (solid line) and Theoretical (long-dashed line) Lift Coefficient, Incompressible Code, α (short-dashed line), Reduced Frequency $k = 2$; (a) $Re = 100$, (b) $Re = 500$, (c) $Re = 1000$, (d) $Re = 2000$

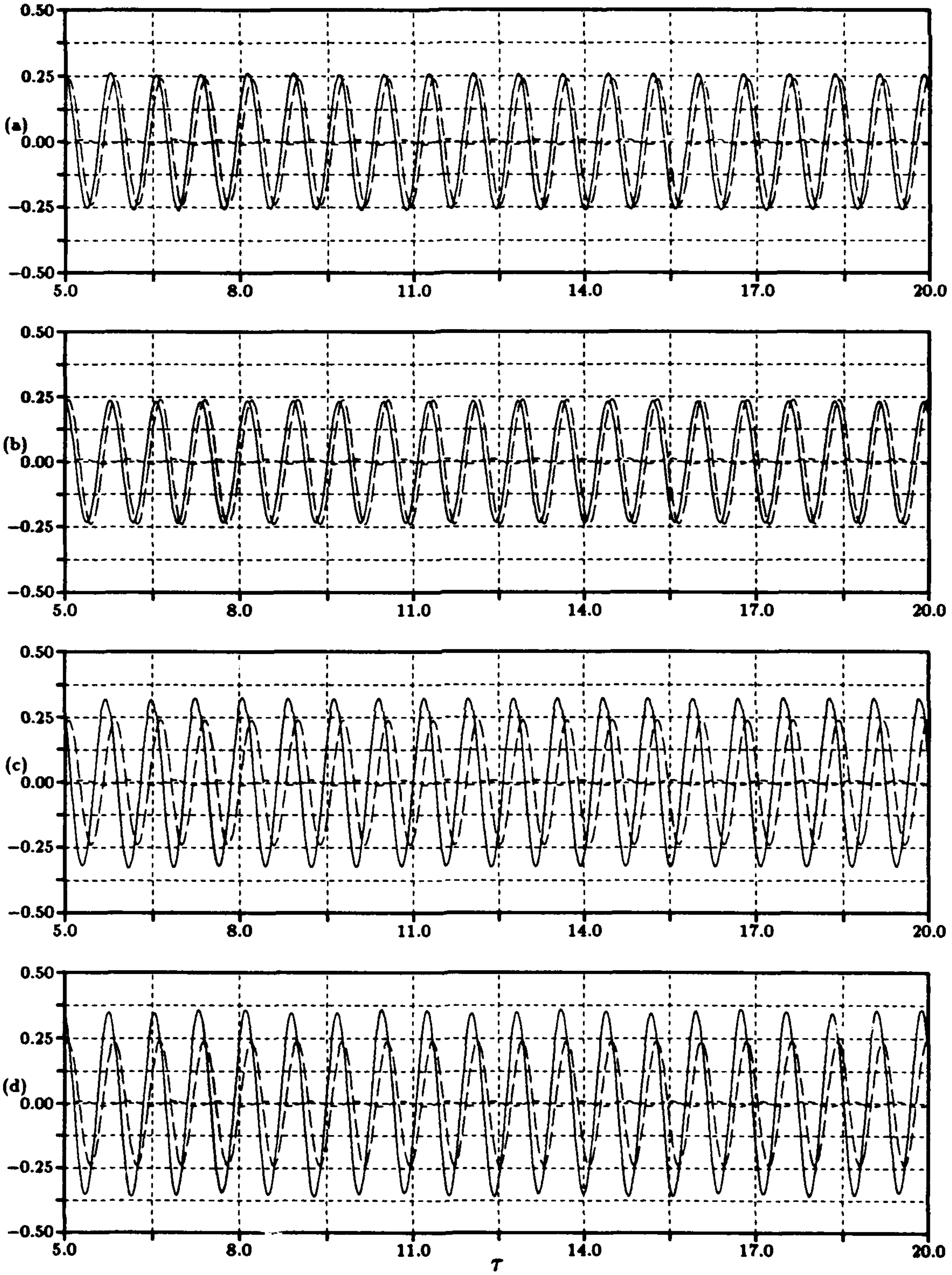

Figure 36. Comparison of Calculated (solid line) and Theoretical (long-dashed line) Lift Coefficient, Incompressible Code, α (short-dashed line), Reduced Frequency $k = 4$; (a) $Re = 100$, (b) $Re = 500$, (c) $Re = 1000$, (d) $Re = 2000$

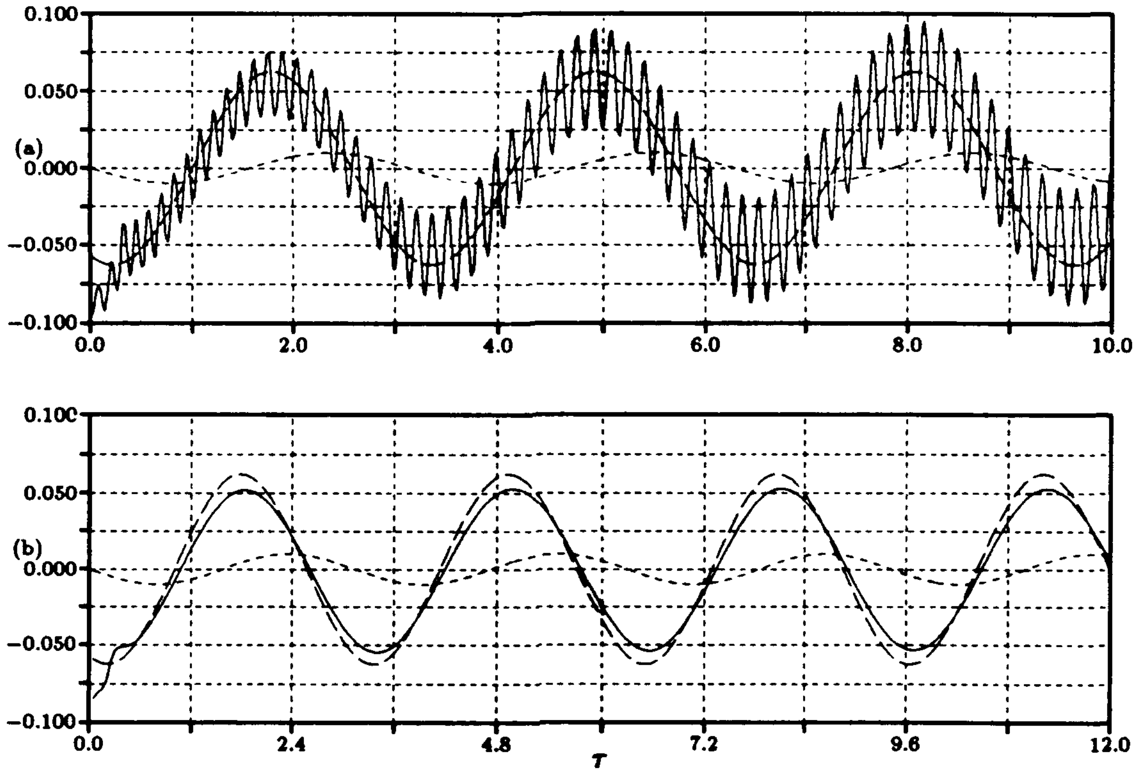

Figure 37. O-Grid 209x108: $k = 1$, $Re = 3 \times 10^6$, (a) Turbulence Model Off, (b) Turbulence Model On

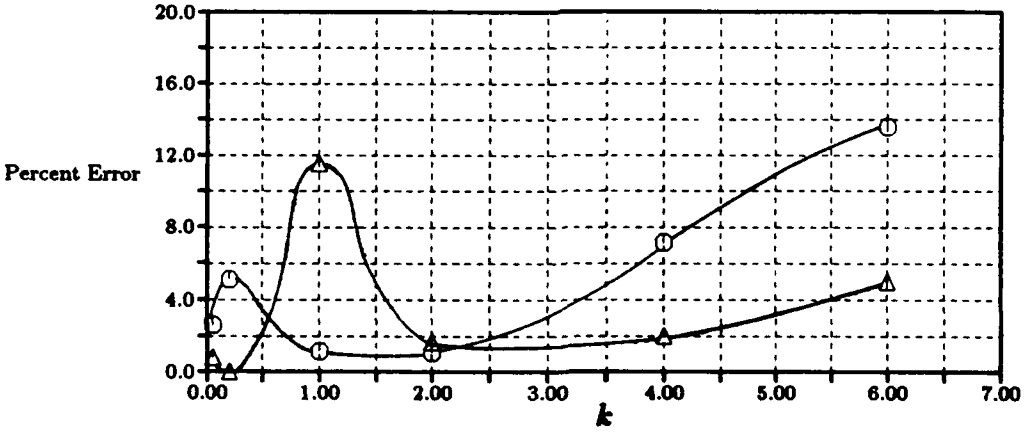

Figure 38. Phase and Amplitude Errors as a Function of Reduced Frequncy: Compressible Code; Phase Error (⊙) Amplitude Error (△)

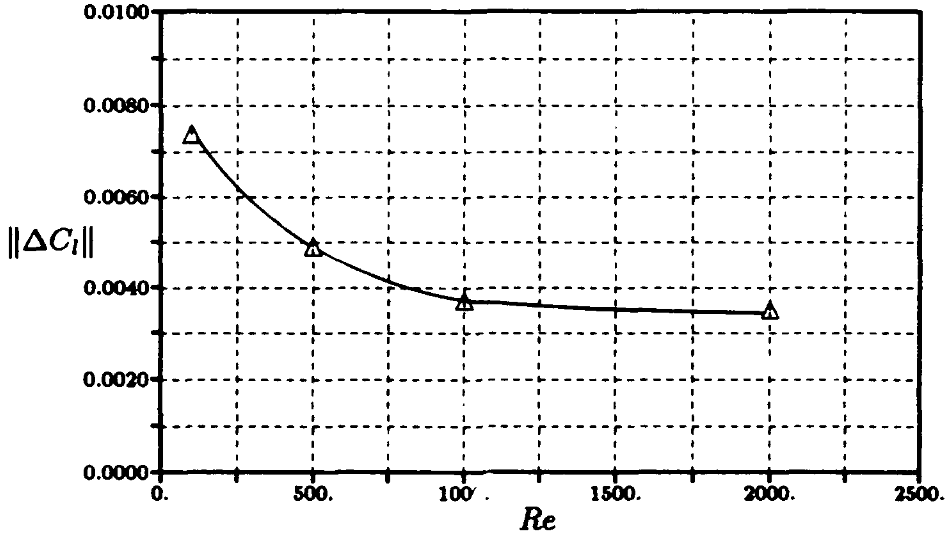

Figure 39. Error Norm as a Function of Reynolds Number: Incompressible Code ($k = 0.2$)

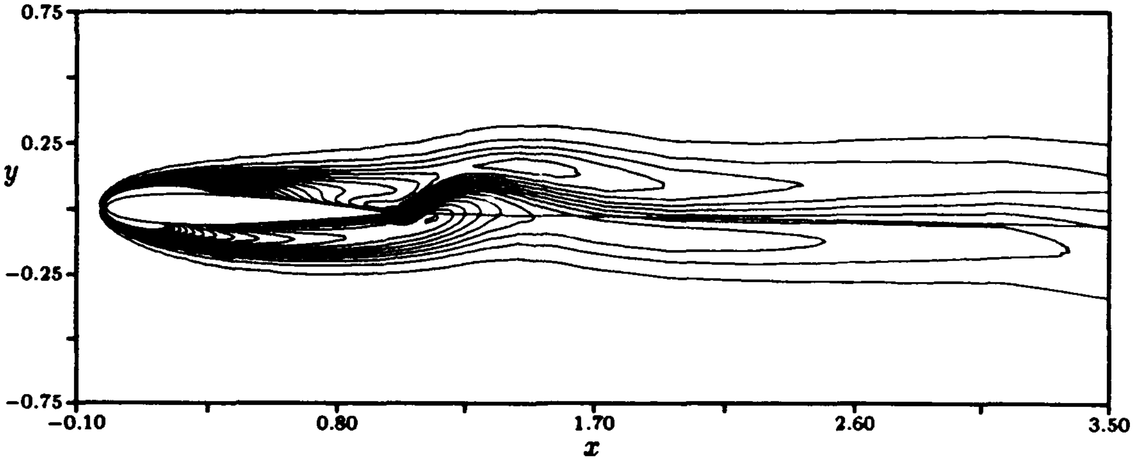

Figure 40. Vorticity Contours: Incompresible Code, Grid 2, Re = 500, k = 2, $\tau = 1.0$

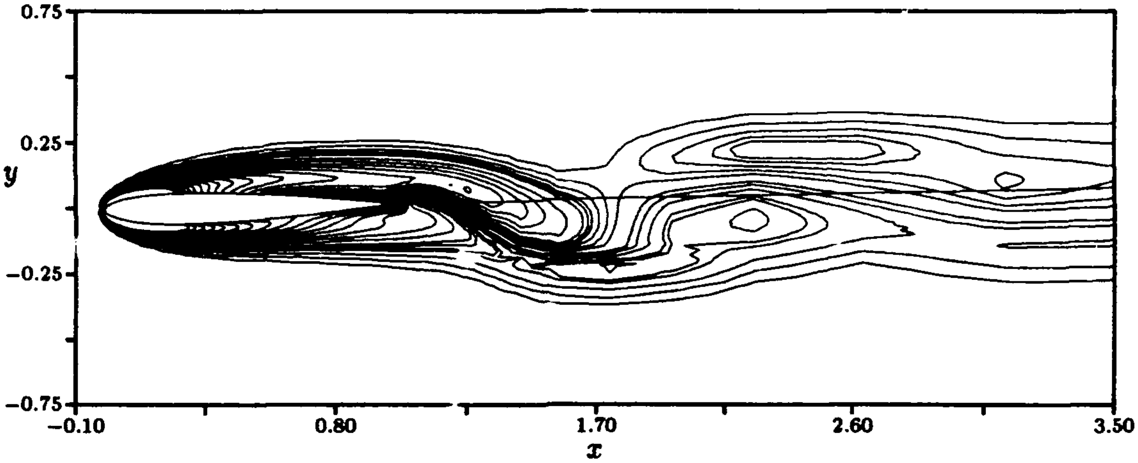

Figure 41. Vorticity Contours: Incompressible Code, Grid 2, *Re* = 500, *k* = 2, $\tau = 2.0$

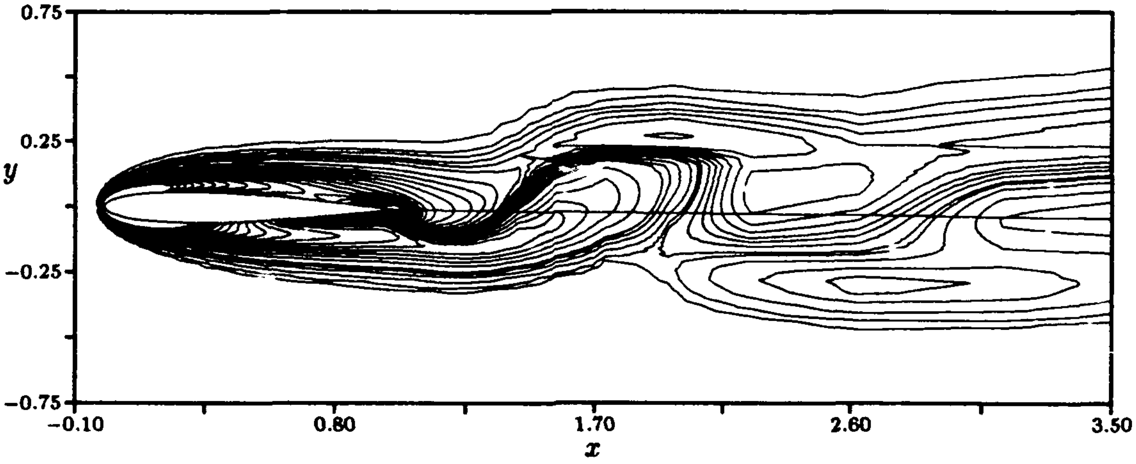

Figure 42. Vorticity Contours: Incompressible Code, Grid 2, *Re* = 500, *k* = 2, $\tau = 3.0$

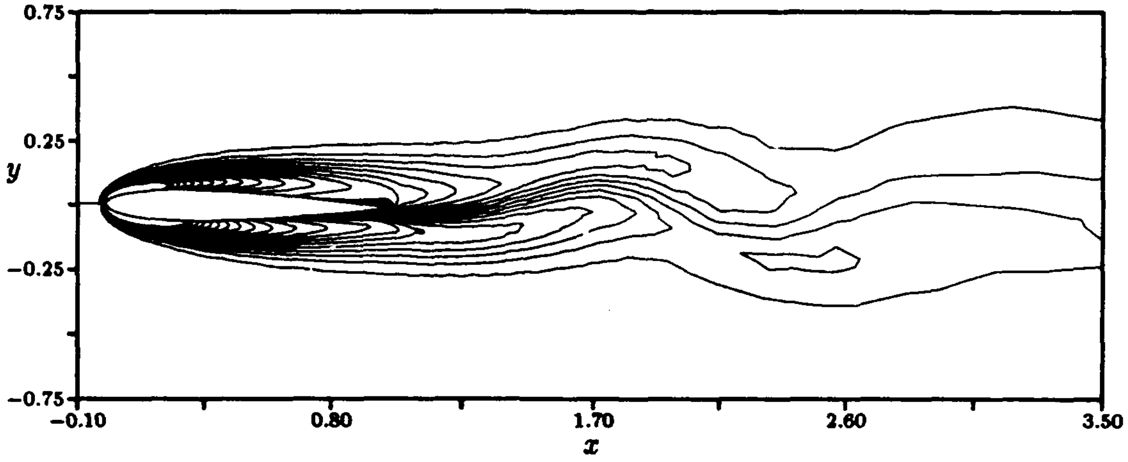

Figure 43. Vorticity Contours: Compressible Code, O-grid 120x50, $Re = 500$, $k = 2$, $\tau = 3.0$

5.4 Conclusions

The influence of the turbulence model is demonstrated in the numerical results for the incompressible code. Implementation of the modified Baldwin-Lomax turbulence model allowed the numerical calculation of flutter-onset speeds corresponding to theoretical and experimental values for a NACA 0015 airfoil. The numerical onset of flutter is a function of ω_h and ω_α independently, in contrast to the theoretical results, which predict onset as a function of the ratio of these parameters. The reason for this effect is the subcritical nature of the bifurcation. There is experimental evidence of this as well, where Yang and Zhao [11] noted a plunge-dominated mode that could only be excited by a physical displacement of the airfoil, indicating a differential response to perturbation level.

The greatest challenge to the accurate calculation of flutter onset for a given structure is the development of turbulence models applicable in this regime. The Baldwin-Lomax model has been criticized in the unsteady and complex flow regimes [14, 47], and in the ability to accurately predict self-induced oscillations [16]. It is unclear at present whether alternatives, such as the $k-\epsilon$ model [47], would be superior. The present research indicates that the Baldwin-Lomax model may serve adequately in predicting flutter onset associated with bifurcations from an equilibrium state. In such a regime, the flow is not dynamic and the application of the turbulence model may be more appropriate. This conclusion is substantiated numerically for the case of forced, small amplitude airfoil oscillations where the inclusion of the turbulence model produces no discernable impact upon the computed lift time history. However, since the scope of this demonstration is limited, further research is warranted in this area.

A basis is established to validate the aerodynamic response for the compressible and incompressible codes and their application to the numerical calculation of flutter. The strong correspondence between the lift coefficient predicted by Theodorsen's function and the numerically calculated lift coefficient across a range of reduced frequencies indicates the applicability of these codes in this capacity. The incompressible code is superior to the compressible code in the low Reynolds number regime, while the compressible code is superior across the range of frequencies and at higher Reynolds numbers. The incompressible code fails to accurately predict the unsteady lift for $k \geq 4$. This failure is attributed to the lack of artificial dissipation in the η direction. The inability to apply simultaneous η- and ξ-upwinding for the non-conservative form of the equations is therefore a detriment. Possible solutions to this problem are rewriting the equations in conservative form, the application of artificial dissipation in conjuction with central-differencing, or both. The compressible code also displays increased error associated with increased frequencies, $k \geq 6$, but they are less pronounced.

VI. Summary

This section is presented to provide a synthesis of the results and conclusions provided in Parts I and II.

In the laminar flow regime explored in Part I, the influence of the structural model of the airfoil on the location of the Hopf bifurcation structure has been demonstrated. In general, the structural model allows the development of sustained, limit-cycle oscillations in the flowfield to develop at a lower Reynolds number than would be the case for a fixed airfoil. This effect is most evident when the structural model incorporates multiple degrees of freedom. Coupling between the axes can occur through either direct structural coupling, or indirectly via the aerodynamics. Single-axis experiments demonstrate that the vertical axis has a minimal impact on the value of Reynolds number at which the flow becomes oscillatory in the absense of a resonance effect, while the pitch axis has a more pronounced effect. The effect of structural damping is most pronounced in the bistable region, beyond this region, the structural damping impacts the airfoil motion more strongly than the aerodymanic flowfield, which will remain unsteady regardless of the structural damping level.

The structure of the bifurcation is subcritical, as the existence of perturbations in the flowfield can initiate sustained oscillations at a Reynolds number lower than would occur when starting from an initial equilibrium state. The influence of the structural model may be more pronounced on the branch of periodic solutions in the bistable region than on the Hopf point itself. In addition, the structural model is seen to provoke additional frequency content in the time history of C_l, for example. The addition of structural elements may induce secondary bifurcations which perturb the solution trajectory from a single, closed orbit in phase space to a more complicated orbit. This is true in the long-term time behavior and in the immediate evolution away from an equilibrium solution.

The influence of the turbulence model is demonstrated in the numerical results for the incompressible code in Part II. Implementation of the modified Baldwin-Lomax turbulence model allowed the numerical calculation of flutter-onset speeds corresponding to theoretical and experimental values for a NACA 0015 airfoil. The numerical onset of flutter is a function of ω_h and ω_α independently, in contrast to the theoretical results, which predict onset as a function of the ratio of these parameters. The reason for this effect is the subcritical nature of the bifurcation. There is experimental evidence of this as well, where Yang and Zhao [11] noted a plunge-dominated mode that could only be excited by a physical displacement of the airfoil, indicating a differential response to perturbation level.

The greatest challenge to the accurate calculation of flutter onset for a given structure is the development of turbulence models applicable in this regime. The Baldwin-Lomax model has been criticized in the unsteady and complex flow regimes [14, 47], and in the ability to accurately predict self-induced oscillations [16]. It is unclear at present whether alternative turbulence models, such as the $k-\epsilon$ model [47], would be superior. The present research indicates that the Baldwin-Lomax model may serve adequately in predicting flutter onset associated with bifurcations from an equilibrium state. In such a regime, the flow is not dynamic and the application of the turbulence model may be more appropriate. This conclusion is substantiated numerically for the case of forced, small amplitude airfoil oscillations where the inclusion of the turbulence model produces no discernable impact upon the computed lift time history. However, since the scope of this demonstration is limited, further research is warranted in this area, particularly in the area of grid refinement, as it was noted on the finer grids that application of turbulence inhibits the bifurcation to secondary oscillations. The fundamental mode of oscillation remains unchanged for both coarse and fine grids.

A basis is established to validate the aerodynamic response for the compressible and incompressible codes and their application to the numerical calculation of flutter. The strong correspondence between the lift coefficient predicted by Theodorsen's function and the numerically calculated lift coefficient across a range of reduced frequencies indicates the applicability of these codes in this capacity. The incompressible code is superior to the compressible code in the low Reynolds number regime, while the compressible code is superior across the range of frequencies and at higher Reynolds numbers. The incompressible code fails to accurately predict the unsteady lift for $k \geq 4$. This failure is attributed to the lack of artificial dissipation in the η direction. The inability to apply simultaneous η- and ξ-upwinding for the non-conservative form of the equations is therefore a detriment. Possible solutions to this problem are rewriting the equations in conservative form, the application of artificial dissipation in conjuction with central-differencing, or both. The compressible code also displays increased error (when compared with the theoretical result) associated with increased frequencies, $k \geq 6$, but they are less pronounced.

Grid sensitivities to critical parameters such as the Strouhal number and critical Reynolds number are considerable. Relatively minor changes in grid spacing or domain size may have a sizeable effect on numerical results. At a minimum, a limited grid refinement study is therefore required to establish consistent results.

Appendix A. *Code Validation*

The validation of the incompressible code was divided into two parts. In the first part, as reported by Lutton and Beran [5], the accuracy of the unsteady numerical results was examined for the case of a circular cylinder. The cylinder was chosen because of the availability of experimental and numerical results. In the second part of the validation, the application of the vertical axis was examined within the context of the aerodynamic portion of the code. The vertical axis was examined singularly because the equation for the pitch axis is of identical form.

A.1 Integration of the Navier-Stokes Equations

The algorithm and the implementation of the algorithm are validated by applying the numerical procedure to the simulation of flow about a fixed circular cylinder. Details specific to the application are discussed first, followed by a comparison of computed results with data reported in previous experimental and numerical investigations.

The grid structure used for the analysis of an airfoil flow was not appropriate for a similar analysis involving a circular cylinder, since a sharp trailing edge is absent from the latter geometry. For the circular cylinder, the numerical procedure was modified to treat an O-grid, like the one pictured in Figure 44a. Aside from trivial changes in the numerical algorithm to account for the altered grid, substantial changes in the application of numerical dissipation and boundary condition enforcement were required. Also, an alternative grid generation technique was employed. In the development of the governing equations for the new flowfield, the radius of the cylinder, a, was chosen as a length scale. With the velocity field scaled by U, a natural Reynolds number was obtained, $\mathrm{Re}_a \equiv Ua/\nu$, which is proportional to a

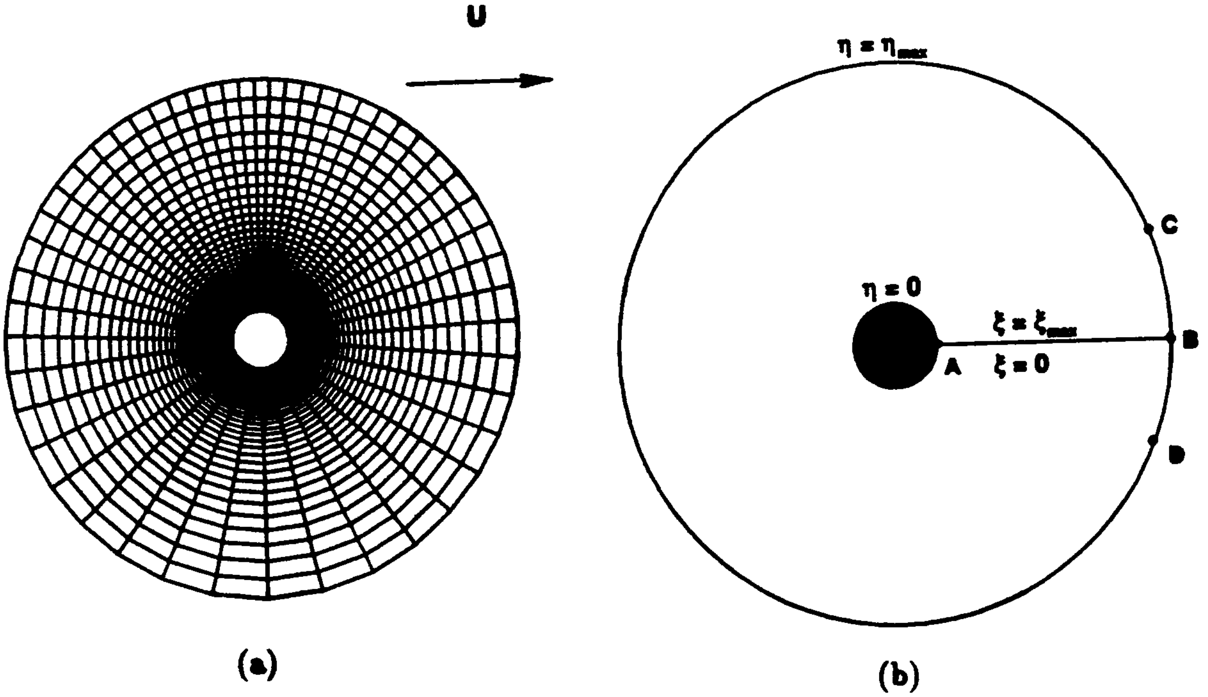

Figure 44. O-grid Structure: (a) Node Distribution; (b) Schematic of Boundaries

Reynolds number based on cylinder diameter, d:

$$\mathrm{Re}_d \equiv \frac{Ud}{\nu} = 2\mathrm{Re}_a.$$

For the O-grid, node points were distributed along rays emanating from the cylinder center. The rays were clustered about the grid cut, AB, aft of the cylinder (see Figure 44b). In an equivalent manner on each ray, the radial node spacing was increased through a geometric progression, starting with a minimum value, Δs_n, at the cylinder surface. The radial position of the outer boundary, R, the number of nodes in the radial direction, J, and Δs_n, serve to define uniquely the node arrangement. The angular distribution of rays was also calculated using a geometric progression, where the smallest angular increment, $2\beta\pi/(I-1)$, was specified to occur adjacent to the cut, while the largest increment was specified to occur adjacent to the forward stagnation point (nodes were placed symmetrically about the centerline). Here, I is the number of nodes in the azimuthal direction and β is a free parameter that was chosen to be 0.5.

Results were obtained using three grids, O1 (coarse grid), O2 (fine grid) and O3 (large and fine grid). Characteristics of these grids are summarized in Table 4.

The O-grid structure differs most from the C-grid structure in the wake region. There, lines of constant η are basically aligned with the freestream direction for the airfoil and normal to the freestream for the circular cylinder. Owing to the importance of numerical dissipation in the computation of smooth wake flows, it was necessary to switch the application of upwinding from ξ derivatives (airfoil) to η derivatives (circular cylinder). The change in the application of upwinding was straightforward to implement, since the convection terms are handled explicitly.

Outflow conditions in the airfoil analysis were naturally enforced along the straight boundary of the C-grid, downstream of the airfoil. For the O-grid, outflow conditions were specified over a predefined arc, CD (see Figure 44b). The number of nodes comprising the arc was $2I\gamma$, where for all calculations $\gamma = 0.15$ was chosen. The vorticity condition enforced on arc CD was $\omega_\eta = 0$, which was evaluated using a 2-point approximation to ω_η. Sa and Chang [50] applied the same outflow condition, but over an arc defined by the local properties of ψ.

After the integration algorithm was modified to incorporate an O-grid structure, flows over a fixed, circular cylinder were numerically simulated for Reynolds numbers between 10 and 80 in increments of 10. Drag coefficient and Strouhal number, $S_t = f_s d/U$, were used to compare computed results to data available in the

Grid	R	I	J	Δs_n
O1	101	51	51	0.01
O2	101	101	101	0.01
O3	201	101	201	0.01

Table 4. Characterstics of Grids O1, O2 and O3

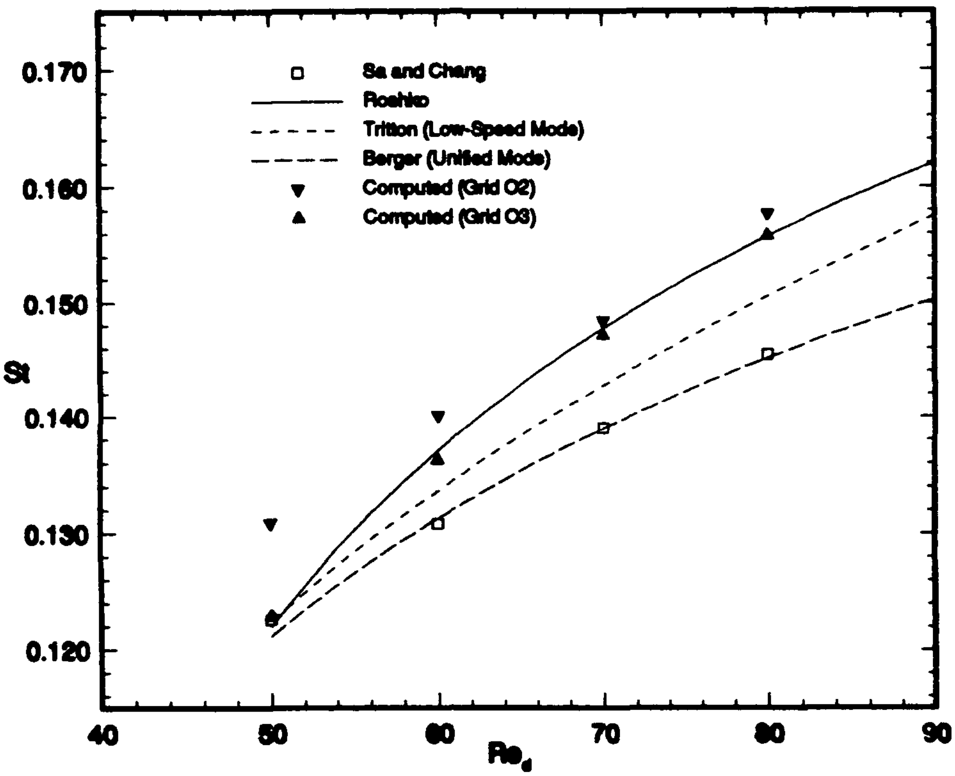

Figure 45. **Strouhal Number as a Function of Reynolds no. Experimental:** Roshko [28], Tritton [29] and Berger [30]; Computational: Sa and Chang [51], and Present (Grids O2 and O3).

literature. Time-periodic solutions were obtained at Reynolds numbers equal to or greater than 50. No attempt was made to compute the critical Reynolds number (between 40 and 50) at which the flow first becomes unsteady. A time step of 0.04 was used for Reynolds numbers greater than 50. At smaller Reynolds numbers, for which the computed flowfields were steady, larger time steps were taken. Time-dependent results were insensitive to reductions of time step below 0.04. Solutions were also found to be insensitive to changes in the geometric parameter Δs_n. Sensitivity to the parameters β and γ was not evaluated.

Computed Strouhal number was compared to the results of experimental and numerical investigations in Figure 45. It should be noted that the solutions obtained with grid O1 for $Re_d \geq 50$ were unsteady, but not time-periodic, and behaved in a spurious manner. It is believed that this departure from periodicity, not observed with grids O2 and O3 for the range of Reynolds number reported, is directly attributable to grid coarseness and the non-conservative formulation of the convective terms. Thus, aperiodic solutions obtained with grid O1 were not included in the results presented below. The experimental studies of Roshko [28], Tritton [29] and Berger [30] and the numerical investigation of Sa and Chang [51] served as a basis for comparison. The computed results were found to be in excellent agreement with Roshko's data, except for grid O2 near $\text{Re}_d = 50$. Apparently, at Reynolds numbers just exceeding the critical Reynolds number, the effects of domain size are significant, and a domain size of $R = 101$ is insufficient. The trend of decreasing S_t with increasing R was also observed by Sa and Chang [50] when the freestream boundary condition on perturbation streamfunction, $\psi = 0$, was enforced. It is unclear to the authors whether the disparity between the present data and that computed by Sa and Chang [51] is a result of differences in the treatment of the convective terms or in differences of grid structure. Sa and Chang employ a conservative formulation of the convective terms, with 4th-order approximations to velocity components, and report results for a 51×50 O-grid.

The drag coefficients associated with computed flowfields about a circular cylinder are plotted in Figure 46 versus Reynolds number. The experimental study of Tritton [29] and the numerical investigations of Borthwick [52] and Sa and Chang [51] were used as a basis for comparison. When $\text{Re}_d \leq 40$ (steady flow), the results of the present study show little sensitivity to grid parameters. Computed values of C_d are 5% to 10% below Tritton's best-fit data. At a Reynolds number of 50 there is a noticeable difference between data obtained with grids O2 and O3. The larger domain, O3, provides a close match to the value predicted by Sa and Chang, perhaps owing to their enforcement of a highly accurate far-field condition on streamfunction. As Reynolds number was increased beyond 50, computed drag values obtained with grids O2 and O3 were quite close, but tended to somewhat exceed that indicated by experiment. Numerical integration at Reynolds numbers beyond about 150 is complicated by the development of turbulence in the cylinder wake (Roshko [28]).

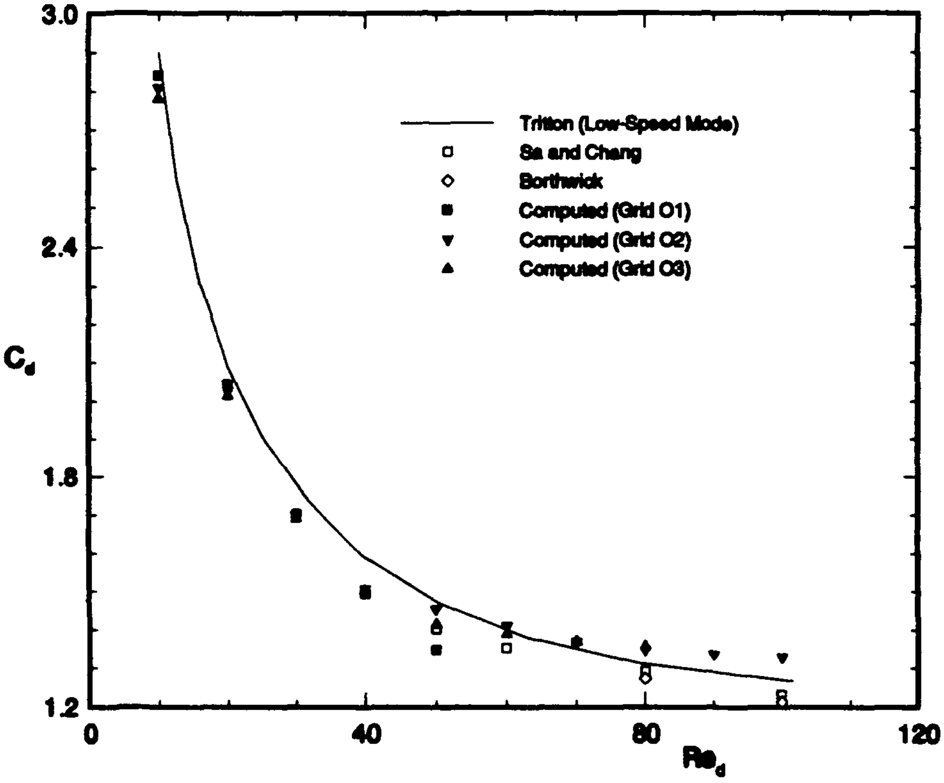

Figure 46. Drag Coefficient as a Function of Reynolds Number. Experimental: Tritton [29]; Computational: Sa and Chang [51], Borthwick [52], and Present (Grids O1, O2 and O3).

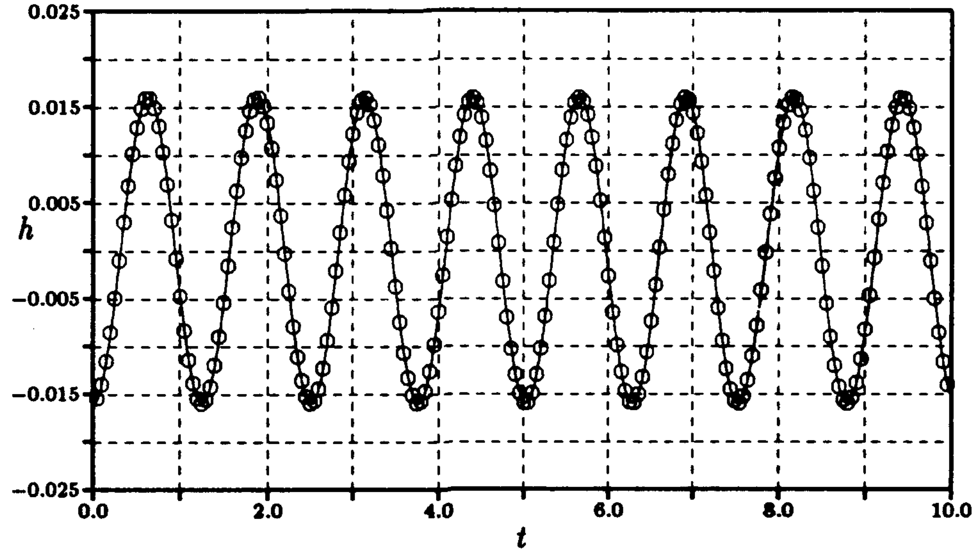

Figure 47. Comparison of Exact (solid line) and Runge-Kutta (⊙) Solutions: Vertical Axis

A.2 Application of Structural Model

As mentioned earlier (cf. Section 2.5), the aerodynamic coefficients are calculated immediately after the calculation of ψ and ω, and are treated as constants over the interval t to $t + \Delta t$. This introduces a phase lag of up to Δt in the application of the loads. However, at the small timesteps required for the stability of the overall scheme, this does not introduce significant error. To substantiate this statement, the vertical axis (cf. Eq. (18)) was examined to validate the Runge-Kutta integration procedure. A prescribed forcing function was applied to the right-hand side of Eq. (18):

$$Q_h = A_o \sin(\omega_f t + \delta). \tag{143}$$

This equation has an exact solution (for $\delta = 0$) given by [53]

$$h(t) = \frac{A_o}{K_h\sqrt{a^2 + b^2}} \sin(\omega_f t + \theta), \tag{144}$$

where $a = 2\zeta r$, $b = 1 - r^2$, $r = \omega_f/\omega_h$, and $\theta = \arctan(a/b)$. Values for the constants were $m_o = 1.0$, $S_\alpha = 0.0$, $D_h = 20.0$, and $K_h = 25.0$, for which $\zeta = 2.0$. The solution was then integrated numerically by applying the Runge-Kutta method using the same forcing function except that in this case δ was set to 0.01. This value of δ represented the largest timestep employed throughout the numerical experiments. Most timesteps were considerably smaller, particularly when finer grids were employed. The results are displayed in Figure 47. No pronounced difference is evident in the two solutions, and it is judged that the application of the lagged forcing function with Runge-Kutta integration has a minimal impact on airfoil motion.

Appendix B. *Comparison of Incompressible Codes*

B.1 Validity of LU Decomposition Approach

The method of solution for the linear system of equations presented in Chapter 2 (Eq. (59))

$$\mathcal{A}\Delta^n\psi_i = N_4 + \hat{G}_i(L_2N_2 - N_1) - \hat{G}_sN_3,$$

where

$$\mathcal{A} \equiv -(\hat{G}_iL_1 + \hat{G}_sL_3),$$

was chosen to be LU decomposition because the matrix $\mathcal{A}$ is time-invariant (for a constant time step and Reynolds number), and can therefore decomposed into the product of lower and upper triangular matrices once at the start of the time-integration procedure.

The operators L_1 and L_2 represent the discrete form of the Laplace operator acting on $\Delta\psi$ to satisfy the Poisson equation. Further, the operator $\hat{G}$ implicitly applies the Laplace operator to $\Delta^n\omega$. However, the Poisson equation (Eq. (28)), shown here again for convenience,

$$\tilde{J}^2\nabla^2\psi = \phi_2\psi_{\xi\xi} + \phi_1\psi_{\eta\eta} - 2\phi_3\psi_{\xi\eta} + \phi_4\psi_\xi + \phi_5\psi_\eta = -\tilde{J}^2\omega,$$

contains the terms ϕ_1 through ϕ_5:

$$\begin{aligned}
\phi_1 &= x_\xi^2 + y_\xi^2, \\
\phi_2 &= x_\eta^2 + y_\eta^2, \\
\phi_3 &= x_\xi x_\eta + y_\xi y_\eta, \\
\phi_4 &= \tilde{J}^{-1}[\phi_1(y_{\eta\eta}x_\eta - x_{\eta\eta}y_\eta) + \phi_2(y_{\xi\xi}x_\eta - x_{\xi\xi}y_\eta) + 2\phi_3(x_{\xi\eta}y_\eta - y_{\xi\eta}x_\eta)], \\
\phi_5 &= -\tilde{J}^{-1}[\phi_1(y_{\eta\eta}x_\xi - x_{\eta\eta}y_\xi) + \phi_2(y_{\xi\xi}x_\xi - x_{\zeta\xi}y_\xi) + 2\phi_3(x_{\xi\eta}y_\xi - y_{\xi\eta}x_\xi)].
\end{aligned}$$

It is then required to demonstrate the validity of the described approach when the time-dependent metric transforation introduced in Chapter 4 (Eq. (69)) is applied. In this case the metrics are functions of time, and the ϕ_i are functions of the metrics and their derivatives. To this end, consider first the Jacobian $\tilde{J}$

$$\tilde{J} \equiv x_\xi y_\eta - x_\eta y_\xi \neq 0,$$

since it is intuitively clear that for the case of a rigid grid, the Jacobian must remain time-invariant under the action of arbitrary grid motions. Imposing a prescribed coordinate transformation from system $(\bar{x}, \bar{y})$ to system (x, y):

$$x = \bar{x}\cos\theta - \bar{y}\sin\theta + h_x,$$
$$y = \bar{x}\sin\theta + \bar{y}\cos\theta + h_y,$$

where θ represents the angle of rotation and h_x, h_y the respective translational displacements. In this case, the metrics are related by

$$x_\xi = \bar{x}_\xi \cos\theta - \bar{y}_\xi \sin\theta, \qquad x_\eta = \bar{x}_\eta \cos\theta - \bar{y}_\eta \sin\theta,$$
$$y_\xi = \bar{x}_\xi \sin\theta + \bar{y}_\xi \cos\theta, \qquad y_\eta = \bar{x}_\eta \sin\theta + \bar{y}_\eta \sin\theta,$$

and further

$$x_{\xi\xi} = \bar{x}_{\xi\xi} \cos\theta - \bar{y}_{\xi\xi} \sin\theta, \qquad x_{\eta\eta} = \bar{x}_{\eta\eta} \cos\theta - \bar{y}_{\eta\eta} \sin\theta,$$
$$y_{\xi\xi} = \bar{x}_{\xi\xi} \sin\theta + \bar{y}_{\xi\xi} \cos\theta, \qquad y_{\eta\eta} = \bar{x}_{\eta\eta} \sin\theta + \bar{y}_{\eta\eta} \sin\theta,$$
$$x_{\xi\eta} = \bar{x}_{\xi\eta} \cos\theta - \bar{y}_{\xi\eta} \sin\theta, \qquad y_{\xi\eta} = \bar{x}_{\xi\eta} \sin\theta + \bar{y}_{\xi\eta} \sin\theta,$$

Substituting these into the definition of $\tilde{J}$

$$\tilde{J} \;=\; (\bar{x}_\xi \cos\theta - \bar{y}_\xi \sin\theta)(\bar{x}_\eta \sin\theta + \bar{y}_\eta \sin\theta$$

$$\begin{aligned}
&- && (\bar{x}_\eta \cos\theta - \bar{y}_\eta \sin\theta)(\bar{x}_\eta \sin\theta + \bar{y}_\eta \sin\theta) \\
&= && \bar{x}_\xi \bar{y}_\eta (\cos^2\theta + \sin^2\theta) - \bar{x}_\eta \bar{y}_\xi (\cos^2\theta + \sin^2\theta) \\
&+ && \bar{x}_\xi \bar{x}_\eta \cos\theta \sin\theta - \bar{y}_\xi \bar{y}_\eta \cos\theta \sin\theta \\
&- && \bar{x}_\xi \bar{x}_\eta \cos\theta \sin\theta + \bar{y}_\xi \bar{y}_\eta \cos\theta \sin\theta \\
&= && \bar{x}_\xi \bar{y}_\eta - \bar{x}_\eta \bar{y}_\xi ,
\end{aligned}$$

and so the Jacobian is time-invariant, as expected. Now the process is repeated for the ϕ_i, starting with ϕ_1:

$$\begin{aligned}
\phi_1 &= (\bar{x}_\xi \cos\theta - \bar{y}_\xi \sin\theta)^2 + (\bar{x}_\xi \sin\theta + \bar{y}_\xi \cos\theta)^2 \\
&= \bar{x}_\xi^2 (\cos^2\theta + \sin^2\theta) + \bar{y}_\xi^2 (\cos^2\theta + \sin^2\theta) \\
&+ 2\bar{x}_\xi \bar{y}_\xi \cos\theta \sin\theta - 2\bar{x}_\xi \bar{y}_\xi \cos\theta \sin\theta \\
&= \bar{x}_\xi^2 + \bar{y}_\xi^2 ,
\end{aligned}$$

and continuing with ϕ_2

$$\begin{aligned}
\phi_2 &= (\bar{x}_\eta \cos\theta - \bar{y}_\eta \sin\theta)^2 + (\bar{x}_\eta \sin\theta + \bar{y}_\eta \cos\theta)^2 \\
&= \bar{x}_\eta^2 (\cos^2\theta + \sin^2\theta) + \bar{y}_\eta^2 (\cos^2\theta + \sin^2\theta) \\
&+ 2\bar{x}_\eta \bar{y}_\eta \cos\theta \sin\theta - 2\bar{x}_\eta \bar{y}_\eta \cos\theta \sin\theta \\
&= \bar{x}_\eta^2 + \bar{y}_\eta^2 ,
\end{aligned}$$

and ϕ_3

$$\begin{aligned}
\phi_3 &= (\bar{x}_\xi \cos\theta - \bar{y}_\xi \sin\theta)(\bar{x}_\eta \cos\theta - \bar{y}_\eta \sin\theta) \\
&+ (\bar{x}_\xi \sin\theta + \bar{y}_\xi \cos\theta)(\bar{x}_\eta \sin\theta + \bar{y}_\eta \cos\theta) \\
&= \bar{x}_\xi \bar{x}_\eta (\cos^2\theta + \sin^2\theta) + \bar{y}_\xi \bar{y}_\eta (\cos^2\theta + \sin^2\theta) \\
&+ \bar{x}_\xi \bar{y}_\eta \cos\theta \sin\theta - \bar{x}_\xi \bar{y}_\eta \cos\theta \sin\theta \\
&+ \bar{x}_\eta \bar{y}_\xi \cos\theta \sin\theta - \bar{x}_\eta \bar{y}_\xi \cos\theta \sin\theta
\end{aligned}$$

$$= \bar{x}_\xi \bar{x}_\eta + \bar{y}_\xi \bar{y}_\eta.$$

With $\tilde{J}, \phi_1, \phi_2$ and ϕ_3 established as time- invariant, all that remains to demonstrate the same for ϕ_4 and ϕ_5 is to examine the terms containing second derivatives in their definition, that is,

$$\begin{aligned}
(y_{\eta\eta}x_\eta - x_{\eta\eta}y_\eta) &= (\bar{x}_{\eta\eta}\sin\theta + \bar{y}_{\eta\eta}\cos\theta)(\bar{x}_\eta\cos\theta - \bar{y}_\eta\sin\theta) \\
&- (\bar{x}_{\eta\eta}\cos\theta - \bar{y}_{\eta\eta}\sin\theta)(\bar{x}_\eta\sin\theta + \bar{y}_\eta\cos\theta) \\
&= \bar{x}_{\eta\eta}\bar{x}_\eta\cos\theta\sin\theta + \bar{y}_{\eta\eta}\bar{x}_\eta\cos^2\theta \\
&- \bar{x}_{\eta\eta}\bar{y}_\eta\sin^2\theta - \bar{y}_{\eta\eta}\bar{y}_\eta\cos\theta\sin\theta \\
&+ \bar{y}_{\eta\eta}\bar{x}_\eta\sin^2\theta - \bar{x}_{\eta\eta}\bar{x}_\eta\cos\theta\sin\theta \\
&- \bar{x}_{\eta\eta}\bar{y}_\eta\cos^2\theta + \bar{y}_{\eta\eta}\bar{y}_\eta\cos\theta\sin\theta \\
&= (\bar{y}_{\eta\eta}\bar{x}_\eta - \bar{x}_{\eta\eta}\bar{y}_\eta),
\end{aligned}$$

and by permutation of subscripts, it is established in similar fashion that

$$\begin{aligned}
(y_{\xi\xi}x_\eta - x_{\xi\xi}y_\eta) &= (\bar{y}_{\xi\xi}\bar{x}_\eta - \bar{x}_{\xi\xi}\bar{y}_\eta), \\
(x_{\xi\eta}y_\eta - y_{\xi\eta}x_\eta) &= (\bar{x}_{\xi\eta}\bar{y}_\eta - \bar{y}_{\xi\eta}\bar{x}_\eta), \\
(y_{\eta\eta}x_\xi - x_{\eta\eta}y_\xi) &= (\bar{y}_{\eta\eta}\bar{x}_\xi - \bar{x}_{\eta\eta}\bar{y}_\xi), \\
(y_{\xi\xi}x_\xi - x_{\xi\xi}y_\xi) &= (\bar{y}_{\xi\xi}\bar{x}_\xi - \bar{x}_{\xi\xi}\bar{y}_\xi), \\
(x_{\xi\eta}y_\xi - y_{\xi\eta}x_\xi) &= (\bar{x}_{\xi\eta}\bar{y}_\xi - \bar{y}_{\xi\eta}\bar{x}_\xi).
\end{aligned}$$

It is therefore established that the application of LU decomposition as described is valid.

B.2 Stability Analysis by Model Equation

To investigate the difference in the stability characteristics of the two versions of the incompressible code, a comparative stability analysis is undertaken. A comparative stability analysis of this type is not available in the literature. The stability analysis is accomplished using a Fourier analysis (also refered to as the von Neumann analysis) [54] applied to the linearized, viscous Burger's equation. Burger's equation is selected because of the similarity to the vorticity-transport equation (cf. Eq. (29)).

To facilitate the examination of the two methods, a similar treatment is applied to Burger's equation. In the first case, a source term is applied which represents the apparent body forces which are similarly applied to the momentum equation (see Chapter 2). In the second case, a time-dependent coordinate transformation is applied to Burger's equation, as in the modified form of the incompressible code (see Chapter 4). The Fourier analysis is applied after discretization utilizing, in both cases, a forward-time (first-order) and central-space (second-order) approach.

Proceeding with the Case 1, Burger's equation with source term

$$S = y\dot{\Omega} + x\Omega^2,$$

with y representing a free parameter, is written as

$$\frac{\partial u}{\partial t} + c\frac{\partial u}{\partial x} = \mu\frac{\partial^2 u}{\partial x^2} + S. \tag{145}$$

The discretized equation is written as

$$\frac{u_j^{n+1} - u_j^n}{\Delta t} + c\frac{u_{j+1}^n - u_{j-1}^n}{2\Delta x} = \mu\frac{u_{j+1}^n - 2u_j^n + u_{j-1}^n}{\Delta x^2} + S,$$

or upon rearranging

$$u_j^{n+1} = u_j^n - \tfrac{1}{2}\tfrac{c\Delta t}{\Delta x}(u_{j+1}^n - u_{j-1}^n) + \tfrac{\mu\Delta t}{\Delta x^2}(u_{j+1}^n - 2u_j^n + u_{j-1}^n) + S(\Delta t).$$

The exact solution and the error must assume the same form [54], hence the error is written as $u_j^n - u_{exact}|_j^n$. Assuming an error distribution of the form $\epsilon_m(x,t) = e^{at}e^{ik_m x}$ where m is a summation index in the Fourier series representing the wavenumber, i.e.,

$$\epsilon(x,t) = \sum_m z_m e^{ik_m x},$$

with $z_m \to e^{at}$, we have

$$\begin{aligned} e^{a(t+\Delta t)}e^{ikx} &= \left(1 - 2\frac{\mu\Delta t}{\Delta x^2}\right) e^{at}e^{ikx} - \tfrac{1}{2}\frac{c\Delta t}{\Delta x}\left(e^{at}e^{ik(x+\Delta x)} - e^{at}e^{ik(x-\Delta x)}\right) \\ &\quad + \frac{\mu\Delta t}{\Delta x^2}\left(e^{at}e^{ik(x+\Delta x)} - e^{at}e^{ik(x-\Delta x)}\right) + S(\Delta t). \end{aligned}$$

Dividing the above equation by $e^{at}e^{ikx}$ and using the identities

$$\begin{aligned} \cos\beta &= \tfrac{1}{2}(e^{i\beta} + e^{-i\beta}), \\ i\sin\beta &= \tfrac{1}{2}(e^{i\beta} - e^{-i\beta}). \end{aligned}$$

where $\beta = k_m x$, the resulting equation can be written as

$$\begin{aligned} e^{a\Delta t} &= \left(1 - 2\frac{\mu\Delta t}{\Delta x^2}\right) - i\frac{c\Delta t}{\Delta x}\sin\beta + 2\frac{\mu\Delta t}{\Delta x^2}\cos\beta + S(\Delta t) \\ &= 1 + 2r_2(\cos\beta - 1) - ir_1\sin\beta + S(\Delta t), \end{aligned}$$

with $r_1 = c\Delta t/\Delta x$ and $r_2 = \mu\Delta t/\Delta x^2$.

The modulus of the amplification factor, $e^{a\Delta t}$, must remain less than unity, resulting in the stability restriction

$$A_1 \equiv |1 + 2r_2(\cos\beta - 1) - ir_1\sin\beta + S(\Delta t)| \leq 1. \tag{146}$$

A similar analysis is undertaken for Case 2. The time-dependent coordinate transformation

$$\xi = \xi(x,t), \qquad \tau = t,$$

is applied to Eq. (145) in lieu of the source term applied in Case 1. The transformed equation is written as

$$\frac{\partial u}{\partial \tau} + (\xi_x c + \xi_t)\frac{\partial u}{\partial \xi} = \mu\left(\xi_x^2 \frac{\partial^2 u}{\partial \xi^2} + \xi_{xx}\frac{\partial u}{\partial \xi}\right),$$

with transformation metrics given by

$$\xi_x = \frac{1}{J}, \qquad \xi_t = -\frac{x_\tau}{J},$$

and the Jacobian defined by

$$J = \frac{1}{x_\xi}.$$

To retain the same form for the viscous terms, choose a transformation such that $\xi_x = 1$ and $\xi_{xx} = 0$, resulting in

$$\frac{\partial u}{\partial \tau} + \tilde{c}\frac{\partial u}{\partial \xi} = \mu\frac{\partial^2 u}{\partial \xi^2}, \tag{147}$$

where $\tilde{c} = c + \xi_t$ is the modified convective coefficient. Note that the redefinition of the convective term does not directly correspond to the inclusion of a source term.

Application of the Fourier analysis for this case results in the amplification factor for Case 2, A_2,

$$A_2 \equiv e^{a\Delta t} = 1 + 2r_2(\cos\beta - 1) - i(r_1 + \frac{\xi_t \Delta t}{\Delta x})\sin\beta. \tag{148}$$

Corresponding to the case of pure rotation, set $x_\tau = \Omega y$, for which $\xi_t = -\Omega y/J$. In comparing the amplification factors for the two cases (Eqs. (146) and (148)), it is noted that both retain a dependence on the parameter Ω, however, the source term in the first case is proportional to Ω^2. In addition, the explicit dependence on $\dot{\Omega}$ vanishes in the second case. It is also noted that the source term S contributes to the real part of A_1, while the additional terms in the second case contribute to the imaginary part of A_2.

The parameters for the two cases were selected to represent a typical application, with $r_1 = 0.5$, $r_2 = 0.375$, $\Delta t = .01$ and $\Omega = \dot{\Omega} = 1.0$. In Case 1 $y = 2.0$ corresponding to the application of the oscillatory boundary conditions on the outer computational boundary, while in the Case 2, $y = 0.2$ corresponding with the application of the oscillatory boundary conditions on the airfoil surface. The real and imaginary components of the amplification factors $A_i = e^{a\Delta t}$ are plotted as the phase angle β is rotated through 2π. The results are shown in Figure 47. The dashed line represents the unit circle, and thus represents a stability boundary. The solid line in Figure 47a indicates the modulus of A_1. The results show that a growth of the amplification factor occurs for Case 1, as the source term contributes to the increase in the real component. In the Case 2, however, shown in Figure 47b the rotational rates contribute to an increase in the imaginary component, where there is a greater stability margin.

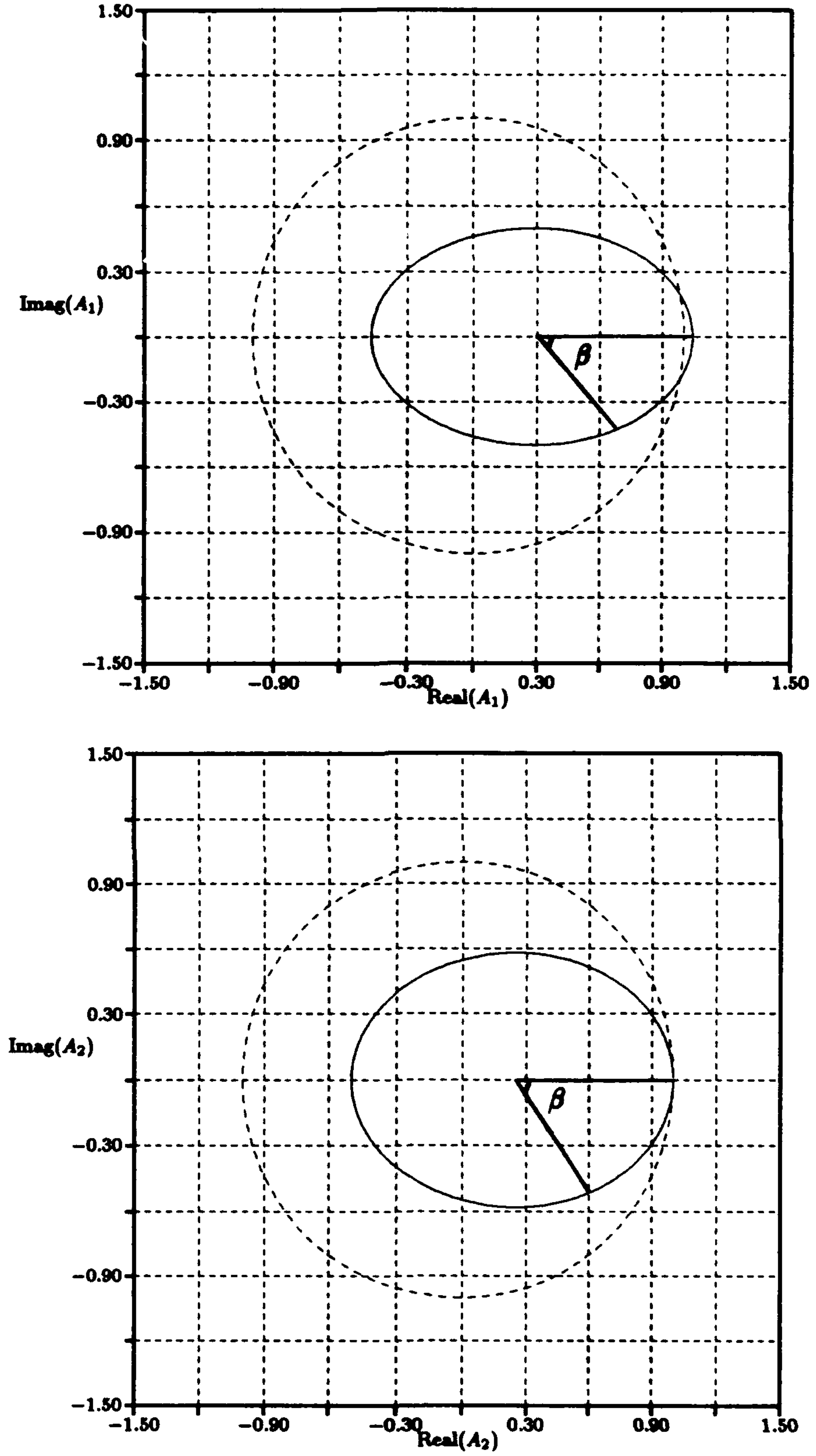

Figure 48. Modulus of Amplification Factor in Complex Plane, (a) Case 1 (A_1), (b) Case 2 (A_2)

Appendix C. *Direct Calculation of Hopf Points*

The conditions for Hopf bifurcation are given by Seydel [6]. Let $F(y,\beta)$ represent a non-linear mapping from $R^n \times R$ into R^n, with $y \in R^n$ and $\beta \in R$. A solution of the system of differential equations

$$y_t + F(y,\beta) = 0$$

is steady-state at a point (y°,β°) if

$$F(y^\circ,\beta^0) = 0.$$

If further the Jacobian matrix

$$A \equiv \left.\frac{\partial F}{\partial y}\right|_{(y^\circ,\beta^\circ)}$$

has a simple pair of purely imaginary eigenvalues $\lambda = \pm i\theta$, and the so-called "transversality condition" is satisfied

$$\left.\frac{d}{d\beta}(Real[\lambda(\beta)])\right|_{\beta_o} \neq 0,$$

then there emerges a branch of limit-cycle solutions. The period of the limit cycle is given by $2\pi/\theta$, and the initial amplitude is zero.

The following sections detail the calculation of Hopf bifurcation points for the fixed airfoil [9] and the modifications made for the case of the moving airfoil.

C.1 Hopf Bifurcation Algorithm: Fixed Airfoil

The following analysis by Beran and Lutton [9] permits the application of the method of Griewank and Reddien [55] to the direct calculation of the Hopf point.

The equations of motion are recast by using an operator notation (per Section 2.5)

$$L_1\psi_i + L_2\psi_s + \omega_i = 0, \tag{149}$$

$$\psi_s + \hat{y} = 0, \tag{150}$$

$$\omega_s + L_3(\psi_i + \hat{y}) = 0, \tag{151}$$

$$\omega_t + G(\psi_i, \psi_s, \omega_i, \omega_s) = 0. \tag{152}$$

The vectors of streamfunction and vorticity are ordered in the following way

$$\psi = \begin{pmatrix} \psi_i \\ \psi_s \end{pmatrix}, \qquad \omega = \begin{pmatrix} \omega_i \\ \omega_s \end{pmatrix},$$

where the i subscript denotes evaluation at internal nodes while the s subscript denotes evaluation at the airfoil surface. This ordering is performed to isolate equations that explicitly contain time derivatives. The linear operators L_1 and L_2 represent discrete forms of the Laplacian operator in the Poisson equation for the streamfunction; L_3 is the discrete form of the operator applied at the airfoil surface for the vorticity.

The temporal development of small perturbations about a known, steady- state solution (ψ^o, ω^o) is assessed by making the collective ansatz

$$\psi_i(t) = \psi_i^o + \epsilon f_i e^{\lambda t}, \qquad \psi_s(t) = \psi_s^o + \epsilon f_s e^{\lambda t}, \tag{153}$$

$$\omega_i(t) = \omega_i^o + \epsilon g_i e^{\lambda t}, \qquad \omega_s(t) = \omega_s^o + \epsilon g_s e^{\lambda t}. \tag{154}$$

Substitution into Eq. (150) establishes that $f_s = 0$ and further substitution into Eqs. (149) and (151) provides

$$L_1 f_i + g_i \;=\; 0, \tag{155}$$

$$L_3 f_i + g_s = 0. \tag{156}$$

The dynamic vorticity equation yields an equation, through linearization, for the growth coefficient λ

$$G^o_{\psi_i} f_i + (G^o_{\omega_i} + \lambda) g_i + G^o_{\omega_s} g_s = 0, \tag{157}$$

where the superscript "o" denotes evaluation at (ψ^o, ω^o). By expressing g_i and g_s in terms of f_i, a single equation for f_i can be derived

$$G^o_{\psi_i} f_i + (G^o_{\omega_i} + \lambda)(-L_1 f_i) + G^o_{\omega_s}(-L_3 f_i) = 0. \tag{158}$$

This equation may be recast as

$$L_1^{-1} \mathcal{A} f_i = \lambda f_i, \tag{159}$$

where

$$\mathcal{A} \equiv (G^o_{\psi_i} - G^o_{\omega_i} L_1 - G^o_{\omega_s} L_3). \tag{160}$$

The method of Griewank and Reddien may now be applied to the complete system of equations, including the Hopf point criteria. The bifurcation parameter, β, is the inverse of Reynolds number and now represents an unknown variable. The complete system is then

$$F_1 = L_1 \psi_i + L_2 \psi_s + \omega_i = 0, \tag{161}$$

$$F_2 = \psi_s + \hat{y} = 0, \tag{162}$$

$$F_3 = L_3(\psi_i + \hat{y}) + \omega_s = 0, \tag{163}$$

$$F_4 = G(\psi_i, \psi_s, \omega_i, \omega_s; \beta) = 0, \tag{164}$$

$$F_5 = \mathcal{A}(\psi_i, \psi_s, \omega_i, \omega_s; \beta) p_1 + \theta L_1 p_2 = 0, \tag{165}$$

$$F_6 = \mathcal{A}(\psi_i, \psi_s, \omega_i, \omega_s; \beta) p_2 - \theta L_1 p_1 = 0, \tag{166}$$

$$F_7 = q^T p_1 = 0, \tag{167}$$

$$F_8 = q^T p_2 - 1 = 0, \tag{168}$$

where $p = p_1 + ip_2$ is an eigenvector and $\lambda = i\theta$ an eigenvalue satisfying the Hopf condition for Eq. (159). Eqs. (164) and (166) result after substituting $i\theta$ into Eq. (159) and equating the real and imaginary parts. Eqs. (167) and (168) represent two real normalizing conditions for the vector p, where q is an arbitrary vector with the same dimension as p. Solution of the complete system is accomplished through the application of Newton's method and Gaussian elimination. The implementation of Newton's method requires a linearization of Eqs. (161-168) in order to apply the iterative scheme

$$A^\nu \Delta^\nu x \equiv A^\nu (x^{\nu+1} - x^\nu) = -F(x^\nu) = -F^\nu, \tag{169}$$

where A^ν is the Jacobian matrix, evaluated at the ν-th Newton iterate:

$$A^\nu \equiv F_x^\nu \equiv \left. \frac{\partial F}{\partial x} \right|_{x^\nu} . \tag{170}$$

The iteration procedure is continued until F^ν, or alternately $\Delta^\nu x$, becomes sufficiently small. Solutions have been obtained for the case of the stationary airfoil and have been verified by time integration and examination of the eigenvalue spectrum of $L_1^{-1}\mathcal{A}$ near the Hopf point by Beran and Lutton [9].

C.2 Hopf Bifurcation Algorithm: Moving Airfoil

The following approach allows a similar calculation for the case of a rotating, translating airfoil. To accommodate the motion of the airfoil, an extended ansatz set is required. A consistent ansatz set would begin, in the case of the pitch axis, with a perturbation about the angle of attack, $\alpha = \alpha^o + \epsilon f_\alpha e^{\lambda t}$. However, there are several disadvantages in such an approach. Firstly, the surface quantity f_s is no longer zero, and the complexity and memory requirements of the algorithm are significantly increased. In addition, the resulting equation set is no longer cast in the form of a standard eigenvalue problem, as in Eq. (159), invalidating the assumed approach. A brief development is presented to indicate the difficulties. The following ansatz set is chosen

$$h = h^o + \epsilon f_h e^{\lambda t}, \qquad \dot{h} = \dot{h}^o + \epsilon \lambda f_h e^{\lambda t}, \qquad \ddot{h} = \ddot{h}^o + \epsilon \lambda^2 f_h e^{\lambda t}, \tag{171}$$

$$\alpha = \alpha^o + \epsilon f_\alpha e^{\lambda t}, \qquad \dot{\alpha} = \dot{\alpha}^o + \epsilon \lambda f_\alpha e^{\lambda t}, \qquad \ddot{\alpha} = \ddot{\alpha}^o + \epsilon \lambda^2 f_\alpha e^{\lambda t}. \tag{172}$$

Application of Eqs. (171)-(172) to Eqs. (149)-(152) provides for the relationships

$$L_1 f_i + L_2 f_s + g_i = 0, \tag{173}$$

$$f_s + \hat{y}_\alpha f_\alpha = 0, \tag{174}$$

$$L_3(f_i + \hat{y} f_\alpha) + g_s = 0, \tag{175}$$

$$G^o_{\psi_s} f_s + G^o_{\psi_i} f_i + G^o_{\omega_s} g_s + (\lambda + G^o_{\omega_i}) g_i + G^o_{\dot{\alpha}} \lambda f_\alpha + G^o_{\ddot{\alpha}} \lambda^2 f_\alpha + G^o_{\ddot{h}} \lambda^2 f_h = 0. \tag{176}$$

A further relationship is established between f_i, f_h, and f_α by considering the airfoil equations of motion, with no damping or structural coupling (cf. Eqs. (18)-(19)). Denoting Q_h as R and Q_α as Q, the equation representing the vertical axis may be written as

$$m\ddot{h} + k_h h = R.$$

Linearization provides

$$(m\lambda^2 + k_h) f_h = (R^o_{\psi_i} - R^o_{\omega_s} L_3 - R^o_{\omega_i} L_1) f_i$$

$$-(R^o_{\psi_s}\hat{y}_\alpha + R^o_{\omega_s}L_3\hat{y}_\alpha + R^o_{\omega.}L_1\hat{y}_\alpha)f_\alpha, \tag{177}$$

Similarly, for the pitch axis

$$I\ddot{\alpha} + k_\alpha\alpha = Q,$$

$$(I\lambda^2 + k_\alpha + Q^o_{\psi_s}\hat{y}_\alpha + Q^o_{\omega_s}L_3\hat{y}_\alpha + Q^o_{\omega_i}L_2\hat{y}_\alpha)f_\alpha = (Q^o_{\psi_i} - Q^o_{\omega_s}L_3 - Q^o_{\omega_i}L_1)f_i. \tag{178}$$

Returning to the vorticity-transport equation and substituting provides

$$\begin{aligned}
&- \lambda[L_1 + L_2\hat{y}_\alpha(I\lambda^2 + k_\alpha + Q^o_{\psi_s}\hat{y}_\alpha + Q^o_{\omega_s}L_3\hat{y}_\alpha + Q^o_{\omega_i}L_2\hat{y}_\alpha)^{-1}(Q^o_{\psi_i} - Q^o_{\omega_s}L_3 - Q^o_{\omega_i}L_1)]f_i\\
&- G^o_{\psi_s}(I\lambda^2 + k_\alpha + Q^o_{\psi_s}\hat{y}_\alpha + Q^o_{\omega_s}L_3\hat{y}_\alpha + Q^o_{\omega_i}L_2\hat{y}_\alpha)^{-1}(Q^o_{\psi_i} - Q^o_{\omega_s}L_3 - Q^o_{\omega_i}L_1)f_i\\
&- G^o_{\omega_s}L_3\hat{y}_\alpha(I\lambda^2 + k_\alpha + Q^o_{\psi_s}\hat{y}_\alpha + Q^o_{\omega_s}L_3\hat{y}_\alpha + Q^o_{\omega_i}L_2\hat{y}_\alpha)^{-1}(Q^o_{\psi_i} - Q^o_{\omega_s}L_3 - Q^o_{\omega_i}L_1)f_i\\
&- G^o_{\omega_i}L_2\hat{y}_\alpha(I\lambda^2 + k_\alpha + Q^o_{\psi_s}\hat{y}_\alpha + Q^o_{\omega_s}L_3\hat{y}_\alpha + Q^o_{\omega_i}L_2\hat{y}_\alpha)^{-1}(Q^o_{\psi_i} - Q^o_{\omega_s}L_3 - Q^o_{\omega_i}L_1)f_i\\
&+ G^o_{\dot{\alpha}}\lambda(I\lambda^2 + k_\alpha + Q^o_{\psi_s}\hat{y}_\alpha + Q^o_{\omega_s}L_3\hat{y}_\alpha + Q^o_{\omega_i}L_2\hat{y}_\alpha)^{-1}(Q^o_{\psi_i} - Q^o_{\omega_s}L_3 - Q^o_{\omega_i}L_1)f_i\\
&+ G^o_{\ddot{\alpha}}\lambda^2(I\lambda^2 + k_\alpha + Q^o_{\psi_s}\hat{y}_\alpha + Q^o_{\omega_s}L_3\hat{y}_\alpha + Q^o_{\omega_i}L_2\hat{y}_\alpha)^{-1}(Q^o_{\psi_i} - Q^o_{\omega_s}L_3 - Q^o_{\omega_i}L_1)f_i\\
&+ G^o_{\ddot{h}}\lambda^2(m\lambda^2 + k_h)^{-1}[(R^o_{\psi_i} - R^o_{\omega_s}L_3 - R^o_{\omega_i}L_1) - (R^o_{\psi_s}\hat{y}_\alpha + R^o_{\omega_s}L_3\hat{y}_\alpha + R^o_{\omega_i}L_1\hat{y}_\alpha)\\
&\quad (I\lambda^2 + k_\alpha + Q^o_{\psi_s}\hat{y}_\alpha + Q^o_{\omega_s}L_3\hat{y}_\alpha + Q^o_{\omega_i}L_2\hat{y}_\alpha)^{-1}(Q^o_{\psi_i} - Q^o_{\omega_s}L_3 - Q^o_{\omega_i}L_1)]f_i\\
&+ (G^o_{\psi_i} - G^o_{\omega_s}L_3 - G^o_{\omega_I}L_1)f_i = 0.
\end{aligned} \tag{179}$$

This equation corresponds to Eq. (159), arrived at in the case of the fixed airfoil. However, the form presented does not allow a tractable application of the algorithm.

To rectify these problems, a hybrid ansatz set is applied:

$$\begin{aligned}
\dot{h} &= \dot{h}^o + \epsilon f_h e^{\lambda t}, \qquad \ddot{h} = \ddot{h}^o + \epsilon\lambda f_h e^{\lambda t},\\
\dot{\alpha} &= \dot{\alpha}^o + \epsilon f_h e^{\lambda t}, \qquad \ddot{\alpha} = \ddot{\alpha}^o + \epsilon\lambda f_h e^{\lambda t}.
\end{aligned} \tag{180}$$

The justification for this approach arises from the examination of the additional terms appended to the momentum equation (cf. Eqs. (9) and (10)). The additive terms f_1 and f_2 do not contain α or h, but rather refer only to the linear and angular velocities and accelerations, hence only these terms are perturbed. The failure to incorporate a perturbation about α and h otherwise has the effect of lagging the boundary conditions.

Proceeding with this approach, the substantial change from the original equation set, Eqs. (149-152), occurs in the vorticity-transport equation, where

$$\omega_t + G(\psi_i, \psi_s, \omega_i, \omega_s, \dot{\alpha}, \ddot{\alpha}, \ddot{h}) = 0. \tag{181}$$

Expanding G about the equilibrium state produces

$$\begin{aligned} G(\psi_s^o + \epsilon f_s e^{\lambda t}, \cdots) = G(\psi_s^o, \cdots) \; & + \; \left.\frac{\partial G}{\partial \psi_s}\right|_o \epsilon f_s e^{\lambda t} + \left.\frac{\partial G}{\partial \psi_i}\right|_o \epsilon f_i e^{\lambda t} + \left.\frac{\partial G}{\partial \omega_s}\right|_o \epsilon g_s e^{\lambda t} \\ & + \; \left.\frac{\partial G}{\partial \omega_i}\right|_o \epsilon g_i e^{\lambda t} + \left.\frac{\partial G}{\partial \dot{\alpha}}\right|_o \epsilon f_\alpha e^{\lambda t} + \left.\frac{\partial G}{\partial \ddot{\alpha}}\right|_o \epsilon \lambda f_\alpha e^{\lambda t} \\ & + \; \left.\frac{\partial G}{\partial \ddot{h}}\right|_o \epsilon \lambda f_h e^{\lambda t} + \mathcal{O}(\epsilon^2). \end{aligned} \tag{182}$$

Upon subtraction of the equilibrium solution from the expanded vorticity-transport equqtion and division by $\epsilon e^{\lambda t}$, an equation corresponding to Eq. (158) is obtained:

$$G^o_{\psi_s} f_s + G^o_{\psi_i} f_i + (G^o_{\omega_i} + \lambda) g_i + G^o_{\omega_s} g_s + (G^o_{\dot{\alpha}} + \lambda G^o_{\ddot{\alpha}}) f_\alpha + \lambda G^o_{\ddot{h}} f_\alpha = 0. \tag{183}$$

As before, $f_s = 0$, and the relationship between f_i, g_s, and g_i is provided by Eqs. (155) and (156). Then a relationship between f_i, f_h, and f_α is developed is accomplished by again considering the airfoil equations of motion, Eqs. (18) and (19), with damping and structural coupling omitted. The approach is to first consider the unsteady equation to establish the relationship for $\ddot{\alpha}$, and then consider perturbations about the equilibrium equation to establish the relationship for $\dot{\alpha}$.

$$(\lambda m_o + k_h) f_h - (R^o_{\psi_i} - R^o_{\omega_i} L_1 - R^o_{\omega_s} L_3) f_i = 0, \tag{184}$$

$$(\lambda I_\alpha + k_\alpha) f_\alpha - (Q^o_{\psi_i} - Q^o_{\omega_i} L_1 - Q^o_{\omega_s} L_3) f_i = 0. \tag{185}$$

Upon substituting Eqs. (184)-(185) into Eq. (183), the identical form is obtained for the eigenvalue problem (cf. Eq. (159)), provided that the matrix $\mathcal{A}$ is redefined as

$$\begin{aligned} \mathcal{A} \equiv & \left(G^o_{\psi_i} - G^o_{\omega_i} L_1 - G^o_{\omega_s} L_3\right) \\ + & \left(\frac{1}{I_\alpha} G^o_{\ddot{\alpha}} + \frac{1}{k_\alpha} G^o_{\dot{\alpha}}\right)\left(Q^o_{\psi_i} - Q^o_{\omega_i} L_1 - Q^o_{\omega_s} L_3\right) \\ + & \left(\frac{1}{m_o} G^o_{\ddot{h}} + \frac{1}{k_h} G^o_{\dot{h}}\right)\left(R^o_{\psi_i} - R^o_{\omega_i} L_1 - R^o_{\omega_s} L_3\right). \end{aligned} \tag{186}$$

The derivatives of G with respect to $\dot{h}$, $\ddot{h}$, $\dot{\alpha}$, and $\ddot{\alpha}$ can be evaluated explicitly. The vorticity-transport equation is (cf. Eq. (29))

$$G = \hat{u}\omega_\xi + \hat{v}\omega_\eta - \frac{1}{Re}\nabla^2\omega - (\hat{f}_1 - \hat{f}_2) = 0, \tag{187}$$

where

$$\begin{aligned} f_1 &= -\ddot{h}\sin\alpha + 2v\dot{\alpha} + y\ddot{\alpha} - x\dot{\alpha}^2, \\ f_2 &= \ddot{h}\cos\alpha - 2u\dot{\alpha} - x\ddot{\alpha} - y\dot{\alpha}^2, \end{aligned}$$

$$\begin{aligned} \hat{f}_1 &= \xi_y f_{1\xi} + \eta_y f_{1\eta}, \\ \hat{f}_2 &= \xi_x f_{2\xi} + \eta_x f_{2\eta}. \end{aligned}$$

The additional contribution to the vorticity transport equation is expressed as

$$(\hat{f}_1 - \hat{f}_2) = \tilde{J}^{-1}(x_\xi f_{1\eta} - x_\eta f_{1\xi} + y_\xi f_{2\eta} - y_\eta f_{2\xi}). \tag{188}$$

The required derivatives $G^o_{\dot{\alpha}}$, $G^o_{\ddot{\alpha}}$, $G^o_{\dot{h}}$, and $G^o_{\ddot{}}$ are then

$$G^o_{\dot{\alpha}} = \left.\frac{\partial G}{\partial \dot{\alpha}}\right|_o$$

$$\begin{aligned}
&= -\frac{\partial}{\partial\dot{\alpha}}(\hat{f}_1 - \hat{f}_2) \\
&= -\tilde{J}^{-1}\frac{\partial}{\partial\dot{\alpha}}(x_\xi f_{1\eta} - x_\eta f_{1\xi} + y_\xi f_{2\eta} - y_\eta f_{2\xi}) \\
&= -2\tilde{J}^{-1}(x_\xi v_\eta - x_\eta v_\xi + y_\eta u_\xi - y_\xi u_\eta), \qquad (189)
\end{aligned}$$

similarly

$$\begin{aligned}
G^o_{\ddot{\alpha}} &= \left.\frac{\partial G}{\partial\ddot{\alpha}}\right|_o \\
&= -\frac{\partial}{\partial\ddot{\alpha}}(\hat{f}_1 - \hat{f}_2) \\
&= -\tilde{J}^{-1}\frac{\partial}{\partial\ddot{\alpha}}(x_\xi f_{1\eta} - x_\eta f_{1\xi} + y_\xi f_{2\eta} - y_\eta f_{2\xi}) \\
&= -\tilde{J}^{-1}(x_\xi y_\eta - x_\eta y_\xi + y_\eta x_\xi - y_\xi x_\eta) \\
&= -\tilde{J}^{-1}(2\tilde{J}) \\
&= -2, \qquad (190)
\end{aligned}$$

and, for the vertical axis,

$$\begin{aligned}
G^o_{\ddot{h}} &= \left.\frac{\partial G}{\partial\ddot{h}}\right|_o \\
&= -\frac{\partial}{\partial\ddot{h}}(\hat{f}_1 - \hat{f}_2) \\
&= -\tilde{J}^{-1}\frac{\partial}{\partial\ddot{h}}(x_\xi f_{1\eta} - x_\eta f_{1\xi} + y_\xi f_{2\eta} - y_\eta f_{2\xi}) \\
&= -\tilde{J}^{-1}(x_\xi(-\sin\alpha)_\eta - x_\eta(-\sin\alpha)_\xi + y_\xi(\cos\alpha)_\eta - y_\eta(\cos\alpha)_\xi) \\
&= 0. \qquad (191)
\end{aligned}$$

Since $\dot{h}$ does not appear in $\hat{f}_1$ or $\hat{f}_2$,

$$G^o_{\dot{h}} = 0. \qquad (192)$$

The application of the modified algorithm, as described, produced an insignificant change in the predicted location of the Hopf point. The critical Reynolds number, Re_{crit}, obtained using the original algorithm (without the extended ansatz set) for Grid 1 was 550. The modified algorithm produced a nearly identical result, $Re_{crit} = 552$. The only pronounced effect that the modifications produced was a much smaller radius of convergence. The initial values of I_α and k_α had to be made very large ($\mathcal{O}(10^7)$), i.e., approximating a fixed airfoil. After obtaining a converged solution, the values of each parameter were reduced by approximately one order of magnitude, and a new solution obtained. This procedure was applied until a solution with $I_\alpha = k_\alpha = 100$ was obtained. Throughout this process, the change in the Hopf point remained insignificant. This was a rather disappointing result, the basis of which lies in the nature of the algorithm. When applying Newton's method, it is required to evaluate the resulting system of equations at equilibrium. At equilibrium, there is no difference between the fixed airfoil and one which can potentially move, hence no difference is observed in the location of the Hopf point. Additionally, it is hypothesized that the structural components principally effect the stable, limit cycle solutions in the bistable region, therefore, a method which essentially searches the path of equilibrium solutions (as per Figure 13) for an instability cannot capture these solutions.

It should be added, as a criticism, that the modified approach can justly be critiqued as lacking rigor, particularly in the assumptions associated with the extended ansatz set. However, additional evidence of a relatively straightforward nature can be offered to support the arguments presented. Consider the time-dependent coordinate transformation presented in Part II (Eq. (69)). The modifications to the boundary equations and vorticity-transport equation are presented there, in Eqs. (71)-(86). Note, however, that the grid speeds x_τ and y_τ and the metric terms ξ_τ and η_τ are all zero at equilibrium. An examination of the aforementioned equations reveals that when applied to the equilibrium system (Eqs. (155-162)), all unsteady terms vanish and the equations assume a form *identical* to those of the fixed airfoil, and as in the previous case, the only potential differences arise in the application of the ansatz and the redefinition of the $\mathcal{A}$ matrix.

Appendix D. *Computer Codes and Resources*

The following hardware resources were utilized, in order of decreasing usage, to perform the computational portions of this dissertation

- AFIT Kubota (Titan 3000) Cluster
- AFIT Convex C 220
- AFIT Stardent ST-2000
- Cray XMP (Wright-Patterson)
- Cray2 (Kirtland)

D.1 Software Documentation

This document was prepared using LaTeX on an AFIT Sun SPARCstation 2. A short synopsis of the computer codes employed is provided, along with a description of the subroutines contained therein. Four main codes were employed:

1. U22 - incompressible code (Part I)
2. U23 - incompressible code (Part II)
3. U26 - incompressible code (Part II)
4. BWO - compressible code (Part II)

The incompressible code U22 allows motion of the airfoil with two degrees of freedom, pitch and vertical motion, and was used for Part I of the dissertation. U23 is identical to U22 except for the implementation of the Baldwin-Lomax turbulence model and the application of η-upwinding. U26 allows airfoil motion in the pitch axis only, applying the time-dependent coordinate transformation described in Section 4.2. This version was used for the correlation with Theodorsen's function and contains the Baldwin-Lomax turbulence model, with η-upwinding eliminated. BWO is the Beam and Warming code authored by Visbal [27], described in Section 4.4.

A short description of input/output files for the above codes and a short synopsis of the subroutines employed is provided below.

U22/23/26

- **Input Files**

  udriver - input file to specify Re, Δt, etc.

  foilgrd - grid file

  foilout - restart file for ψ and ω

  foiledv - restart file for eddy viscosity (U23/26 only)

- **Output Files**

  foilout - restart file for ψ and ω

  foiledv - restart file for eddy viscosity (U23/26 only)

  foilvor - vorticity

  foilstr - streamfunction

  avt - angle of attack vs. time

  clvt - lift coefficient vs. time

  clk - lift coefficient (theoretical) vs. time (U26 only)

  hvt - vertical displacement vs. time

- **Subroutines**

  AEOM - driver file for solving airfoil equations of motion

  BANSOL - linear system solver for banded matrices

  DECOMP - decomposes A matrix into lower and upper triangular matrices

DERIVS - computes functional derivatives for Runge-Kutta integration

ENERGY/ERG2 - computes aerodynamic coefficients

G14CLC - calculation of G operator

LUSOLV - solves LU decomposed system

L12CLC - calculates L_1 and L_2 operators

L3CLC - calculates L_3 operator

METRIC - calculates transformation metrics

N1CLC - calculates N_1 vector

N2CLC - calculates N_2 vector

N3CLC - calculates N_3 vector

N4CLC - calculates N_4 vector

PACKER - calculates column index for banded matrices

RKD/RK4 - implements Runge-Kutta integration

TURBU - implements Baldwin-Lomax turbulence model

VISCO - calculates coefficients of Laplace operator, ϕ_i

BWO

- **Input Files**

  odata - input file to specify Re, Δt, etc.

  ogrid - grid file; also contains field data when performing restart

- **Output Files**

  outo - output file for lift, drag, norms, etc.

  solno - output file for field variables, also used for restarts when renamed as 'ogrid'

avt - angle of attack vs. time

clvt - lift coefficient vs. time

clk - lift coefficient (theoretical) vs. time

hvt - vertical displacement vs. time

- **Subroutines**

BNDRY - implements boundary conditions

BTRIDX/Y - block tridiagonal solvers for x and y sweeps

CMATA - computes Jacobian matrix A

CMATB - computes Jacobian matrix B

CMATM - computes Jacobian matrix M

CMATN - computes Jacobian matrix N

CMXU - computes dynamic viscosity using Sutherland's formula

DAMPEX - implements fourth-order explicit damping in ξ direction

DAMPEY - implements fourth-order explicit damping in η direction

INITIA - initialization routine, computes common parameters

LIFT/1 - computes aerodynamic coefficients

METRIC - calculates transformation metrics and Jacobian

OUTPUT - writes flow field data to output file

RHSV - computes RHS vector

SPECR - computes scaling factor for spectral damping coefficient

STEPX - performs ξ sweep

STEPY - performs η sweep

TMSTEP - computes timestep (when applying local timesteping)

TURB - implements Baldwin-Lomax turbulence model

The computer codes, and the associated drivers, restart files, and grids, are archived on the AFIT Convex 220 in the following directories

`U22 - /home/tmp/mlutton/59x25`
`U23 - /home/tmp/mlutton/59x25/TURB`
`U26 - /home/tmp/mlutton/UMOD`
`BWO - /home/tmp/mlutton/BWO`

D.2 Algorithm Performance

A comparison of computer code performance is shown in Table x. The computations were performed on the Kubota cluster. The codes were executed using vector optimization only. The incompressible code U26 is seen to be more efficient for course grids. The increase in the bandwidth of the linear system results in a degredation of efficiency for the incompressible codes as the grid size increases, and thus the compressible code is more efficient for finer grids. A more efficient implementation of the incompressible code has been developed by Beran [56].

Code	Grid	No. nodes	Timesteps	CPUsec	CPUsec/node/iter
U26	59x25	1475	4000	872.6	1.4783×10^{-4}
BWO	65x25	1625	4000	1355.2	2.0849×10^{-4}
U26	99x40	3960	2000	1731.5	1.9069×10^{-4}
BWO	125x50	6250	2000	2610.3	2.0882×10^{-4}
U26	139x50	6950	2000	3804.2	2.4525×10^{-4}
BWO	209x108	22572	2000	8608.1	1.9068×10^{-4}
U26	179x60	10740	2000	6024.8	2.6582×10^{-4}

Table 5. Comparison of Computer Code Performance

Bibliography

1. Pulliam, T. H. "Low Reynolds number numerical solutions of chaotic flows," *AIAA 27th Aerospace Sciences Meeting*, AIAA-89-0123, January 1989.
2. Pulliam, T. H. "Introduction of chaos theory in CFD," *AIAA 21st Fluid Dynamics, Plasma Dynamics and Lasers Conference.* AIAA-90- 1440, June 1990.
3. Jackson, C. P. "A finite-element study of the onset of vortex shedding in flow past variously shaped bodies," *J. Fluid Mech.*, Volume 182:23-45, 1987.
4. Strganac, T. W., Mook, D. T. "The application of the unsteady vortex lattice method to the nonlinear two degree-of-freedom aeroelastic equations," *AIAA 27th Structures, Structural Dynamics, and Materials Conference.* AIAA-86-0867, May 1987.
5. Lutton, M. and Beran, P. "Hopf bifurcation in viscous, low-speed flows about an airfoil with structural coupling," *Computers and Fluids*, to be published.
6. Seydel, R. *From Equilibrium to Chaos: Practical Bifurcation and Stability Analysis*, Elsevier Science Publishing Co., New York, 1988.
7. Jackson, E. A. *Perspectives of Nonlinear Dynamics, 2 Volumes*, Cambridge University Press, New York, 1989.
8. Beran, P. "Steady and unsteady solutions of the Navier- Stokes equations for flows about airfoils at low speeds," *AIAA 22nd Fluid Dynamics, Plasma Dynamics and Lasers Conference.* AIAA-91-1733, June 1991.
9. Beran, P. and Lutton, M. "Hopf bifurcation in viscous flows about airfoils at low speeds,"*AIAA 22nd Fluid Dynamics, Plasma Dynamics and Lasers Conference.* AIAA-91-1807, June 1991.
10. Lienhard, J. H., "Synopsis of lift, drag, and vortex frequency for rigid circular cylinders," Washington State University, Research Division Bulletin 300, 1966.
11. Yang, Z. C. and L. C. Zhao. "Analysis of limit cycle flutter of an airfoil in incompressible flow," *J. Sound and Vib.*, Volume 123:1-13, 1988.
12. Kehoe, M. "Aircraft flight flutter testing at the NASA Ames-Dryden Flight Test Facility," AIAA-88-2075, 1988.
13. Baldwin, B. S. and Lomax, H. "Thin layer approximation and algebraic model for separated turbulent flows," *AIAA 16th Aerospace Sciences Meeting*, AIAA-78-25, January 1978.
14. Knight, D. and Visbal, M. "The Baldwin-Lomax turbulence model for two-dimensional shock-wave/boundary-layer interactions," *AIAA Journal* Volume 22, No. 7, July 1984.

15. Theodorsen, T. "General theory of aerodynamic instabilities and the mechanism of flutter," NACA Report No. 496, 1935.

16. Guruswamy, G. P. "Vortical flow computations on a flexible blended wing-body configuration," *AIAA Journal* Volume 30, No. 10, October 1992.

17. Kousen, K. and Bendiksen, O. "Nonlinear aspects of the transonic aeroelastic stability problem," *AIAA 29th Structures, Structural Dynamics and Materials Conference.* AIAA-88-2306, April 1988.

18. Wu, J., Srivastava, R., and Sankar, L. "Application of Navier-Stokes analysis to stall flutter," in *Structural Dynamics: Volume 1*, NASA Lewis Research Center, N88-23249, 1988.

19. Bendiksen, O. and Kousen, K. "Transonic flutter analysis using the Euler equations," *AIAA Dynamics Specialists Conference.* AIAA-87-0911, April 1987.

20. Robinson, B., Batina, J. and Yang, H. "Aeroelastic analysis of wings using the Euler equations with a deforming mesh," AIAA-90-1032, 1990.

21. Strganac, T. W., Mook, D. T., and Mitchum, M. "The numerical simulation of subsonic flutter,"*AIAA 19th Fluid Dynamics, Plasma Dynamics, and Lasers Conference.* AIAA-87-1428, June 1987.

22. Laschka, B. et al. "Unsteady Aerodynamics," AGARD Report No. 645, Gottingen, 1975.

23. Blevins, R. D. *Flow-Induced Vibration, 2nd ed.*, Van Nostrand Reinhold, New York, 1990.

24. Kussner, H. G. "A comparison of methods used in flutter research," AGARD Report No. 592, 1972.

25. Dowell, E. H. et al. *A Modern Course in Aeroelasticity*, Sijthoff and Noordhoff, The Netherlands, 1978.

26. Dowell, E. H. "Nonlinear elasticity," AIAA-90-1031, 1990.

27. Visbal, Miguel R. "Vectorized Navier-Stokes code, Beam and Warming algorithm: O-grid configuration," July 1986.

28. Roshko, A. "On the development of turbulent wakes from vortex streets," NACA Report 1191, 1954.

29. Tritton, D. J. "Experiments on the flow past a circular cylinder at low Reynolds number," *J. Fluid Mech.*, Volume 6:547-567, 1959.

30. Berger, E., "Unterdruekung der laminaren wirbelstroemung und des turbulenzeinsatzes der Karmanschen wirbelstrasse im nachlauf eines schwingenden zylinders kleinen Reynolds-zahlen. *Jahrb. 1964 der WGRL* 164-192, 1964.

31. Batchelor, G. *An Introduction to Fluid Dynamics*, Cambridge University Press, New York, 1967.

32. Greenwood, T. *Principles of Dynamics, 2nd ed.*, Prentice-Hall, New Jersey, 1988.
33. Burden, R., Faires, J. and Reynolds, A., *Numerical Analysis, 2nd ed.*, Prindle, Weber, and Schmidt, Massachusetts, 1981.
34. Steger, J. L. "Implicit finite-difference simulation of flow about arbitrary two-dimensional geometries," *AIAA Journal*, Volume 16, No.7, July 1978.
35. Mehta, U. B. "Dynamic stall of an oscillating airfoil," AGARD CP-227, No. 23, 1977.
36. Kinsey, D. W. and T. J. Barth. *Description of a Hyperbolic Grid Generating Procedure for Arbitrary Two-Dimensional Bodies*, Technical Manual, AFWAL, Flight Dynamics Laboratory, WPAFB, OH, AFWAL-TM-84-FIMM, July 1984.
37. Wolfram, S., *Mathematica, 2nd ed.*, Addison-Wesley, California, 1991.
38. Bushnell, D. M. "Turbulence modeling in aerodynamic shear flows - status and problems," *AIAA 29th Aerospace Sciences Meeting*, AIAA-91-0214, January 1991.
39. Visbal, Miguel R. "Calculation of viscous transonic flows about a supercritical airfoil," Air Force Flight Dynamics Laboratory, WPAFB, OH, AFWAL-TR-86-3013, 1986.
40. Schlichting, H. *Boundary-Layer Theory, 7th ed.*, McGraw-Hill, New York, 1978.
41. Hegna, H. A. "Numerical prediction of dynamic forces on arbitrarily pitched airfoils in turbulent flow," AIAA-82-0092, January 1982.
42. Galloway, C. R. "Numerical aerodynamic analysis of a free falling autorotating plate," Dissertation AFIT/DS/AA/83-2, 1983.
43. Ashley, H. and Landahl, M., *Aerodynamics of Wings and Bodies*, Dover, New York, 1965.
44. Beam, R. M. and Warming, R. F. " An implicit factored scheme for the compressible Navier-Stokes equations," *AIAA 3rd Computational Fluid Dynamics Conference*, 1987.
45. Visbal, Miguel R. Air Force Flight Dynamics Laboratory (Wright Laboratory) WPAFB, OH. Private communication, 1989.
46. Chaing, H. D. and Fletter, S. "Prediction of incidence effects on oscillating airfoil aerodynamics by a locally analytical method," *International Journal for Numerical Methods in Engineering*, Volume 26, October 1988.
47. Rizzetta, D. P. and Visbal, M. R. "Comparative numerical study of two turbulence models for airfoil static and dynamic stall," AIAA-92-4649, 1992.
48. Visbal, M. R. "Evaluation of an implicit Navier-Stokes solver for some unsteady separated flows," AIAA-86-1053, May 1986.

49. Stanek, M. J. and Visbal, M. R. "Study of the vortical wake patterns of an oscillating airfoil," AIAA-89-0554, January 1989.

50. Sa, J. and Chang, K. "On far-field stream function condition for two-dimensional incompressible flows," *J. Comp. Physics*, Volume 91:398-412, 1990.

51. Sa, J. and Chang, K. "Shedding Patterns of the near-wake vortices behind a circular cylinder," *Int. J. Num. Meth. Fluids*, Volume 12:463-474, 1991.

52. Borthwick, A. "Comparison between two finite-difference schemes for computing the flow around a cylinder," *Int. J. Numer. Meth. Fluids*, Volume 6:275-290, 1986.

53. Vierck, R. K., *Vibration Analysis, 2nd ed.*, Harper and Row, New York, 1979.

54. Anderson, D., Tannehill, J., and Pletcher, R. *Computational Fluid Mechanics and Heat Transfer*, Hemisphere Publishing, New York, 1984.

55. Griewank, A. and Reddien, G., "The calculation of Hopf points by a direct method," *IMA J. Num. Anal.* Volume 3:295-303, 1983,

56. Beran, P. "An efficient, semi-implicit algorithm for the calculation of incompressible flows about airfoils," in *Advances in Computer Methods for Partial Differential Equations - IV*, IMACS, New Jersey, 1992.

Vita

Captain Mark J. Lutton was born 4 Nov 1956 in Bethlehem, Pennsylvania. He graduated from Liberty High School in 1974 and entered the Air Force in 1977. After serving as a Medical Laboratory Specialist stationed at Eglin Air Force Base in Florida, he was selected for the Airman's Education and Commissioning Program. He attended The Pennsylvania State University and graduated with high distinction, earning a Bachelor of Science in Aerospace Engineering. After completing Officer Training School in 1984, he served as a flight test engineer at the Air Force Flight Test Center, Edwards Air Force Base, California, until entering the School of Engineering, Air Force Institute of Technology in 1988, where as a distinguished graduate, he was awarded the degree of Master of Science in Aeronautical Engineering in December, 1989.

Permanent address: 116 E. North Street
Bethlehem, Pennsylvania
18018

REPORT DOCUMENTATION PAGE

Form Approved
OMB No 0704-0188

Public reporting burden for this collection of information is estimated to average 1 hour per response, including the time for reviewing instructions, searching existing data sources, gathering and maintaining the data needed, and completing and reviewing the collection of information. Send comments regarding this burden estimate or any other aspect of this collection of information, including suggestions for reducing this burden to Washington Headquarters Services, Directorate for Information Operations and Reports, 1215 Jefferson Davis Highway, Suite 1204, Arlington, VA 22202-4302, and to the Office of Management and Budget, Paperwork Reduction Project (0704-0188), Washington, DC 20503

1. AGENCY USE ONLY *(Leave blank)*

2. REPORT DATE
23 Mar 93

3. REPORT TYPE AND DATES COVERED
Dissertation 2 Jan 90 - 23 Mar 93

4. TITLE AND SUBTITLE
Hopf Bifurcation in Viscous, Low Speed Flows About an Airfoil with Structural Coupling

5. FUNDING NUMBERS

6. AUTHOR(S)
Mark John Lutton, MS, Capt, USAF

7. PERFORMING ORGANIZATION NAME(S) AND ADDRESS(ES)
School of Engineering
Air Force Institute of Technology
Wright-Patterson AFB OH 45433

8. PERFORMING ORGANIZATION REPORT NUMBER
AFIT/DS/AA/93 -1

9. SPONSORING/MONITORING AGENCY NAME(S) AND ADDRESS(ES)
Flight Dynamics Directorate
Wright Laboratory (WL/FIMC)
Air Force Materiel Command
Wright-Patterson AFB OH 45433-7913

10. SPONSORING/MONITORING AGENCY REPORT NUMBER

11. SUPPLEMENTARY NOTES

12a. DISTRIBUTION/AVAILABILITY STATEMENT
Approved for public release; unlimited distribution

12b. DISTRIBUTION CODE

13. ABSTRACT *(Maximum 200 words)*

The locations of Hopf bifurcation points associated with the viscous, incompressible flow about a NACA 0012 airfoil with structural coupling are computed for very low Reynolds numbers (<2000). A semi-implicit, first-order-accurate time-integration algorithm is employed to solve the streamfunction-vorticity form of the Navier-Stokes equations. The formulation models the inclusion of simple structural elements affixed to the airfoil and captures the resulting airfoil motion. The equations describing the airfoil motion are integrated in time using a fourth-order Runge-Kutta algorithm. The dissertation is divided into two parts. In part one, numerical experiments are performed in the laminar regime to determine if the structural model of the ailfoil has an effect upon the location of the Hopf bifurcation point when compared with the fixed airfoil. Results are reported for a variety of structural characteristics, including variations of torsional and linear spring constants, inertial properties, structural coupling, and structural damping. The structure of the solution space is explored by means of phase plots. In part two, the Baldwin-Lomax turbulence model is implemented to model turbulent flow. A numerical effort is made to predict the onset of unsteady flow.

14. SUBJECT TERMS
Computational Fluid Dynamics, Hopg Bifurcation, Incompressible Flow, Navier-Stokes Equations, Flutter Onset, Theodorsen's Function

15. NUMBER OF PAGES
150

16. PRICE CODE

17. SECURITY CLASSIFICATION OF REPORT

18. SECURITY CLASSIFICATION OF THIS PAGE

19. SECURITY CLASSIFICATION OF ABSTRACT

20. LIMITATION OF ABSTRACT

NSN 7540-01-280-5500

Standard Form 298 (Rev 2-89)
Prescribed by ANSI Std Z39-18